

14

Radio-Frequency Linear Accelerators

Resonant linear accelerators are usually single-pass machines. Charged particles traverse each section only once; therefore, the kinetic energy of the beam is limited by the length of the accelerator. Strong accelerating electric fields are desirable to achieve the maximum kinetic energy in the shortest length. Although linear accelerators cannot achieve beam, output energy as high as circular accelerators, the following advantages dictate their use in a variety of applications: (1) the open geometry makes it easier to inject and extract beams; (2) high-flux beams can be transported because of the increased options for beam handling and high-power rf structures; and (3) the duty cycle is high. The duty cycle is defined as the fraction of time that the machine produces beam output.

The operation of resonant linear accelerators is based on electromagnetic oscillations in tuned structures. The structures support a traveling wave component with phase velocity close to the velocity of accelerated particles. The technology for generating the waves and the interactions between waves and particles were described in Chapters 12 and 13. Although the term radio

Radio-frequency Linear Accelerators

frequency (rf) is usually applied to resonant accelerators, it is somewhat misleading. Although some resonant linear accelerators have been constructed with very large or inductive structures, most present accelerators use resonant cavities or waveguides with dimensions less than 1 m to contain electromagnetic oscillations; they operate in the microwave regime (> 300 MHz).

Linear accelerators are used to generate singly-charged light ion beams in the range of 10 to 300 MeV or multiply charged heavy ions up to 4 GeV (17 MeV/nucleon). These accelerators have direct applications such as radiation therapy, nuclear research, production of short-lived isotopes, meson production, materials testing, nuclear fuel breeding, and defense technology. Ion linear accelerators are often used as injectors to form high-energy input beams for large circular accelerators. The recent development of the radio-frequency quadrupole (RFQ), which is effective for low-energy ions, suggests new applications in the 1-10 MeV range, such as high-energy ion implantation in materials. Linear accelerators for electrons are important tools for high-energy physics research because they circumvent the problems of synchrotron radiation that limit beam energy in circular accelerators. Electron linear accelerators are also used as injectors for circular accelerators and storage rings. Applications for high-energy electrons include the generation of synchrotron radiation for materials research and photon beam generation through the free electron laser process.

Linear accelerators for electrons differ greatly in both physical properties and technological realization from ion accelerators. The contrasts arise partly from dissimilar application requirements and partly from the physical properties of the particles. Ions are invariably non-relativistic; therefore, their velocity changes significantly during acceleration. Resonant linear accelerators for ions are complex machines, often consisting of three or four different types of acceleration units. In contrast, high-gradient electron accelerators for particle physics research have a uniform structure throughout their length. These devices are described in Section 14.1. Electrons are relativistic immediately after injection and have constant velocity through the accelerator. Linear electron accelerators utilize electron capture by strong electric fields of a wave traveling at the velocity of light. Because of the large power dissipation, the machines are operated in a pulsed mode with low-duty cycle. After a description of the general properties of the accelerators, Section 14.1 discusses electron injection, beam breakup instabilities, the design of iris-loaded wave-guides with $\omega/k = c$, optimization of power distribution for maximum kinetic energy, and the concept of shunt impedance.

Sections 14.2-14.4 review properties of high-energy linear ion accelerators. The four common configurations of rf ion accelerators are discussed in Sections 14.2 and 14.3: the Wideröe accelerator, the independently-phased cavity array, the drift tube linac, and the coupled cavity array. Starting from the basic Wideröe geometry, the rationale for surrounding acceleration gaps with resonant structures is discussed. The configuration of the drift tube linac is derived qualitatively by considering an evolutionary sequence from the Wideröe device. The principles of coupled cavity oscillations are discussed in Section 14.3. Although a coupled cavity array is more difficult to fabricate than a drift tube linac section, the configuration has a number of benefits for high-flux ion beams when operated in a particular mode (the $\pi/2$ mode). Coupled cavities have high accelerating gradient, good frequency stability, and strong energy coupling. The latter property is essential for stable electromagnetic oscillations in the presence of significant beam

loading. Examples of high-energy ion accelerators are included to illustrate strategies for combining the different types of acceleration units into a high-energy system.

Some factors affecting ion transport in rf linacs are discussed in Section 14.4. Included are the transit-time factor, gap coefficients, and radial defocusing by rf fields. The transit-time factor is important when the time for a particle to cross an acceleration gap is comparable to half the rf period. In this case, the peak energy gain (reflecting the integral of charge times electric field during the transit) is less than the product of charge and peak gap voltage. The transit-time derating factor must be included to determine the synchronous particle orbit. The gap coefficient refers to radial variations of longitudinal electric field. The degree of variation depends on the gap geometry and rf frequency. The spatial dependence of E_z leads to increased energy spread in the output beam or reduced longitudinal acceptance. Section 14.4 concludes with a discussion of the effects of the radial fields of a slow traveling wave on beam containment. The existence and nature of radial fields are derived by a transformation to the rest frame of the wave in it appears as electrostatic field pattern. The result is that orbits in cylindrically symmetric rf linacs are radially unstable if the particles are in a phase region of longitudinal stability. Ion linacs must therefore incorporate additional focusing elements (such as an FD quadrupole array) to ensure containment of the beam.

Problems of vacuum breakdown in high-gradient rf accelerators are discussed in Section 14.5. The main difference from the discussion of Section 9.5 is the possibility for geometric growth of the number of secondary electrons emitted from metal surfaces when the electron motion is in synchronism with the oscillating electric fields. This process is called multipactoring. Electron multipactoring is sometimes a significant problem in starting up rf cavities; ultimate limits on accelerating gradient in rf accelerators may be set by ion multipactoring.

Section 14.6 describes the RFQ, a recently-developed configuration. The RFQ differs almost completely from other rf linac structures. The fields are azimuthally asymmetric and the main mode of excitation of the resonant structure is a TE mode rather than a TM mode. The RFQ has significant advantages for the acceleration of high-flux ion beams in the difficult low-energy regime (0.1-5 MeV). The structure utilizes purely electrostatic focusing from rf fields to achieve simultaneous average transverse and longitudinal containment. The electrode geometries in the device can be fabricated to generate precise field variations over small-scale lengths. This gives the RFQ the capability to perform beam bunching within the accelerator, eliminating the need for a separate buncher and beam transport system. At first glance, the RFQ appears to be difficult to describe theoretically. In reality, the problem is tractable if we divide it into parts and apply material from previous chapters. The properties of longitudinally uniform RFQs, such as the interdependence of accelerating gradient and transverse acceptance and the design of shaped electrodes, can be derived with little mathematics.

Section 14.7 reviews the racetrack microtron, an accelerator with the ability to produce continuous high-energy electron beams. The racetrack microtron is a hybrid between linear and circular accelerators; it is best classified as a recirculating resonant linear accelerator. The machine consists of a short linac (with a traveling wave component with $\omega/k = c$) and two regions of uniform magnetic field. The magnetic fields direct electrons back to the entrance of the accelerator in synchronism with the rf oscillations. Energy groups of electrons follow separate

orbits which require individual focusing and orbit correction elements. Synchrotron radiation limits the beam kinetic energy of microtrons to less than 1 GeV. Beam breakup instabilities are a major problem in microtrons; therefore, the output beam current is low ($< 100 \mu\text{A}$). Nonetheless, the high-duty cycle of microtrons means that the time-averaged electron flux is much greater than that from conventional electron linacs.

14.1 ELECTRON LINEAR ACCELERATORS

Radio-frequency linear accelerators are used to generate high-energy electron beams in the range of 2 to 20 GeV. Circular electron accelerators cannot reach high output kinetic energy because of the limits imposed by synchrotron radiation. Linear accelerators for electrons are quite different from ion accelerators. They are high-gradient, traveling wave structures used primarily for particle physics research. Accelerating gradient is the main figure of merit; consequently, the efficiency and duty cycle of electron linacs are low. Other accelerator configurations are used when a high time-averaged flux of electrons at moderate energy is required. One alternative, the racetrack microtron, is described in Section 14.7.

A. General Properties

Figure 14.1 shows a block diagram of an electron linac. The accelerator typically consists of a sequence of identical, iris-loaded slow-wave structures that support traveling waves. The waveguides are driven by high-power klystron microwave amplifiers. The axial electric fields of the waves are high, typically on the order of 8 MV/m. Parameters of the 20-GeV accelerator at the Stanford Linear Accelerator Center are listed in Table 14.1. The accelerator is over 3 km in length; the open aperture for beam transport is only 2 cm in diameter. The successful transport of the beam through such a long, narrow tube is a consequence of the relativistic contraction of the apparent length of the accelerator (Section 13.6). A cross section of the accelerator is illustrated in Figure 14.2. A scale drawing of the rf power distribution system is shown in Figure 14.3.

The features of high-energy electron linear accelerators are determined by the following considerations.

1. Two factors motivate the use of strong accelerating electric fields: (a) high gradient is favorable for electron capture (Section 13.6) and (b) the accelerator length for a given final beam energy is minimized.
2. Resistive losses per unit length are large in a high-gradient accelerator because power dissipation in the waveguide walls scales as E_z^2 . Dissipation is typically greater than 1 MW/m. Electron linacs must be operated on an intermittent duty cycle with a beam pulselength of a few microseconds.

Radio-frequency Linear Accelerators

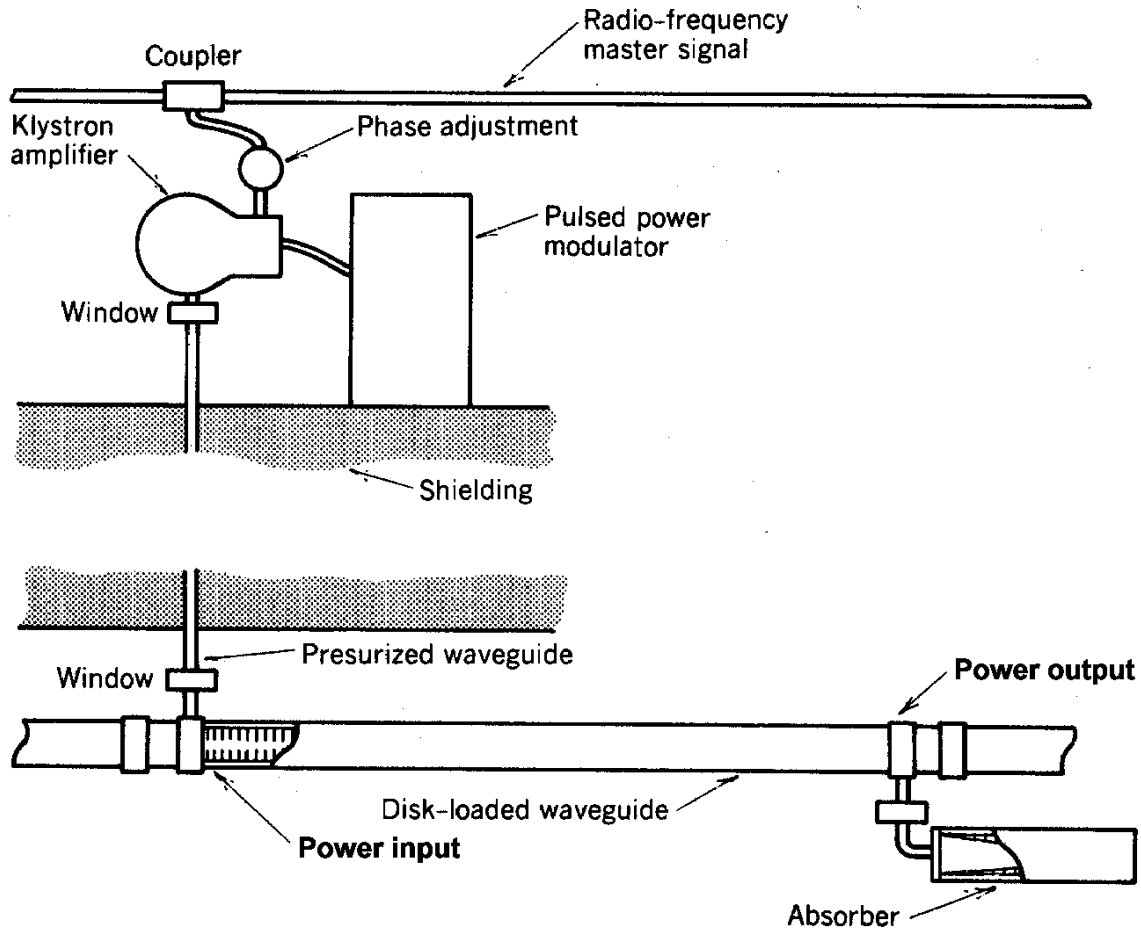


Figure 14.1 High-energy linear electron accelerator.

3. An iris-loaded waveguide with relatively large aperture can support slow waves with $\omega/k = c$. Conduction of rf energy along the waveguide is effective; nonetheless, the waves are attenuated because of the high losses. There is little to be gained by reflecting the traveling waves to produce a standing wave pattern. In practice, the energy of the attenuated wave is extracted from the waveguide at the end of an accelerating section and deposited in an external load. This reduces heating of the waveguides.

4. A pulsed electron beam is injected after the waveguides are filled with rf energy. The beam pulse length is limited by the accelerator duty cycle and by the growth of beam breakup instabilities. Relatively high currents (≤ 0.1 A) are injected to maximize the number of electrons available for experiments.

TABLE 14.1 Parameters of the Stanford Linear Accelerator

Accelerator length	3100 m
Length between power feeds	3.1 m
Number of accelerator sections	960
Number of klystrons	245
Peak power per klystron	6–24 MW
Beam pulse repetition rate	1–360 pulses/s
Radio-frequency pulse length	2.5 μ s
Filling time	0.83 μ s
Shunt impedance	53 M Ω /m
Electron energy (unloaded)	11.1–22.2 GeV
Electron energy (loaded)	10–20 GeV
Electron beam peak current	25–50 mA
Electron beam average current	15–30 μ A
Average electron beam power	0.15–0.6 MW
Efficiency	4.3%
Positron energy	7.4–14.8 GeV
Positron average beam current	0.45 μ A
Operating frequency	2.856 GHz
Accelerating structure	Iris-loaded waveguide
Waveguide outer diameter	10.5 cm
Aperture diameter	1.9 cm

5. The feasibility of electron linacs is a consequence of technological advances in high-power rf amplifiers. Klystrons can generate short pulses of rf power in the 30-MW range with good frequency stability. High-power klystrons are driven by pulsed power modulators such as the PFN discussed in Section 9.12.

The waveguides of the 2.5-GeV accelerator at the National Laboratory for High Energy Physics (KEK), Tsukuba, Japan, have a diameter of 0.1 m and an operating frequency of 2.856 GHz. The choice of frequency results from the availability of high-power klystrons from the development of the SLAC accelerator. An acceleration unit consists of a high-power coupler, a series of four iris-loaded waveguides, a decoupler, and a load. The individual waveguides are 2 m long. The inner radius of the irises has a linear taper of 75 μ m per cell along the length of the guide; this maintains an approximately constant E_z along the structure, even though the traveling wave is

Radio-frequency Linear Accelerators

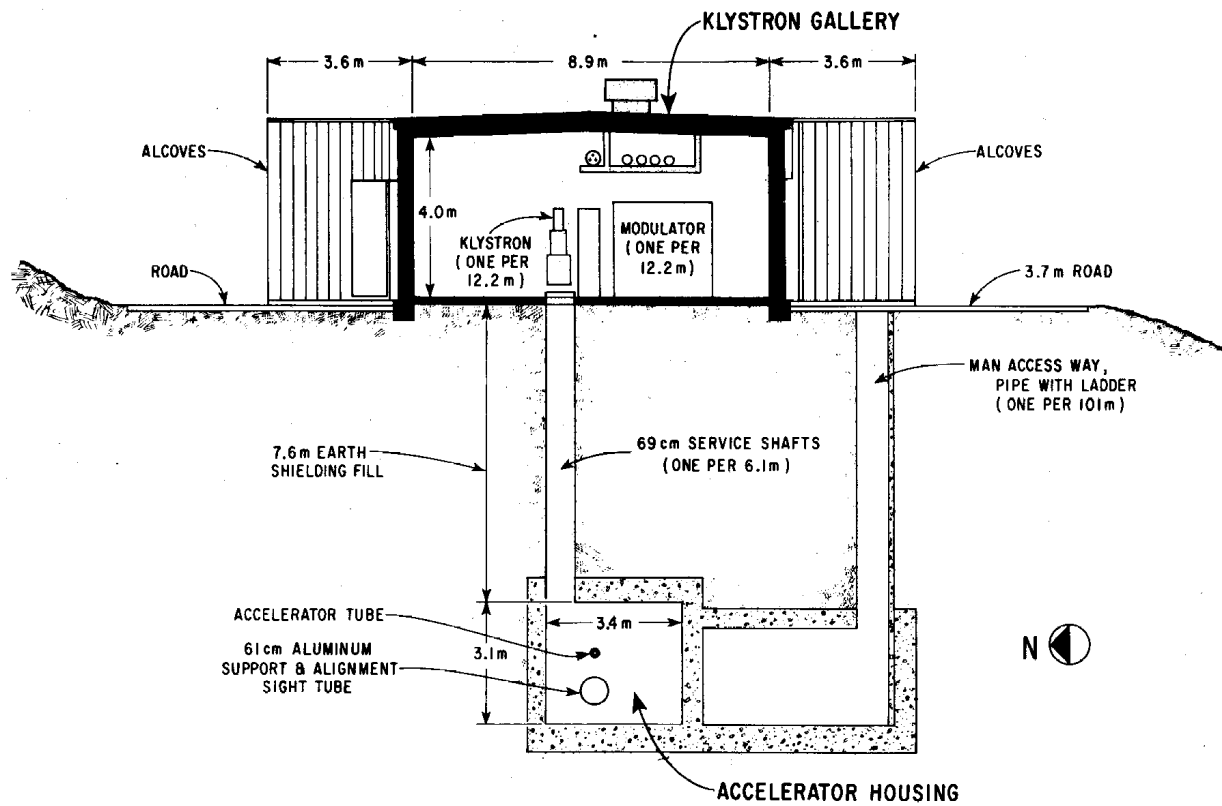


Figure 14.2 Stanford Linear Accelerator; cross section. (Courtesy W. B. Herrmannsfeldt, Stanford Linear Accelerator Center.)

Radio-frequency Linear Accelerators

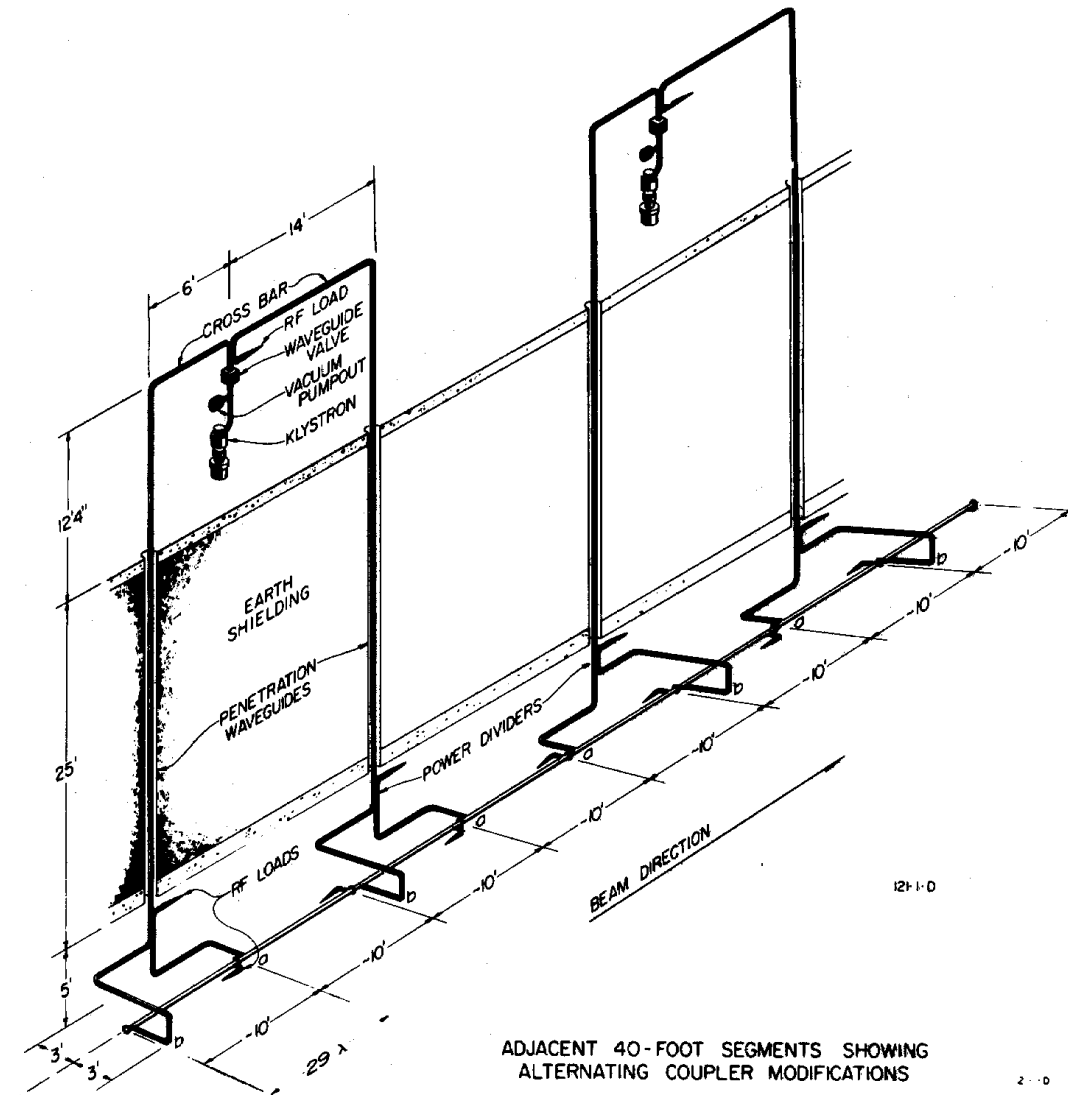


Figure 14.3 Stanford Linear Accelerator; arrangement of rf power system. (Courtesy W. B. Herrmannsfeldt, Stanford Linear Accelerator Center.)

attenuated. Individual waveguides of a unit have the same phase velocity but vary in the relative dimensions of the wall and iris to compensate for their differing distance from the rf power input. There are five types of guides in the accelerator; the unit structure is varied to minimize propagation of beam-excited modes which could contribute to the beam breakup instability. Construction of the guides utilized modern methods of electroplating and precision machining. A dimensional accuracy of $\pm 2 \mu\text{m}$ and a surface roughness of 200 \AA was achieved, making postfabrication tuning unnecessary.

B. Injection

The pulsed electron injector of a high-power electron linear accelerator is designed for high voltage (> 200 kV) to help in electron capture. The beam pulselength may vary from a few nanoseconds to $1\text{ }\mu\text{s}$ depending on the research application. The high-current beam must be aimed with a precision of a few milliradians to prevent beam excitation of undesired rf modes in the accelerator. Before entering the accelerator, the beam is compressed into micropulses by a buncher. A buncher consists of an rf cavity or a short section of iris-loaded waveguide operating at the same frequency as the main accelerator. Electrons emerge from the buncher cavity with a longitudinal velocity dispersion. Fast particles overtake slow particles, resulting in downstream localization of the beam current to sharp spikes. The electrons must be confined within a small spread in phase angle ($\leq 5^\circ$) to minimize the kinetic energy spread of the output beam.

The micropulses enter the accelerator at a phase between 0° and 90° . As we saw in Section 13.6, the average phase of the pulse increases until the electrons are ultra-relativistic. For the remainder of the acceleration cycle, acceleration takes place near a constant phase called the *asymptotic phase*. The injection phase of the micropulses and the accelerating gradient are adjusted to give an asymptotic phase of 90° . This choice gives the highest acceleration gradient and the smallest energy spread in the bunch.

Output beam energy uniformity is a concern for high-energy physics experiments. The output energy spread is affected by variations in the traveling wave phase velocity. Dimensional tolerances in the waveguides on the order of 10^{-3} cm must be maintained for a 1% energy spread. The structures must be carefully machined and tuned. The temperature of the waveguides under rf power loading must be precisely controlled to prevent a shift in phase velocity from thermal expansion.

C. Beam Breakup Instability

The theory of Section 13.6 indicated that transverse focusing is unnecessary in an electron linac because of the shortened effective length. This is true only at low beam current; at high current, electrons are subject to the *beam breakup instability* [W. K. H. Panofsky and M. Bander, Rev. Sci. Instrum. **39**, 206 (1968); V. K. Neil and R. K. Cooper, Part. Accel. **1**, 111 (1970)] also known as the *transverse instability* or *pulse shortening*. The instability arises from excitation of TM_{110} cavity modes in the spaces between irises. Features of the TM_{110} mode in a cylindrical cavity are illustrated in Figure 14.4. Note that there are longitudinal electric fields of opposite polarity in the upper and lower portions of the cavity and that there is a transverse magnetic field on the axis. An electron micropulse (of sub-nanosecond duration) can be resolved into a broad spectrum of frequencies. If the pulse has relatively high current and is eccentric with respect to the cavity, interaction between the electrons and the longitudinal electric field of the TM_{110} mode

Radio-frequency Linear Accelerators

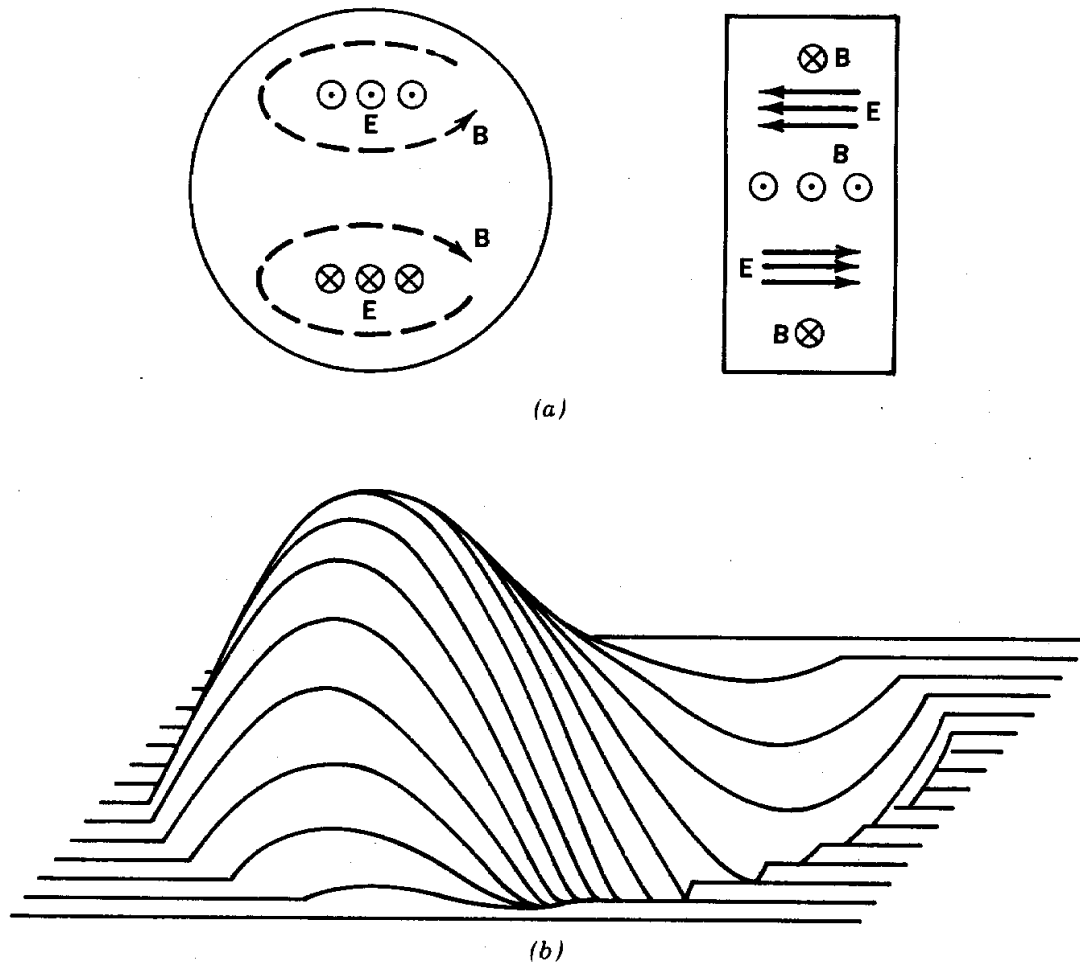


Figure 14.4 TM_{110} mode in cylindrical cavity. (a) diagram of electric and magnetic field distributions. (b) Three-dimensional plot of peak electric field amplitude as function of position.

takes place. The mode is excited near the entrance of the accelerator by the initial micropulses of the macropulse. The magnetic field of the mode deflects subsequent portions of the macropulse, causing transverse sweeping of the beam at frequency ω_{110} . The sweeping beam can transfer energy continually to TM_{110} excitations in downstream cavities. The result is that beam sweeping grows from the head to the tail of the microsecond duration macropulse and the strength of TM_{110} oscillations grows along the length of the machine. Sweeping motion leads to beam loss. The situation is worsened if the TM_{110} excitation can propagate backward along the iris-loaded waveguide toward the entrance to the accelerator or if the beam makes many passes through the same section of accelerator (as in the microtron). This case is referred to as the *regenerative beam breakup instability*.

Radio-frequency Linear Accelerators

The beam breakup instability has the following features.

1. Growth of the instability is reduced by accurate injection of azimuthally symmetric beams.
2. The energy available to excite undesired modes is proportional to the beam current. Instabilities are not observed below a certain current; the cutoff depends on the macropulse length and the Q values of the resonant structure.
3. The amplitude of undesired modes grows with distance along the accelerator and with time. This explains pulse shortening, the loss of late portions of the electron macropulse.
4. Mode growth is reduced by varying the accelerator structure. The phase velocity for TM_{01} traveling waves is maintained constant, but the resonant frequency for TM_{110} standing waves between irises is changed periodically along the accelerator.

Transverse focusing elements are necessary in high-energy electron linear accelerators to counteract the transverse energy gained through instabilities. Focusing is performed by solenoid lenses around the waveguides or by magnetic quadrupole lenses between guide sections.

D. Frequency Equation

The dispersion relationship for traveling waves in an iris-loaded waveguide was introduced in Section 12-10. We shall determine the approximate relationship between the inner and outer radii of the irises for waves with phase velocity $\omega/k = c$ at a specified frequency. The *frequency equation* is a first-order guide. A second-order waveguide design is performed with computer calculations and modeling experiments.

Assume that δ , the spacing between irises, is small compared to the wavelength of the traveling wave; the boundary fields approximate a continuous function. The tube radius is R_o and the aperture radius is R . The complete solution consists of standing waves in the volume between the irises and a traveling wave matched to the reactive boundary at $r = R_o$. The solution must satisfy the following boundary conditions:

$$E_z(\text{standing wave}) = 0 \quad \text{at } r = R_o, \quad (14.1)$$

$$E_z(\text{traveling wave}) \cong E_z(\text{standing wave}) \quad \text{at } r = R, \quad (14.2)$$

$$B_\theta(\text{traveling wave}) \cong B_\theta(\text{standing wave}) \quad \text{at } r = R. \quad (14.3)$$

The last two conditions proceed from the fact that \mathbf{E} and \mathbf{B} must be continuous in the absence of surface charges or currents.

Radio-frequency Linear Accelerators

Following Section 12.3, the solution for azimuthally symmetric standing waves in the space between the irises is

$$E_z(r,t) = A J_0(\omega r/c) + B Y_0(\omega r/c). \quad (14.4)$$

The Y_0 term is retained because the region does not include the axis. Applying Eq. (14.1), Eq. (14.4) becomes

$$E_z = E_o [Y_0(\omega R_o/c) J_0(\omega r/c) - J_0(\omega R_o/c) Y_0(\omega r/c)]. \quad (14.5)$$

The toroidal magnetic field is determined from Eq. (12.45) as

$$B_\theta = - (jE_o/c) [Y_0(\omega R_o/c) J_1(\omega r/c) - J_0(\omega R_o/c) Y_1(\omega r/c)]. \quad (14.6)$$

The traveling wave has an electric field of the form $E_z = E_o \exp[j(kz - \omega t)]$. We shall see in Section 14.4 that the axial electric field of the traveling wave is approximately constant over the aperture. Therefore, the net displacement current carried by a wave with phase velocity equal to c is

$$I_d = \pi R^2 (\partial E_z / \partial t) / \mu_o c^2 = - (j\omega / \mu_o c^2) (\pi R^2) E_o \exp[j(kz - \omega t)]. \quad (14.7)$$

The toroidal magnetic field of the wave at $r = R$ is

$$B_\theta = - (j\omega R/2c^2) E_o \exp[j(kz - \omega t)]. \quad (14.8)$$

The frequency equation is determined by setting E_z/B_θ for the cavities and for the traveling wave equal at $r = R$ [Eqs. (14.2) and (14.3)]:

$$\omega R/c = \frac{2 [Y_0(\omega R_o/c) J_1(\omega R/c) - J_0(\omega R_o/c) Y_1(\omega R/c)]}{Y_0(\omega R_o/c) J_0(\omega R/c) - J_0(\omega R_o/c) Y_0(\omega R/c)}. \quad (14.9)$$

Equation (14.9) is a transcendental equation that determines ω in terms of R and R_o to generate a traveling wave with phase velocity equal to the speed of light. A plot of the right-hand side of the equation is given in Figure 14.5. A detailed analysis shows that power flow is maximized and losses minimized when there are about four irises per wavelength. Although the assumptions underlying Eq. (14.9) are not well satisfied in this limit, it still provides a good first-order estimate.

Radio-frequency Linear Accelerators

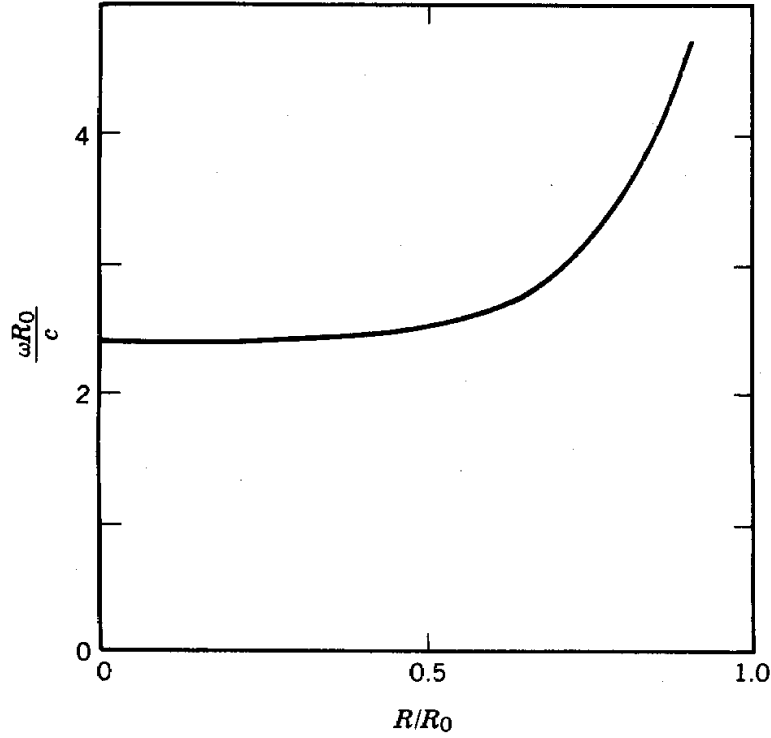


Figure 14.5 Frequency of TM_{01} mode with $\omega/k = c$ in iris-loaded cylindrical waveguide as function of R/R_0 , where R is iris inner radius and R_0 is inner radius of waveguide.

E. Electromagnetic Energy Flow

Radio-frequency power is inserted into the waveguides periodically at locations separated by a distance l . For a given available total power P , and accelerator length L , we can show that there is an optimum value of l such that the final beam energy is maximized. In analogy with standing wave cavities, the quantity Q characterizes resistive energy loss in the waveguide according to

$$-(dP/dz) = U\omega/Q. \quad (14.10)$$

In Eq. (14.10), dP/dz is the power lost per unit length along the slow-wave structure and U is the electromagnetic energy per unit length. Following the discussion of Section 12.10, the group velocity of the traveling waves is equal to

$$v_g = \frac{\text{energy flux}}{\text{electromagnetic energy density}}.$$

Multiplying the numerator and denominator by the area of the waveguide implies

Radio-frequency Linear Accelerators

$$Uv_g = P, \quad (14.11)$$

where P is the total power flow. Combining Eqs. (14.10) and (14.11), $-(dP/dz) = (\omega/Qv_g) P$, or

$$P(z) = P_o \exp(-\omega z/Qv_g), \quad (14.12)$$

where P_o is the power input to a waveguide section at $z = 0$. The electromagnetic power flow is proportional to the Poynting vector $\mathbf{S} = \mathbf{E} \times \mathbf{H} \sim E_z^2$ where E_z is the magnitude of the peak axial electric field. We conclude that electric field as a function of distance from the power input is described by

$$E_z(z) = E_{zo} \exp(-z/l_o), \quad (14.13)$$

where $l_o = 2Qv_g/\omega$. An electron traveling through an accelerating section of length l gains an energy

$$\Delta T = e \int_0^l E_z(z) dz. \quad (14.14)$$

Substituting from Eq. (14.13) gives

$$\Delta T = eE_{zo}l [1 - \exp(-l/l_o)] / (l/l_o). \quad (14.15)$$

In order to find an optimum value of l , we must define the following constraints:

1. The total rf power P_t and total accelerator length L are specified. The power input to an accelerating section of length l is $\Delta P = P_t (l/L)$.

2. The waveguide properties Q , v_g , and ω are specified.

The goal is to maximize the total energy $T = \Delta T (L/l)$ by varying the number of power input points. The total power scales as

$$P_t \sim (v_g E_{zo}^2) (L/l),$$

where the first factor is proportional to the input power flux to a section and the second factor is the number of sections. Therefore, with constant power, E_{zo} scales as \sqrt{l} . Substituting the scaling for E_{zo} in Eq. (14.15) and multiplying by L/l , we find that the beam output energy scales as

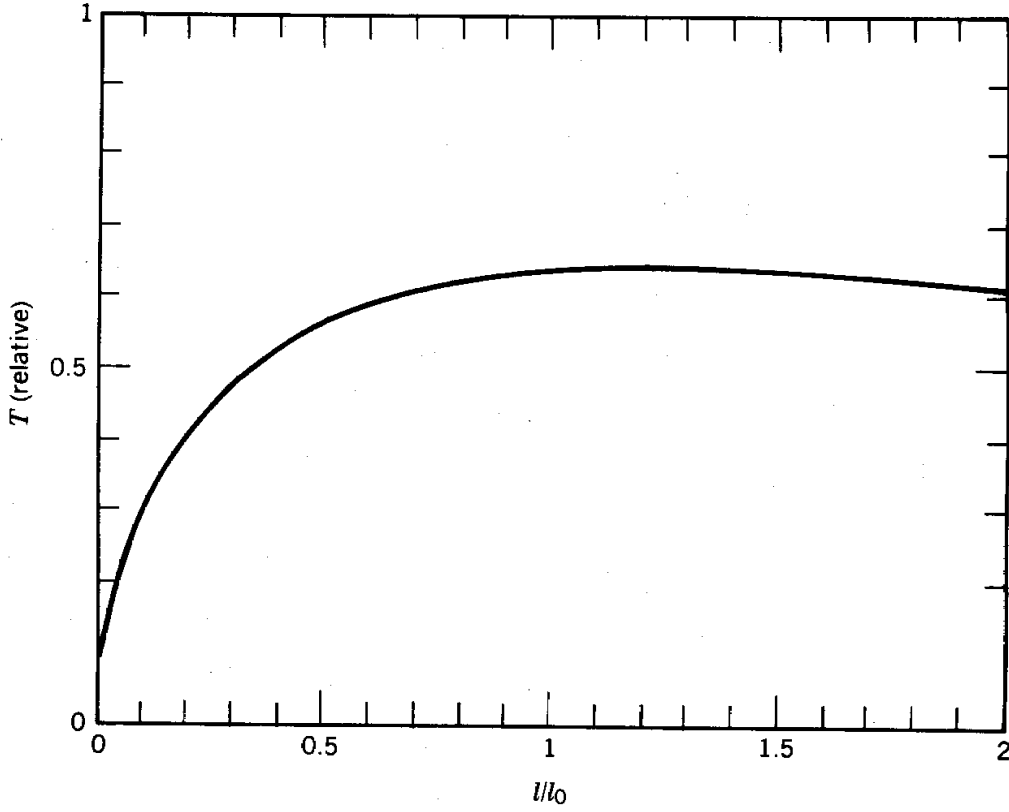


Figure 14.6 Relative output beam kinetic energy from traveling wave electron accelerator as function of l/l_0 , where $l_0 = 2Qv_g/\omega$: Q is quality factor of waveguide, v_g is group velocity of traveling waves in slow-wave structure, and ω is rf angular frequency).

$$T \sim \sqrt{l} [1 - \exp(-l/l_0)]/l$$

or

$$T \sim [1 - \exp(-l/l_0)] / \sqrt{l/l_0}. \quad (14.16)$$

Inspection of Figure 14.6 shows that T is maximized when $l/l_0 = 1.3$; the axial electric field drops to 28% of its initial value over the length of a section. It is preferable from the point of view of particle dynamics to maintain a constant gradient along the accelerator. Figure 14.6 implies that l/l_0 can be reduced to 0.8 with only a 2% drop in the final energy. In this case, the output electric field in a section is 45% of the initial field.

Fields can also be equalized by varying waveguide properties over the length of a section. If the

Radio-frequency Linear Accelerators

wall radius and the aperture radius are decreased consistent with Eq. (14.9), the phase velocity is maintained at c while the axial electric field is raised for a given power flux. Waveguides can be designed for constant axial field in the presence of decreasing power flux. In practice, it is difficult to fabricate precision waveguides with continuously varying geometry. A common compromise is to divide an accelerator section into subsections with varying geometry. The sections must be carefully matched so that there is no phase discontinuity between them. This configuration has the additional benefit of reducing the growth of beam breakup instabilities.

F. Shunt Impedance

The *shunt impedance* is a figure-of-merit quantity for electron and ion linear accelerators. It is defined by

$$P_t = V_o^2 / (Z_s L), \quad (14.17)$$

where P_t is the total power dissipated in the cavity walls of the accelerator, V_o is the total accelerator voltage (the beam energy in electron volts divided by the particle charge), and L is the total accelerator length. The shunt impedance Z_s has dimensions of ohms per meter. An alternate form for shunt impedance is

$$Z_s = \overline{E_z^2} / (dP/dz), \quad (14.18)$$

where dP/dz is the resistive power loss per meter. The power loss of Eq. (14.17) has the form of a resistor of value $Z_s L$ in parallel with the beam load. This is the origin of the term shunt impedance.

The efficiency of a linear accelerator is given by

$$\text{energy efficiency} = Z_b / (Z_b + Z_s L), \quad (14.19)$$

where Z_b is the beam impedance, $Z_b = V_o / i_b$. The shunt impedance for most accelerator rf structures lies in the range of 25 to 50 M Ω /m. As an example, consider a 2.5-GeV linear electron accelerator with a peak on-axis gradient of 8 MV/m. The total accelerator length is 312 m. With a shunt impedance of 50 M Ω /m, the total parallel resistance is 1.6×10^{10} Ω . Equation (14.17) implies that the power to maintain the high acceleration gradient is 400 MW.

14.2 LINEAR ION ACCELERATOR CONFIGURATIONS

Linear accelerators for ions differ greatly from electron machines. Ion accelerators must support

Radio-frequency Linear Accelerators

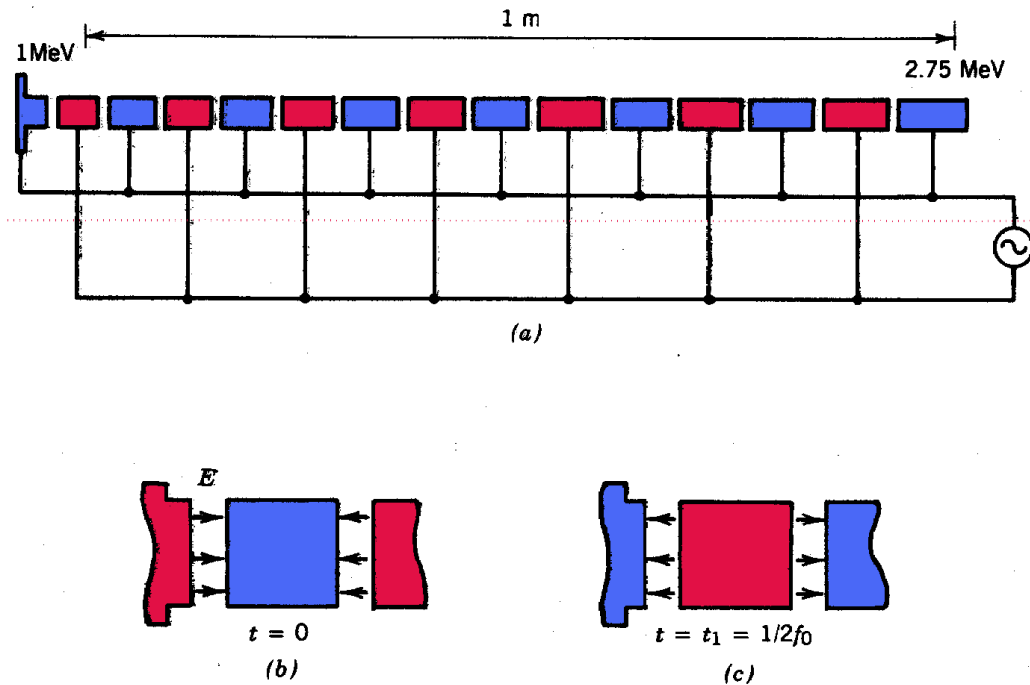


Figure 14.7 Wideröe linear accelerator for heavy ions. (a) Scale drawing of accelerator with following parameters: Ion species: Cs-137, $f = 10$ MHz, $T_i = 1$ MeV, $V_0 = 100$ kV, and $\phi_s = 60^\circ$. (b) Electric fields in acceleration gaps 1 and 2 at ion injection ($t = 0$). (c) Electric fields at time $t = 1/2f$, where f is the rf frequency.

traveling wave components with phase velocity well below the speed of light. In the energy range accessible to linear accelerators, ions are non-relativistic; therefore, there is a considerable change in the synchronous particle velocity during acceleration. Slow-wave structures are not useful for ion acceleration. An iris-loaded waveguide has small apertures for $\omega/k \ll c$. The conduction of electromagnetic energy via slow waves is too small to drive a multi-cavity waveguide. Alternative methods of energy coupling are used to generate traveling wave components with slow phase velocity.

An ion linear accelerator typically consists of a sequence of cylindrical cavities supporting standing waves. Cavity oscillations are supported either by individual power feeds or through inter-cavity coupling via magnetic fields. The theory of ion accelerators is most effectively carried out by treating cavities as individual oscillators interacting through small coupling terms.

Before studying rf linear ion accelerators based on microwave technology, we will consider the Wideröe accelerators [R. Wideroe, Arch. Elektrotechn. **21**, 387 (1928)] (Fig. 14.7a), the first successful linear accelerator. The Wideröe accelerator operates at a low frequency (1-10 MHz); it still has application for initial acceleration of heavy ions. The device consists of a number of tubes concentric with the axis connected to a high-voltage oscillator. At a particular time, half the tubes are at negative potential with respect to ground and half the tubes are positive. Electric fields are concentrated in narrow acceleration gaps; they are excluded from the interior of the

Radio-frequency Linear Accelerators

tubes. The tubes are referred to as *drift tubes* because ions drift at constant velocity inside the shielded volume. Assume that the synchronous ion crosses the first gap at $t = 0$ when the fields are aligned as shown in Figure 14.7b. The ion is accelerated across the gap and enters the zero-field region in the first drift tube. The ion reaches the second gap at time

$$\Delta t_1 = L_1/v_{s1}. \quad (14.20)$$

The axial electric fields at $t = t_1$ are distributed as shown in Figure 14.7c if t_1 is equal to half the rf period, or

$$\Delta t_1 = \pi/\omega. \quad (14.21)$$

The particle is accelerated in the second gap when Eq. (14.21) holds.

It is possible to define a synchronous orbit with continuous acceleration by increasing the length of subsequent drift tubes. The velocity of synchronous ions following the n th gap is

$$V_1 (LC_c \omega_o^2) + V_2 (1 - LC \omega^2 - LC_c \omega_o^2) = 0. \quad (14.22)$$

here T_o is the injection kinetic energy, V_o is the peak gap voltage, and ϕ_s is the synchronous phase. The length of drift tube n is

$$L_n = v_n (\pi/\omega). \quad (14.23)$$

The drift tubes of Figure 14.7a are drawn to scale for the acceleration of Hg^+ ions injected at 2 MeV with a peak gap voltage of 100 kV and a frequency of 4 MHz.

The Wideröe accelerator is not useful for light-ion acceleration and cannot be extrapolated to produce high-energy heavy ions. At high energy, the drift tubes are unacceptably long, resulting in a low average accelerating gradient. The drift tube length is reduced if the rf frequency is increased, but this leads to the following problems:

1. The acceleration gaps conduct large displacement currents at high frequency, loading the rf generator.
2. Adjacent drift tubes act as dipole antennae at high frequency with attendant loss of rf energy by radiation.

The high-frequency problems are solved if the acceleration gap is enclosed in a cavity with resonant frequency ω . The cavity walls reflect the radiation to produce a standing electromagnetic oscillation. The cavity inductance in combination with the cavity and gap capacitance constitute an LC circuit. Displacement currents are supported by the electromagnetic oscillations. The power supply need only contribute energy to compensate for resistive losses and beam loading.

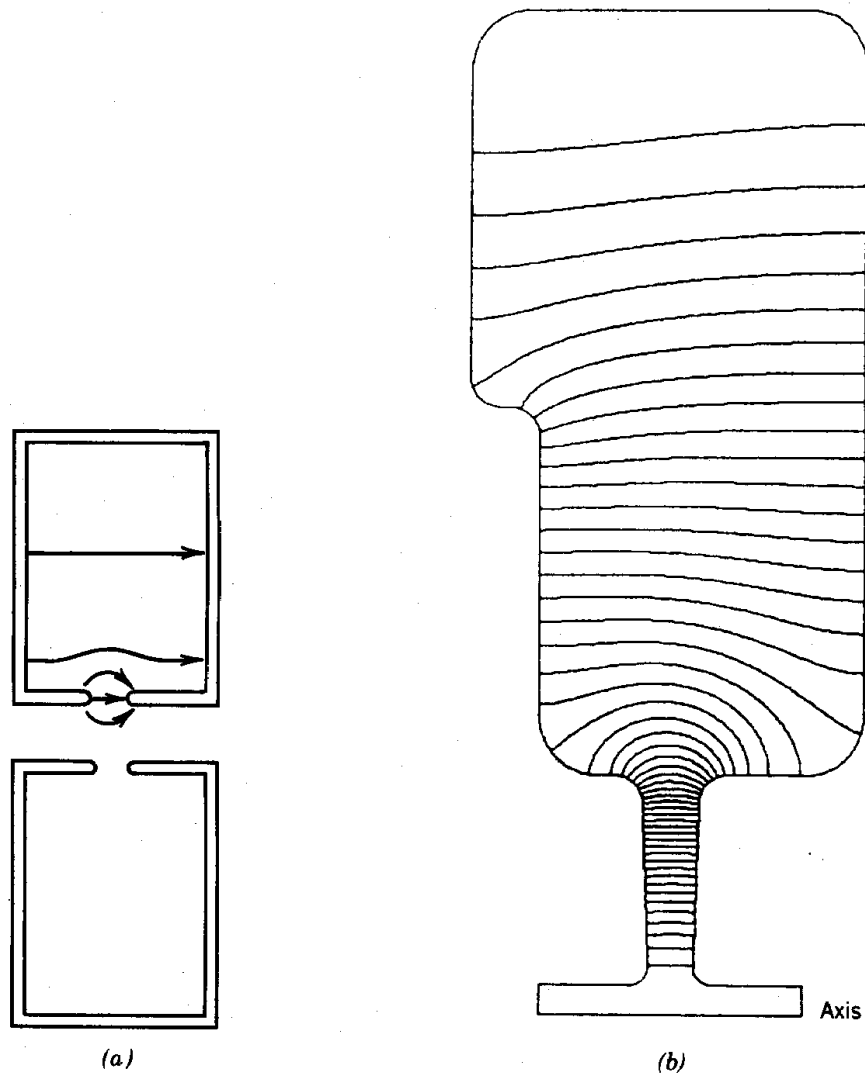


Figure 14.8 Resonant cavities for particle acceleration. (a) Electric fields in cylindrical cavity with “noses” to define beam drift space. (b) Computer calculation of electric fields of an acceleration cavity using the SUPERFISH code; $f = 454$ MHz. (Courtesy G. Boicourt, Los Alamos National Laboratory.)

A resonant cavity for ion acceleration is shown in Figure 14.8a. The TM_{010} mode produces good electric fields for acceleration. We have studied the simple cylindrical cavity in Section 12.3. The addition of drift tube extensions to the cylindrical cavity increases the capacitance on axis, thereby lowering the resonant frequency. The resonant frequency can be determined by a perturbation analysis or through the use of computer codes. The electric field distribution for a linac cavity computed by the program SUPERFISH is shown in Figure 14.8b.

Linear ion accelerators are composed of an array of resonant cavities. We discussed the synthesis of slow waves by independently phased cavities in Section 12.9. Two frequently

Radio-frequency Linear Accelerators

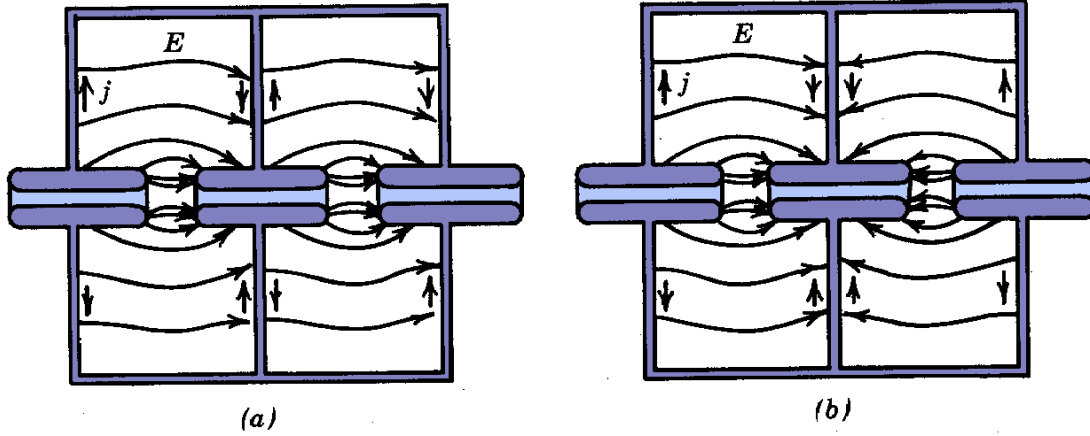


Figure 14.9 Electric field lines and wall currents of TM_{010} modes in two cavities of standing wave linear accelerator: (a) $\beta\lambda$ linac, (b) $\frac{1}{2}\beta\lambda$ linac.

encountered cases of cavity phasing are illustrated in Figures 14.9a and 14.9b. In the first, the electric fields of all cavities are in phase, while in the second there is a phase change of 180° between adjacent cavities. The synchronous condition for the in-phase array is satisfied if ions traverse the inter-gap distance L_n in one rf period:

$$L_n = v_n (2\pi/\omega) = \beta\lambda, \quad (14.24)$$

where $\beta = v_n/c$ and $\lambda = 2\pi c/\omega$. Hence, an accelerator with the phasing of Figure 14.9a is referred to as a $\beta\lambda$ linac. Similarly, the accelerator of Figure 14.9b is a $\beta\lambda/2$ linac because the synchronous condition implies that

$$L_n = \beta\lambda/2. \quad (14.25)$$

In this notation, the Wideröe accelerator is a $\beta\lambda/2$ structure.

The advantages of an individually-phased array are that all cavities are identical and that a uniform accelerating gradient can be maintained. The disadvantage is technological; each cavity requires a separate rf amplifier and waveguide. The cost of the accelerator is reduced if a number of cavities are driven by a single power supply at a single feed point. Two geometries that accomplish this are the *drift tube* or *Alvarez linac* [L.W. Alvarez, Phys. Rev. **70**, 799 (1946)] and the *coupled cavity array*. We shall study the drift tube accelerator in the remainder of this section. Coupled cavities are treated in Section 14.3.

The concept of the drift tube linac is most easily understood by following an evolution from the independently-phased array. The $\beta\lambda$ cavity array of Figure 14.10a is an improvement over the independently phase array in terms of reduction of microwave hardware. There are separate power feeds but only one amplifier. Synchronization of ion motion to the rf oscillations is accomplished by varying the drift lengths between cavities. The structure of Figure 14.10b is

Radio-frequency Linear Accelerators

a mechanically simplified version in which the two walls separating cavities are combined. In the absence of the drift tubes, the cavities have the same resonant frequency because ω_{010} does not depend on the cavity length (Table 12.1). This reflects the fact that the capacitance of a cylindrical cavity scales as $1/d$ while the inductance increases as d . The additional capacitance of the acceleration gap upsets the balance. It is necessary to adjust the gap geometry in different cavities to maintain a constant resonant frequency. The capacitance is determined by the drift tube diameter and the gap width. Figure 14.10b illustrates variation of drift tube diameter to compensate for increasing cavity length along the direction of acceleration. Resonant frequencies of individual cavities must be matched to within a factor of $1/Q$ so that all cavities are excited by the driving wave; a typical requirement is 1 part in 10^4 . The design procedure for a cavity array often consists of the following stages:

1. Approximate dimensions are determined by analytic or computer calculations.
2. Measurements are performed on a low-power model.
3. The final cavity array is tuned at low power. Small frequency corrections can be made by deforming cavity walls (dimpling) or by adjusting tuning slugs which change the capacitance or inductance of individual cavities.

The electric fields and wall currents for the TM_{010} mode in a $\beta\lambda$ structure are illustrated in Figure 14.9a. Note the distribution of electric field and current on the wall separating two cavities:

1. The currents in the two cavities are opposite and approximately equal; therefore, the wall carries zero net current.
2. Electric fields have equal magnitude and direction on both sides of the wall; therefore, the surface charge densities on the two sides of the wall have equal magnitude and opposite sign. There is zero net charge per area on the wall.

The field pattern is almost unchanged if the wall is removed (Fig. 14.10c). Eliminating the intervening walls leads to the drift tube accelerator of Figure 14.10c. Shaped drift tubes with increasing length along the direction of acceleration are supported by rods. The rods are located at positions of zero radial electric field; they do not seriously perturb the field distribution. An alternate view of the DTL is that it is a long cylindrical cavity with a single rf power feed to drive the TM_{010} mode; the variation of drift tube length and diameter maintains synchronization with accelerated particles and compensates the tube perturbations to maintain a constant axial electric field.

Magnetic quadrupole lenses for beam focusing are located inside the drift tubes. Power and cooling water for the magnets enter along the tube supports. The development of strong permanent magnetic materials (such as orientated samarium-cobalt) has generated interest in adjustable permanent magnet quadrupole lenses. One of the main operational problems in DTLs is

Radio-frequency Linear Accelerators

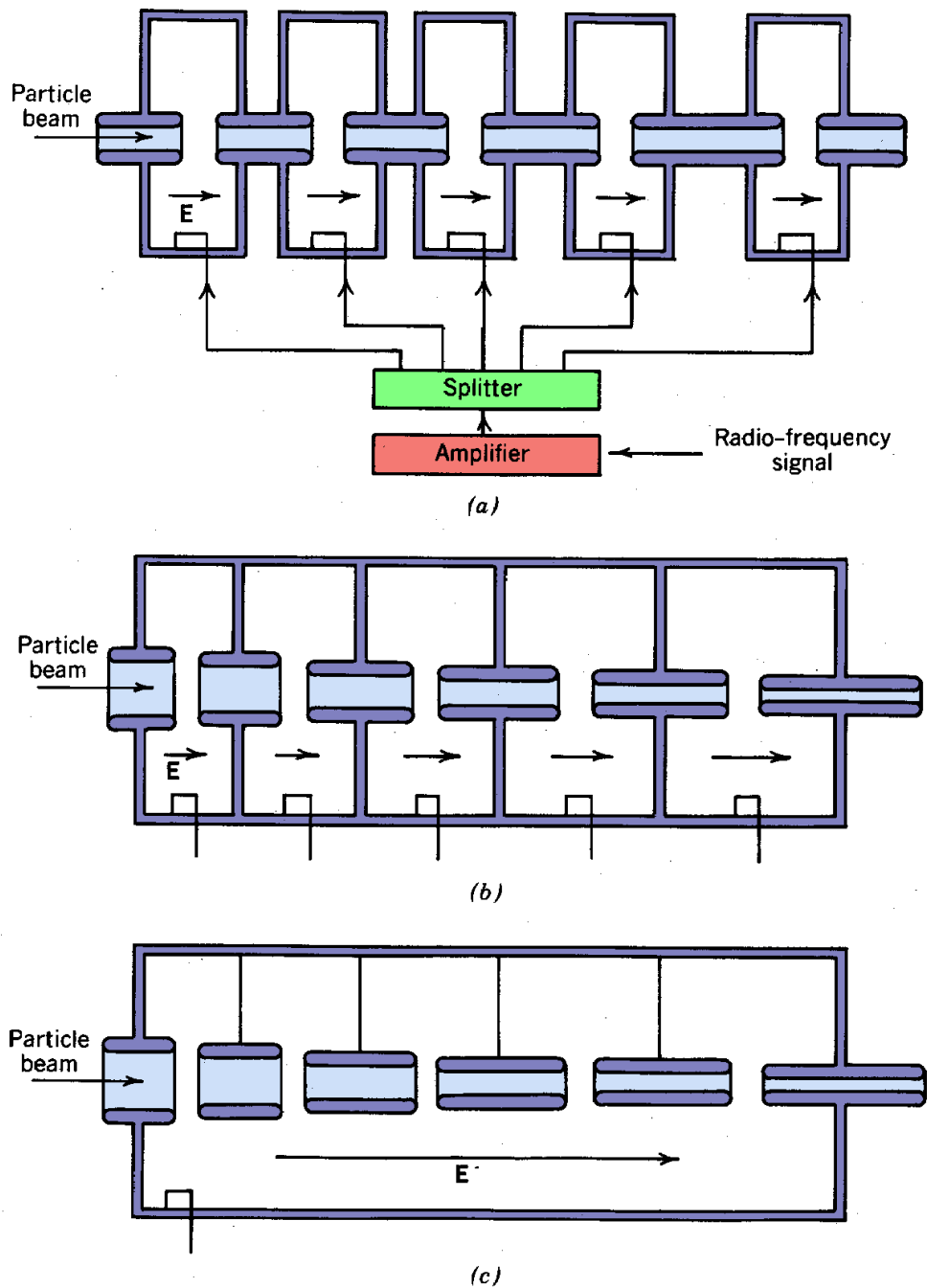
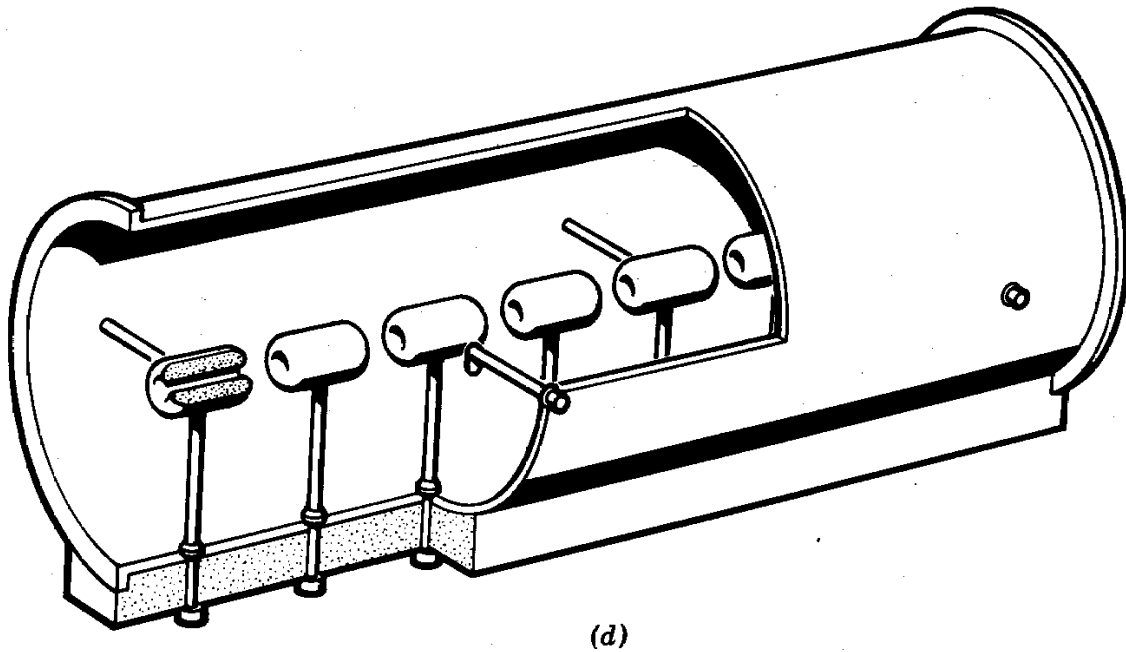


Figure 14.10 Evolution of drift tube linear accelerator. (a) Array of resonant cavities in the $\beta\lambda$ configuration with particle synchronization maintained by variation of distance between cavities. (b) Simplified $\beta\lambda$ structure with synchronization by varying cavity length; uniform resonant frequency maintained by variation of drift tube and acceleration gap geometry. (c) Alvarez linac tank. (d) Drift tube linac with postcouplers to shift the frequency of undesired rf modes. (Courtesy R. Jameson, Los Alamos National Laboratory.)



(d)
Figure 14.10 (Continued).

maintaining the TM_{010} mode in a complex structure with many competing modes. Contributions of modes with transverse electric fields are particularly dangerous because they lead to beam loss. An effective solution to stabilize the rf oscillations is to incorporate tuning elements in the structure. Post couplers are illustrated in Figure 14.10d. The posts are orthogonal to the drift tube supports. They have little effect on the fundamental acceleration mode which has only longitudinal electric fields. On the other hand, the combination of drift tube support and post coupler causes a significant perturbation of other modes that have transverse electric fields. The effect is to shift the frequency of competing modes away from that of the fundamental so that they are less likely to be excited. A second purpose of the post couplers is to add periodic loading of the drift tube structures. Rotation of the post adds a small shunt capacitance to selected drift tubes. The variable loading is used to adjust the distribution of fundamental mode accelerating fields along the resonant cavity.

14.3 COUPLED CAVITY LINEAR ACCELERATORS

For a constrained frequency (set by rf power tube technology) and peak electric field (set by breakdown limits), a $\beta\lambda/2$ linac has twice the average accelerating gradient as a $\beta\lambda$ structure such as the drift tube linac. For a given beam output energy, a $\beta\lambda/2$ accelerator is half as long as a $\beta\lambda$ machine. Practical $\beta\lambda/2$ geometries are based on coupled cavity arrays. In this section, we shall

analyze the coupled cavity formalism and study some practical configurations.

To begin, we treat two cylindrical resonant cavities connected by a coupling hole (Fig. 14.11a). The cavities oscillate in the TM_{010} mode. Each cavity can be represented as a lumped element LC circuit with $\omega_o = 1/\sqrt{LC}$ (Fig. 14.11b). Coupling of modes through an on-axis hole is capacitive. The electric field of one cavity makes a small contribution to displacement current in the other (Fig. 14.11c). In the circuit model we can represent the coupling by a capacitor C_c between the two oscillator circuits (Fig. 14.11b). If coupling is weak, $C_c \ll C$. Similarly, an azimuthal slot near the outer diameter of the wall between the cavities results in magnetic coupling. Some of the toroidal magnetic field of one cavity leaks into the other cavity, driving wall currents through inductive coupling (Fig. 14.11d). In the circuit model, a magnetic coupling slot is represented by a mutual inductance (Fig. 14.11e).

The following equations describe voltage and current in the circuit of Figure 14.11b:

$$-C(dV_1/dt) = I_1, \quad (14.26)$$

$$V_1 = L (dI_1/dt - di/dt), \quad (14.27)$$

$$-C(dV_2/dt) = I_2, \quad (14.28)$$

$$V_2 = L (dI_2/dt + di/dt), \quad (14.29)$$

$$i = C_c (dV_1/dt - dV_2/dt) = (C_c/C) (-I_1 + I_2). \quad (14.30)$$

When coupling is small, voltages and currents oscillate at frequency to $\omega \cong \omega_o$ and the quantity i is much smaller than I_1 or I_2 . In this case, Eq. (14.30) has the approximate form

$$i \cong (-C_c \omega_o^2) (V_1 - V_2). \quad (14.31)$$

Assuming solutions of the form $V_1, V_2 \sim \exp(j\omega t)$, Eqs. (14.26)-(14.31) can be combined to give

$$V_1 (1 - LC\omega^2 - LC_c\omega_o^2) + V_2 (LC_c\omega_o^2) = 0, \quad (14.32)$$

$$V_1 (LC_c\omega_o^2) + V_2 (1 - LC\omega^2 - LC_c\omega_o^2) = 0. \quad (14.33)$$

Substituting $\Omega = \omega/\omega_o$ and $\kappa = C_c/C$, Eqs. (14.32) and (14.33) can be written in matrix form:

$$\begin{bmatrix} 1 - \Omega^2 - \kappa & \kappa \\ \kappa & 1 - \Omega^2 - \kappa \end{bmatrix} \begin{pmatrix} V_1 \\ V_2 \end{pmatrix} = 0. \quad (14.34)$$

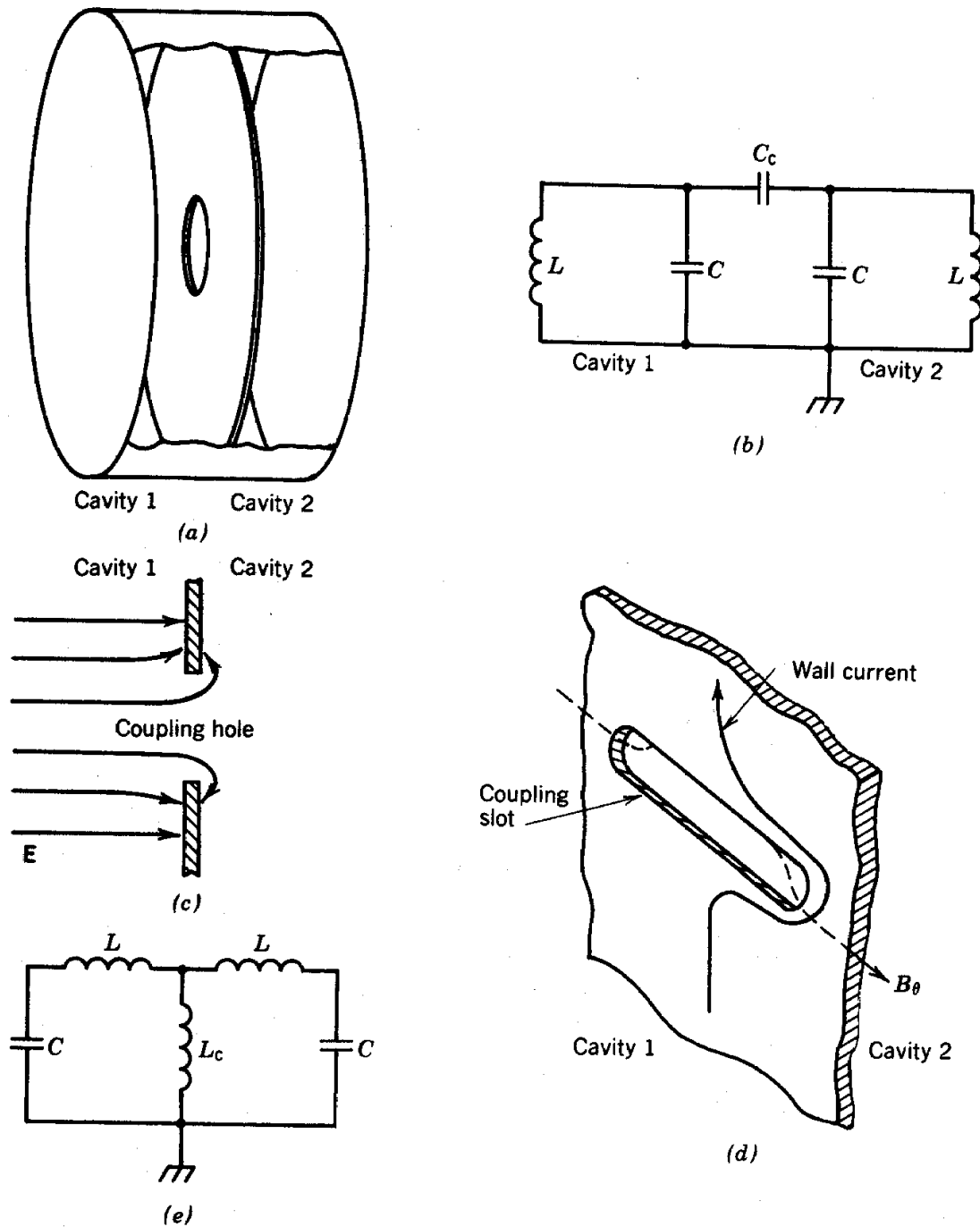


Figure 14.11 Coupled cavities. (a) Two resonant cavities with TM_{010} modes coupled capacitively through hole on-axis. (b) Equivalent circuit model of two electrically coupled cavities. (c) Electric field distribution near coupling hole with cavity 1 excited and cavity 2 unexcited. (d) Magnetic field distribution from TM_{010} mode at azimuthal slot near outer cavity radius; cavity 1 excited, cavity 2 unexcited. (e) equivalent circuit model for two magnetically coupled cavities.

Radio-frequency Linear Accelerators

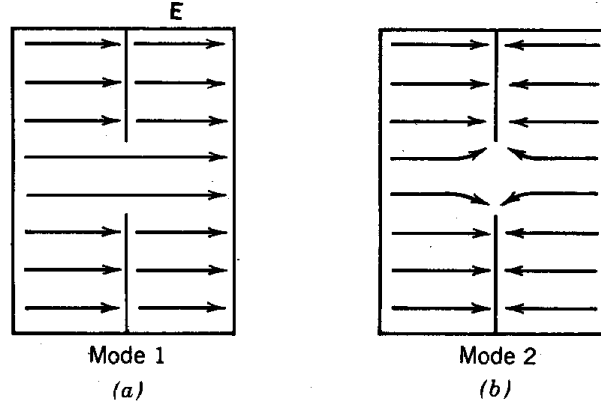


Figure 14.12 TM_{010} modes of oscillation for two capacitively coupled cavities. (a) Electric field distribution for mode 1 (0 mode). (b) Electric field distribution for mode 2 (π mode).

The equations have a nonzero solution if the determinant of the matrix equals zero, or

$$(1 - \Omega^2 - \kappa^2) - \kappa^2 = 0 \quad (14.35)$$

Equation (14.35) has two solutions for the resonant frequency:

$$\Omega_1 = \omega_1/\omega_o = \sqrt{1-2\kappa}, \quad (14.36)$$

$$\Omega_2 = \omega_2/\omega_o = 1. \quad (14.37)$$

There are two modes of oscillation for the coupled two-cavity system. Substituting Eqs. (14.36) and (14.37) into Eq. (14.32) or (14.33) shows that $V_1 = -V_2$ for the first mode and $V_1 = V_2$ for the second. Figure 14.12 illustrates the physical interpretation of the modes. In the first mode, electric fields are aligned; the coupling hole does not influence the characteristics of the oscillation (note that ω_o is the oscillation frequency of a single cavity without the central region). We have previously derived this result for the drift tube linac. In the second mode, the fields are anti-aligned. The interaction of electric fields near the hole cancels coupling through the aperture. A coupled two-cavity system can oscillate in either the $\beta\lambda$ or the $\beta\lambda/2$ mode, depending on the input frequency of the rf generator. A similar solution results with magnetic coupling.

In a coupled cavity linac, the goal is to drive a large number of cavities from a single power feed. Energy is transferred from the feed cavity to other cavities via magnetic or electric coupling. Assume that there are N identical cavities oscillating in the TM_{010} mode with uniform capacitive coupling, represented by C_c . Figure 14.13 illustrates current and voltage in the circuit model of the n th cavity. The equations describing the circuit are

Radio-frequency Linear Accelerators

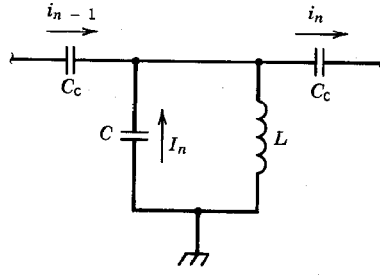


Figure 14.13 Equivalent circuit model for array of uniform, capacitively coupled resonant cavities.

$$-C (d^2 V_n / dt^2) = (dI_n / dt), \quad (14.38)$$

$$V_n = L [(dI_n / dt) - (di_n / dt) - (di_{n-1} / dt)] \quad (14.39)$$

$$di_n / dt \cong C_c \omega_o^2 (V_{n+1} - V_n). \quad (14.40)$$

The assumption of small coupling is inherent in Eq. (14.40). Taking time variations of the form $\exp(j\omega t)$, Eqs. (14.38)-14.40 can be combined into the single finite difference equation

$$V_{n+1} = [(1 - \Omega^2 - 2\kappa) / \kappa] V_n + V_{n-1} = 0, \quad (14.41)$$

where κ and Ω are defined as above.

We have already solved a similar equation for the thin-lens array in Section 8.5. Again, taking a trial solution with amplitude variations between cells of the form

$$V_n = V_o \cos(n\mu + \phi), \quad (14.42)$$

we find that

$$\cos \mu = - (1 - \Omega^2 - 2\kappa) / 2\kappa. \quad (14.43)$$

The resonant frequencies of the coupled cavity system can be determined by combining Eq. (14.43) with appropriate boundary conditions. The cavity oscillation problem is quite similar to the problem of an array of unconstrained, coupled pendula. The appropriate boundary condition is that the displacement amplitude (voltage) is maximum for the end elements of the array.

Therefore, the phase term in Eq. (14.42) is zero. Applying the boundary condition in the end cavity implies that

$$\cos[(N-1)\mu] = \pm 1. \quad (14.44)$$

Radio-frequency Linear Accelerators

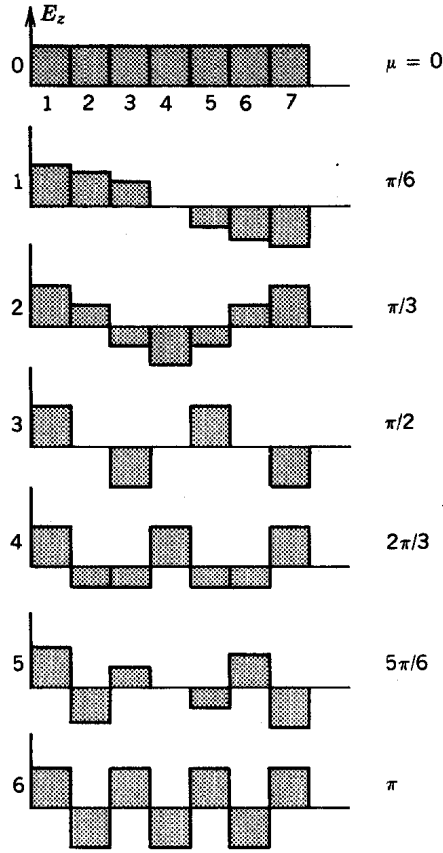


Figure 14.14 Amplitudes of axial electric fields for allowed modes of array of seven coupled cavities.

Equation (14.44) is satisfied if

$$\mu_m = \pi m / (N-1), \quad m = 0, 1, 2, \dots, N-1. \quad (14.45)$$

The quantity m has a maximum value $N-1$ because there can be at most N different values of V_n in the coupled cavity system.

A coupled system of N cavities has N modes of oscillation with frequencies given by

$$\Omega_m = \omega_m / \omega_o = \sqrt{1 - 2\kappa [1 - \cos(2\pi m / (N-1))]} \quad (14.46)$$

The physical interpretation of the allowed modes is illustrated in Figure 14.14. Electric field amplitudes are plotted for the seven modes of a seven-cavity system. In microwave nomenclature, the modes are referenced according to the value of μ . The 0 mode is equivalent to a $\beta\lambda$ structure while the π mode corresponds to $\beta\lambda/2$.

At first glance, it appears that the π mode is the optimal choice for a high-gradient accelerator. Unfortunately, this mode cannot be used because it has a very low energy transfer rate between

Radio-frequency Linear Accelerators

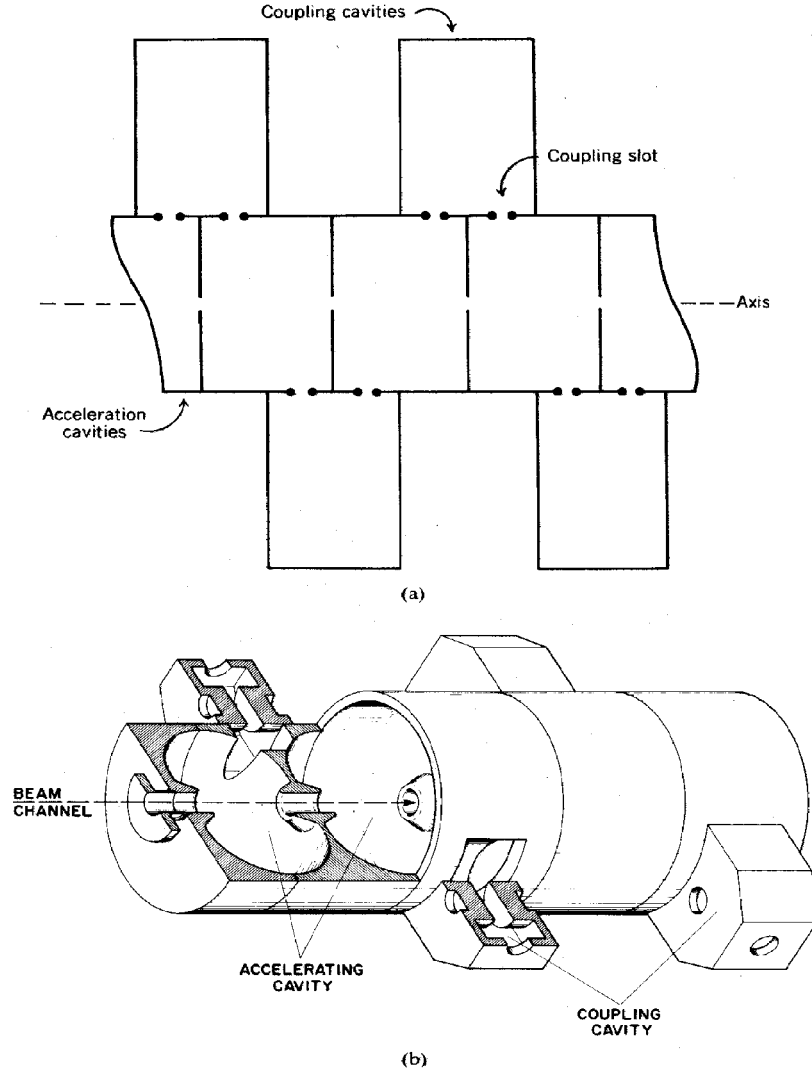


Figure 14.15 Side-coupled linear accelerator with resonant coupling a) Schematic diagram. b) Scale cross section of LAMF accelerator cavities (Courtesy O. B. van Dyck, Los Alamos National Laboratory.)

cavities. We can demonstrate this by calculating the group velocity of the traveling wave components of the standing wave. In the limit of a large number of cavities, the positive-going wave can be represented as

$$V_+(z,t) = \exp[j(\mu z/d - \omega t)]. \quad (14.47)$$

The wavenumber k is equal to μ/d . The phase velocity is

$$\omega/k = \omega_o \Omega d/\mu, \quad (14.48)$$

Radio-frequency Linear Accelerators

where ω_o is the resonant frequency of an uncoupled cavity. For the π mode, Eq. (14.48) implies

$$d = (\omega/k) \pi/\omega_o \Omega = (\beta\lambda/2)/\Omega. \quad (14.49)$$

Equation (14.49) is the $\beta\lambda/2$ condition adjusted for the shift in resonant oscillation caused by cavity coupling.

The group velocity is

$$d\omega/dk = (\omega_o d) d\Omega/d\mu = - (\omega_o d) \frac{\kappa \sin \mu}{\sqrt{1-2\kappa+2\kappa \cos \mu}}.$$

Note that v_g is zero for the 0 and π modes, while energy transport is maximum for the $\pi/2$ mode.

The $\pi/2$ mode is the best choice for rf power coupling but it has a relatively low gradient because half of the cavities are unexcited. An effective solution to this problem is to displace the

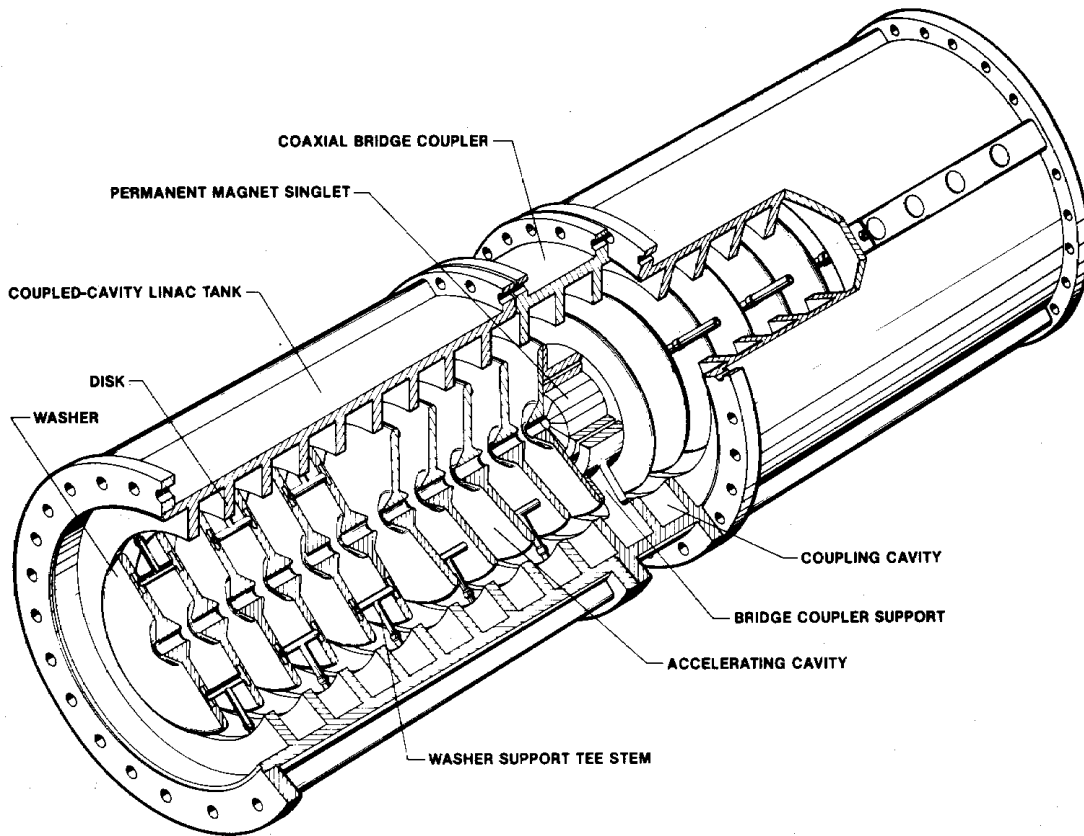
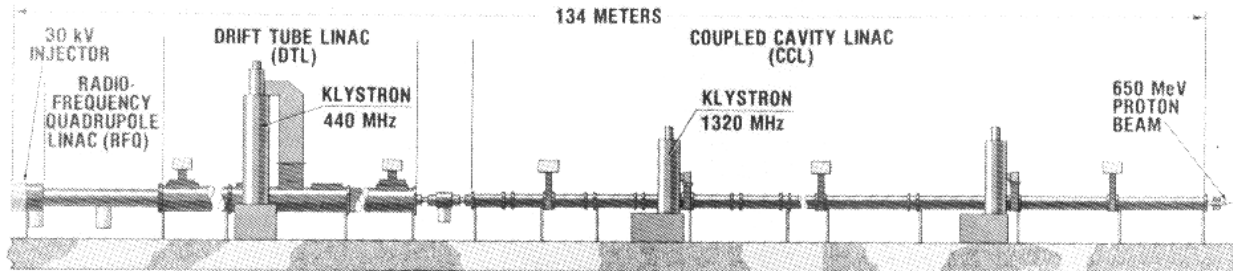


Figure 14.16 Cutaway view of a disk-and-washer accelerator structure. (Courtesy D. Swenson, Los Alamos National Laboratory and Texas A & M University).

PION GENERATOR FOR MEDICAL IRRADIATION (PIGMI)



MAJOR TECHNICAL INNOVATIONS

HIGHER FREQUENCIES
HIGHER GRADIENTS
LOWER INJECTION ENERGY
RFQ LINAC STRUCTURE
POST-COUPLED DTL STRUCTURE
PERMANENT MAGNET QUADRUPOLE LENSES
DISK AND WASHER CCL STRUCTURE
COAXIAL BRIDGE COUPLERS
DISTRIBUTED MICROPROCESSOR CONTROL

PROTON BEAM PARAMETERS

INJECTION ENERGY	30 keV
RFQ/DTL TRANSITION ENERGY	2.5 MeV
DTL/CCL TRANSITION ENERGY	125 MeV
FINAL ENERGY	650 MeV
PEAK BEAM CURRENT	28 mA
PULSE LENGTH	60 μ s
REPETITION RATE	60 Hz
AVERAGE BEAM CURRENT	100 μ A

PROTON LINAC PARAMETERS

	FREQUENCY	KLYSTRONS	GRADIENT
RFQ & DTL SECTION	440 MHz	1	6 MV/m
CCL SECTION	1320 MHz	6	8 MV/m

Figure 14.17 Diagram and parameters of PIGMI accelerator. (Courtesy D. Swenson, Los Alamos National Laboratory and Texas A & M University).

Radio-frequency Linear Accelerators

TABLE 14.2 Parameters of the LAMPF Accelerator

Accelerator length	800 m
Output beam energy	800 MeV
Output beam current	15 mA
Macropulselength	1 ms
Repetition rate	120 Hz
Duty cycle	12%
<i>Injector</i>	
Ion species	H ⁺ , H ⁻
Maximum output current	30 mA, H ⁺
Voltage	750 kV
Voltage generator	Cockcroft–Walton generator
Bunchers	201.25 MHz, 4-kV prebuncher, 10-kV main buncher
<i>Drift Tube Linac</i>	
Energy variation	0.75–100 MeV
Length	61.7 m
Operating frequency	201.25 MHz
Cavity Q	5×10^4
rf filling time	200 μ s
Number of tanks	4
Tank diameter	0.9 m
Number of drift tubes	165
Drift tube outer diameter	0.16 m
Drift tube bore	0.75–1.5 cm
Shunt impedance	42 M Ω /m
Average axial field	1.6–2.4 MV/m peak
Maximum surface field	12 MV/m
Synchronous phase	64°
rf power units	Triode power amplifiers
Number of rf units	4
rf power rating/unit	2.7 MW
Number of focusing quadrupoles	135
Focusing magnetic field gradient	8 to 0.8 kG/cm
Focusing mode	FDFD
System normalized acceptance	7π mm · mrad

Radio-frequency Linear Accelerators

Side-Coupled Linac

Energy variation	100–800 MeV
Total length	726.9 m
Operating frequency	805 MHz
Cavity Q	$1.6 \text{ to } 2.4 \times 10^4$
rf filling time	0.15 ms
Number of tanks	104
Tank length	2.9 to 7.8 m
Number of cavities	5000
Bore diameter	3.2–3.8 cm
Shunt impedance	30–42 M Ω /m
Average axial field	1.1 MV/m
Synchronous phase	64–70°
rf power units	Klystrons
Number of rf power units	44
rf power rating/unit	1.25 MW
Number of focusing quadrupoles	204
Focusing magnetic field gradient	2.2 to 3.2 kG/cm
Focusing mode	Doublets
Normalized acceptance	$17\pi \text{ mm} \cdot \text{mrad}$

unexcited cavities to the side and pass the ion beam through the even-numbered cavities. The result is a $\beta\lambda/2$ accelerator with good power coupling. The side-coupled linac [See B. C. Knapp, E. A. Knapp, G. J. Lucas, and J. M. Potter, IEEE Trans. Nucl. Sci. **NS-12**, 159 (1965)] is illustrated in Figure 14.15a. Intermediate cavities are coupled to an array of cylindrical cavities by magnetic coupling slots. Low-level electromagnetic oscillations in the side cavities act to transfer energy along the system. There is little energy dissipation in the side cavities. Figure 14.15b illustrates an improved design. The side cavities are reentrant to make them more compact (see Section 12.2). The accelerator cavity geometry is modified from the simple cylinder to reduce shunt impedance. The simple cylindrical cavity has a relatively high shunt impedance because wall current at the outside corners dissipates energy while making little contribution to the cavity inductance.

The disk and washer structure (Fig. 14.16) is an alternative to the side-coupled linac. It has high shunt impedance and good field distribution stability. The accelerating cavities are defined by "washers." The washers are suspended by supports connected to the wall along a radial electric field null. The coupling cavities extend around the entire azimuth. The individual sections of the disk-and-washer structure are strongly coupled. The perturbation analysis we used to treat coupled

Radio-frequency Linear Accelerators

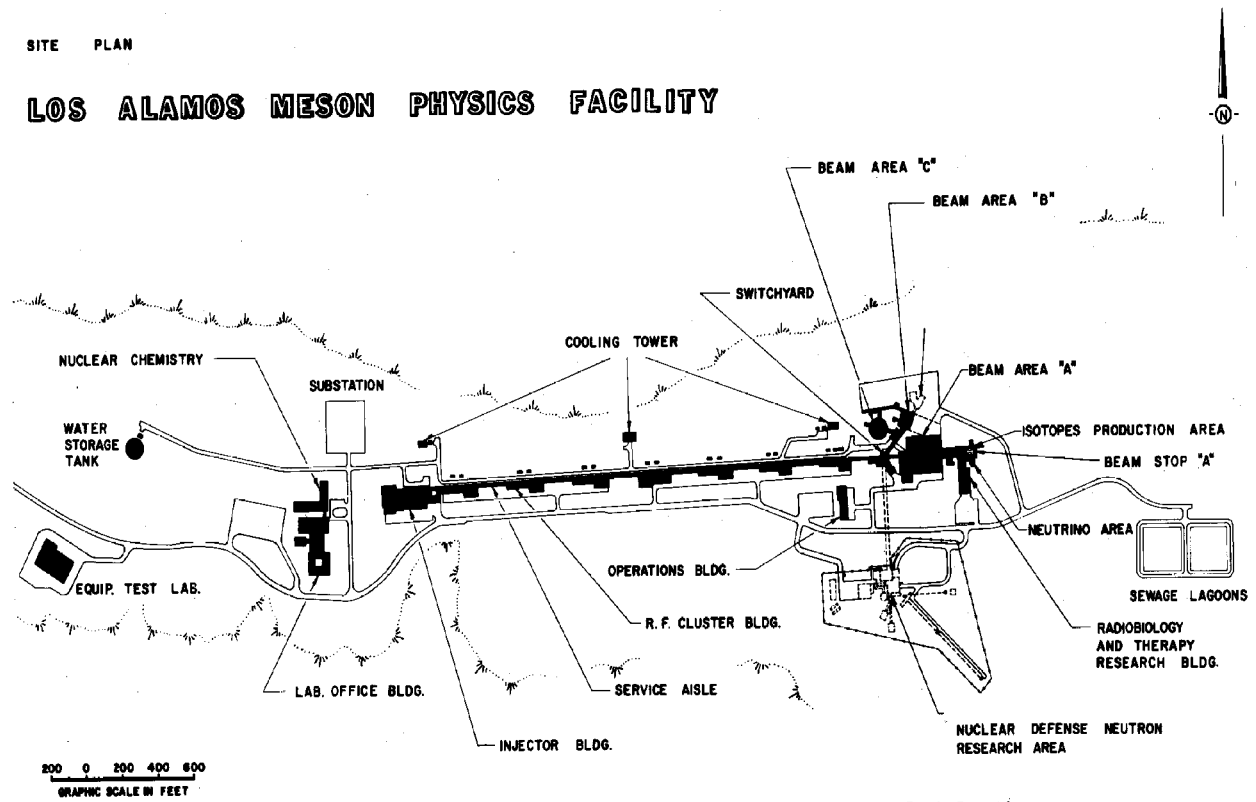


Figure 14.18 Los Alamos Meson Facility (LAMPF) Accelerator. (Courtesy, O. B. van Dyck, Los Alamos National Laboratory.)

Radio-frequency Linear Accelerators

TABLE 14.3 Parameters of the UNILAC^a

Accelerator length	125 m
Particle species	Variety of heavy ions, oxygen through uranium
Number of isotopes available	~ 50
Output energy (U) ^b	~ 4 GeV
Energy/nucleon (U)	17 MeV
Average output current (U)	0.05 μ A
Macropulselength	5 ms
Duty cycle factor	0.25, 5 ms each 20 ms
Ion source	Penning discharge
Typical charge state (U)	+10
Typical Z/A (U)	0.042
Electrostatic accelerator voltage	300 kV
Species selection	Magnetic mass separator
Wideröe accelerator, number of cavities	4
Matched entrance β	0.05
Bore diameter	0.03 m
Number of accelerating gaps	120
Total accelerating voltage	30 MV
rf frequency	27 MHz
rf power	3 MW
Energy/nucleon at exit (U)	1.4 MeV
Average charge state after stripper	+40
Alvarez accelerator, number of cavities	4
Total accelerating voltage	100 MeV
rf frequency	108 MHz = 4×27 MHz
rf power	5 MW
Number of cavities and rf amplifiers, independently phased array for beam energy variation	17
Accuracy of final beam energy	0.1%
Micropulselength	0.2 to 4 ns

^aGesellschaft für Schwerionenforschung.

^bParameters quoted for uranium ions.

Radio-frequency Linear Accelerators

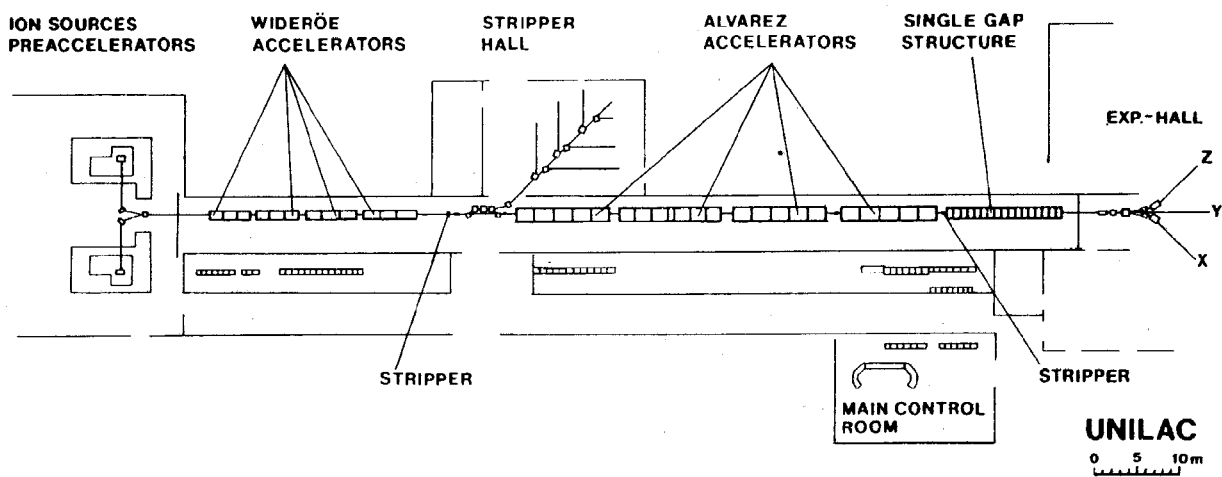


Figure 14.19 UNILAC heavy-ion linear accelerator. (Courtesy D. Böhne, Gesellschaft für Schwerionenforschung).

Radio-frequency Linear Accelerators

cavities is inadequate to determine the resonant frequencies of the disk-and-washer structure. The development of strongly-coupled cavity geometries results largely from the application of digital computers to determine normal modes.

In contrast to electron accelerators, ion linear accelerators may be composed of a variety of acceleration structures. Many factors must be considered in choosing the accelerating components, such as average gradient, field stability, shunt impedance, fabrication costs, and beam throughput. Energy efficiency has become a prime concern; this reflects the rising cost of electricity as well as an expansion of interest in the accelerator community from high-energy physics to commercial applications. Figure 14.17 shows an accelerator designed for medical irradiation. Three types of linear accelerators are used. Notice that the factor of 4 increase in frequency between the low- and high-energy sections. Higher frequency gives higher average gradient. The beam micro-bunches are compressed during acceleration in the drift-tube linac (see Section 13.4) and are matched into every fourth bucket of the coupled cavity linac.

Parameters of the Los Alamos Meson Facility (LAMF) accelerator are listed in Table 14.2. The machine, illustrated in Figure 14.18, was designed to accelerate high-current proton beams for meson production. Parameters of the UNILAC are listed in Table 14.3. The UNILAC, illustrated in Figure 14.19, accelerates a wide variety of highly ionized heavy ions for nuclear physics studies.

14.4 TRANSIT-TIME FACTOR, GAP COEFFICIENT, AND RADIAL DEFOCUSING

The diameter of accelerator drift tubes and the width of acceleration gaps cannot be chosen arbitrarily. The dimensions are constrained by the properties of electromagnetic oscillations. In this section, we shall study three examples of rf field properties that influence the design of linear accelerators: the transit-time factor, the gap coefficient, and the radial defocusing forces of traveling waves.

The *transit-time factor* applies mainly to drift tube accelerators with narrow acceleration gaps. The transit-time factor is important when the time for particles to cross the gap is comparable to or longer than the half-period of an electromagnetic oscillation. If d is the gap width, this condition can be written

$$d/v_s \geq \pi/\omega. \quad (14.51)$$

where v_s is the synchronous velocity. In this limit, particles do not gain energy $eE_0 d \sin\omega t$. Instead, they are accelerated by a time-averaged electric field smaller than $E_0 \sin\omega t$.

Assume that the gap electric field has time variation

$$E_z(r,z,t) = E_0 \cos(\omega t + \phi). \quad (14.52)$$

Radio-frequency Linear Accelerators

The longitudinal equation of motion for a particle crossing the gap is

$$dp_z/dt = qE_o \sin(\omega t + \phi). \quad (14.53)$$

Two assumptions simplify the solution of Eq. (14.53).

1. The time $t = 0$ corresponds to the time that the particle is at the middle of the gap.
2. The change in particle velocity over the gap is small compared to v_s .

The quantity ϕ is equivalent to the particle phase in the limit of a gap of zero thickness (see Fig. 13.1). The change in longitudinal motion is approximately

$$\Delta p_z \cong qE_o \int_{-d/2v_s}^{d/2v_s} \cos(\omega t + \phi) dt = qE_o \int_{-d/2v_s}^{d/2v_s} (\cos \omega t \sin \phi - \sin \omega t \cos \phi) dt. \quad (14.54)$$

Note that the term involving $\sin \omega t$ is an odd function; its integral is zero. The total change in momentum is

$$\Delta p_z \cong (2qE_o/\omega) \sin(d/2v_s) \sin \phi. \quad (14.55)$$

The momentum gain of a particle in the limit $d \Rightarrow 0$ is

$$\Delta p_o = qE_o \sin \phi (d/v_s). \quad (14.56)$$

The ratio of the momentum gain for a particle in a gap with nonzero width to the ideal thin gap is defined as the transit-time factor:

$$T_f = \Delta p / \Delta p_o = \sin(\omega d/2v_s) / (\omega d/2v_s). \quad (14.57)$$

The transit-time factor is also approximately equal to the ratio of energy gain in a finite-width gap to that in a zero-width gap.

Defining a particle transit time as $\Delta t = d/v_s$, Eq. (14.57) can be rewritten

$$T_f = \sin(\omega \Delta t/2) / (\omega \Delta t/2). \quad (14.58)$$

The transit-time factor is plotted in Figure 14.20 as a function of $\omega \Delta t$.

As an application example, consider acceleration of 5 MeV Cs^+ ions in a Wideröe accelerator operating at $f = 2$ MHz. The synchronous velocity is 2.6×10^6 m/s. The transit time across a 2-cm gap is $\Delta t = 7.5$ ns. The quantity $\omega \Delta t$ equals 0.95; the transit-time factor is 0.963. If the

Radio-frequency Linear Accelerators

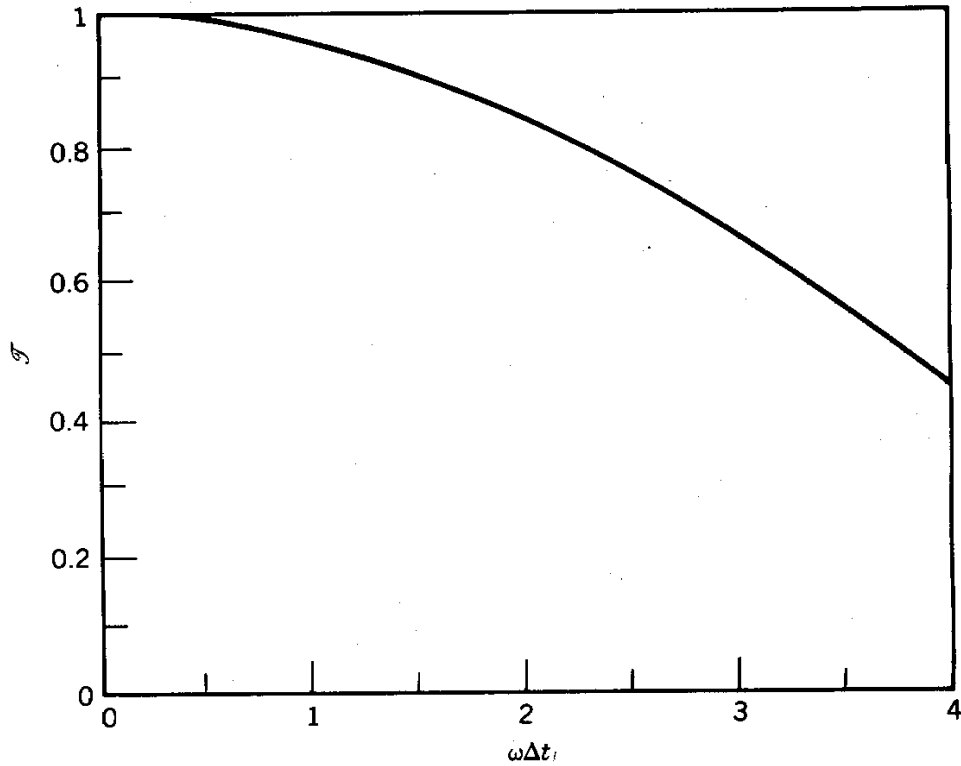


Figure 14.20 Transit-time factor as function of $\omega \Delta t$.

synchronous phase is 60° and the peak gap voltage is 100 kV, the cesium ions gain an average energy of $(100)(0.963)(\sin 60^\circ) = 83$ keV per gap.

The *gap coefficient* characterizes the radial variation of accelerating fields across the dimension of the beam. Variations in E_z lead to a spread in beam energy; particles with large-amplitude transverse oscillations gain a different energy than particles on the axis. Large longitudinal velocity spread is undesirable for research applications and may jeopardize longitudinal confinement in rf buckets. We shall first perform a non-relativistic derivation because the gap coefficient is primarily of interest in linear ion accelerators.

The slow-wave component of electric field chiefly responsible for particle acceleration has the form

$$E_z(0, z, t) = E_o \sin(\omega t - \omega z/v_s). \quad (14.59)$$

As discussed in Section 13.3, a slow wave appears to be an electrostatic field with no magnetic field when observed in a frame moving at velocity v_s . The magnitude of the axial electric field is unchanged by the transformation. The on-axis electric field in the beam rest frame is

$$E_z(0, z') = -E_o \sin(2\pi z'/\lambda'), \quad (14.60)$$

Radio-frequency Linear Accelerators

where λ' is the wavelength in the rest frame. In the nonrelativistic limit, $\lambda = \lambda'$ so that

$$\lambda' = 2\pi v_s / \omega. \quad (14.61)$$

The origin and sign convention in Eq. (14.60) are chosen so that a positive particle at $z' = 0$ has zero phase. In the limit that the beam diameter is small compared to λ' , the electrostatic field can be described by the paraxial approximation. According to Eq. (6.5), the radial electric field is

$$E_r(r', z') \cong (r'/2) (2\pi/\lambda') E_o \cos(2\pi z'/\lambda'). \quad (14.62)$$

The equation $\nabla \times \mathbf{E} = 0$ implies that

$$E_r(r', z') \cong -E_o [1 - (\pi r'/\lambda')^2 \sin(2\pi z'/\lambda')] \quad (14.63)$$

The energy gain of a particle at the outer radius of the beam (r_b) is reduced by a factor proportional to the square of the gap coefficient:

$$\Delta T/T \cong - (\pi r_b/\lambda')^2. \quad (14.64)$$

The gap coefficient must be small compared to unity for a small energy spread. Equation (14.64) sets a limit on the minimum wavelength of electromagnetic waves in terms of the beam radius and allowed energy spread:

$$\lambda > \pi r_b / \sqrt{\Delta T/T}. \quad (14.65)$$

As an example, consider acceleration of a 10-MeV deuteron beam of radius 0.01m. To obtain an energy spread less than 1%, the wavelength of the slow wave must be greater than 0.31 m. Using a synchronous velocity of 3×10^7 m/s, the rf frequency must be lower than $f < 100$ MHz.

This derivation can also be applied to demonstrate radial defocusing of ion beams by the fields of a slow wave. Equation (14.62) shows that slow waves must have radial electric fields. Note that the radial field is positive in the range of phase $0^\circ < \phi < 90^\circ$ and negative in the range $90^\circ < \phi < 180^\circ$. Therefore, the rf fields radially defocus particles in regions of axial stability. The radial forces must be compensated in ion accelerators by transverse focusing elements, usually magnetic quadrupole lenses. The stability properties of a slow wave are graphically illustrated in Figure 14.21. The figure shows three-dimensional variations of the electrostatic confinement potential (see Section 13.3) of an accelerating wave viewed in the wave rest frame. It is clear that there is no position in which particles have stability in both the radial and axial directions.

Radio-frequency Linear Accelerators

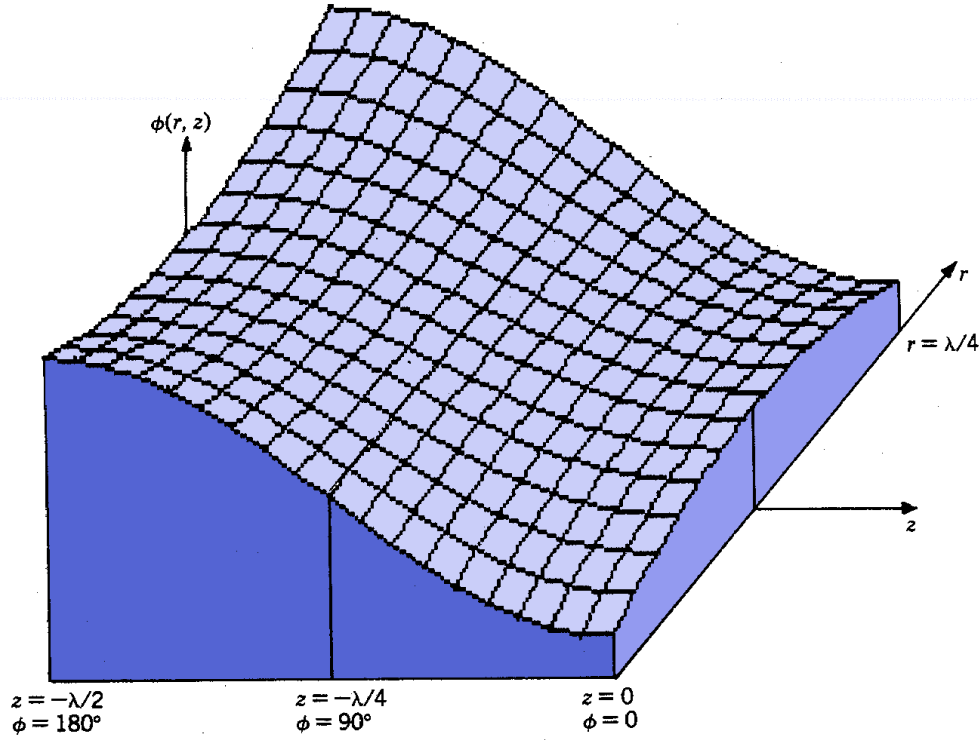


Figure 14.21 Three-dimensional view of variations of the electrostatic potential of a slow wave viewed in the wave rest frame.

The problems of the gap coefficient and radial defocusing are reduced greatly for relativistic particles. For a relativistic derivation, we must include the fact that the measured wavelength of the slow wave is not the same in the stationary frame and the beam rest frame. Equation (2.23) implies that the measurements are related by

$$\lambda = \lambda'/\gamma, \quad (14.66)$$

where γ is the relativistic factor, $\gamma = 1/\sqrt{1 - (v_s/c)^2}$. Again, primed symbols denote the synchronous particle rest frame.

The radial and axial fields in the wave rest frame can be expressed in terms of the stationary frame wavelength:

$$E_r'(r', z') \cong E_o' (-r'/2) (2\pi/\gamma\lambda) \cos(2\pi z'/\gamma\lambda), \quad (14.67)$$

$$E_z'(r', z') \cong E_o' [1 - (\pi r'/\gamma\lambda)^2] \sin(2\pi z'/\gamma\lambda). \quad (14.68)$$

Note that the peak value of axial field is unchanged in a relativistic transformation ($E_o' = E_o$). Transforming Eq. (14.68) to the stationary frame, we find that

Radio-frequency Linear Accelerators

$$E_z(r,z) = E_o [1 - (\pi r/\gamma\lambda)^2] \sin(2\pi z/\lambda), \quad (14.69)$$

with the replacement $r = r'$, $z = z'/\gamma$. Equation (14.69) differs from Eq. 14.63 by the γ factor in the denominator of the gap coefficient. The radial variation of the axial accelerating field is considerably reduced at relativistic energies.

The transformation of radial electric fields to the accelerator frame is more complicated. A pure radial electric field in the rest frame corresponds to both a radial electric field and a toroidal magnetic field in the stationary frame:

$$E_r' = \gamma (E_r + v_z B_\theta). \quad (14.70)$$

Furthermore, the total radial force exerted by the rf fields on a particle is written in the stationary frame as

$$F_r = q (E_r + v_z B_\theta). \quad (14.71)$$

The net radial defocusing force in the stationary frame is

$$F_r = [E_o (r/2) (2\pi/\lambda) \cos(2\pi z/\lambda)]/\gamma^2. \quad (14.72)$$

Comparison with Eq. (14.62) shows that the defocusing force is reduced by a factor of γ^2 . Radial defocusing by rf fields is negligible in high-energy electron linear accelerators.

14.5 VACUUM BREAKDOWN IN RF ACCELERATORS

Strong electric fields greater than 10 MV/m can be sustained in rf accelerators. This results partly from the fact that there are no exposed insulators in regions of high electric field. In addition, rf accelerators are run at high duty cycle, and it is possible to condition electrodes to remove surface whiskers. The accelerators are operated for long periods of time at high vacuum, minimizing problems of surface contamination on electrodes.

Nonetheless, there are limits to the voltage gradient set by resonant particle motion in the oscillating fields. The process is illustrated for electrons in an acceleration gap in Figure 14.22. An electron emitted from a surface during the accelerating half-cycle of the rf field can be accelerated to an opposing electrode. The electron produces secondary electrons at the surface. If the transit time of the initial electron is about one-half that of the rf period, the electric field will be in a

Radio-frequency Linear Accelerators

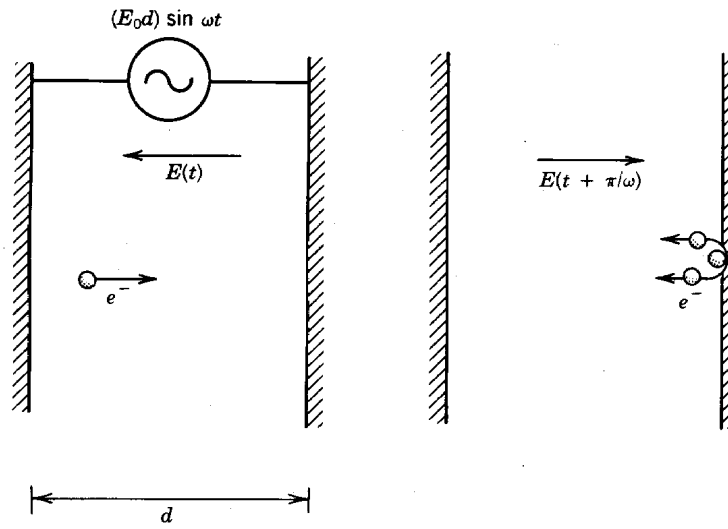


Figure 14.22 Geometry for calculating electron multipactoring. Electron field indicated at times of electron emission and electron collision with opposing electrode.

direction to accelerate the secondary electrons back to the first surface. If the secondary electron coefficient δ is greater than unity, the electron current grows. Table 14.4 shows maximum secondary electron coefficients for a variety of electrode materials. Also included are the incident electron energy corresponding to peak emission and to $\delta = 1$. Emission falls off at a higher electron energy. Table 14.4 gives values for clean, outgassed surfaces. Surfaces without special cleaning may have a value of δ as high as 4.

The resonant growth of electron current is called multipactoring, implying multiple electron impacts. Multipactoring can lead to a number of undesirable effects. The growing electron current absorbs rf energy and may clamp the magnitude of electric fields at the multipactoring level. Considerable energy can be deposited in localized regions of the electrodes, resulting in outgassing or evaporation of material. This often leads to a general cavity breakdown.

TABLE 14.4 Secondary Electron Coefficient

Metal	d (electrons per incident electron)	Electron Energy at δ_{\max} (eV)	Electron Energy for $\delta = 1$ (eV)
Al	1.9	220	35
Au	1.1	330	160
Cu	1.3	240	100
Fe	1.3	350	120
Mo	1.3	360	120
Ni	1.3	460	160
W	1.45	700	200

Radio-frequency Linear Accelerators

Conditions for electron multipactoring can be derived easily for the case of a planar gap with electrode spacing d . The electric field inside the gap is assumed spatially uniform with time variation given by

$$E(x,t) = -E_o \sin(\omega t + \phi). \quad (14.73)$$

The non-relativistic equation of motion for electrons is

$$m_e (d^2x/dt^2) = eE_o \sin(\omega t + \phi). \quad (14.74)$$

The quantity ϕ represents the phase of the rf field at the time an electron is produced on an electrode. Equation (14.74) can be integrated directly. Applying the boundary conditions that $x = 0$ and $dx/dt = 0$ at $t = 0$, we find that

$$x = - (eE_o/m_e \omega^2) [\omega t \cos \phi + \sin \phi - \sin(\omega t + \phi)]. \quad (14.75)$$

Resonant acceleration occurs when electrons move a distance d in a time interval equal to an odd number of rf half-periods. When this condition holds, electrons emerging from the impacted electrode are accelerated in the $-x$ direction; they follow the same equation of motion as the initial electrons. The resonance condition is

$$\Delta t = (2n+1) (\pi/\omega). \quad (14.76)$$

for $n = 0, 1, 2, 3, \dots$. Combining Eqs. (14.75) and (14.76), the resonant condition can be rewritten

$$d = - (eE_o/m_e \omega^2) [(2n+1) \pi \cos \phi + 2 \sin \phi], \quad (14.77)$$

because $\sin(\omega \Delta t + \phi) = -\sin \phi$. Furthermore, we can use Eq. (14.75) to find the velocity of electrons arriving at an electrode:

$$v_x(x=d) = - (2eE_o/m_e \omega^2) \cos \phi. \quad (14.78)$$

The solution of Eq. (14.74) is physically realizable only for particles leaving the initial electrode within a certain range of ϕ . First, the electric field must be negative to extract electrons from the surface at $t = 0$, or $\sin \phi > 0$. A real solution exists only if electrons arrive at the opposite electrode with positive velocity, or $\cos \phi > 0$. These two conditions are met in the phase range

$$0 < \phi < \pi/2. \quad (14.79)$$

Radio-frequency Linear Accelerators

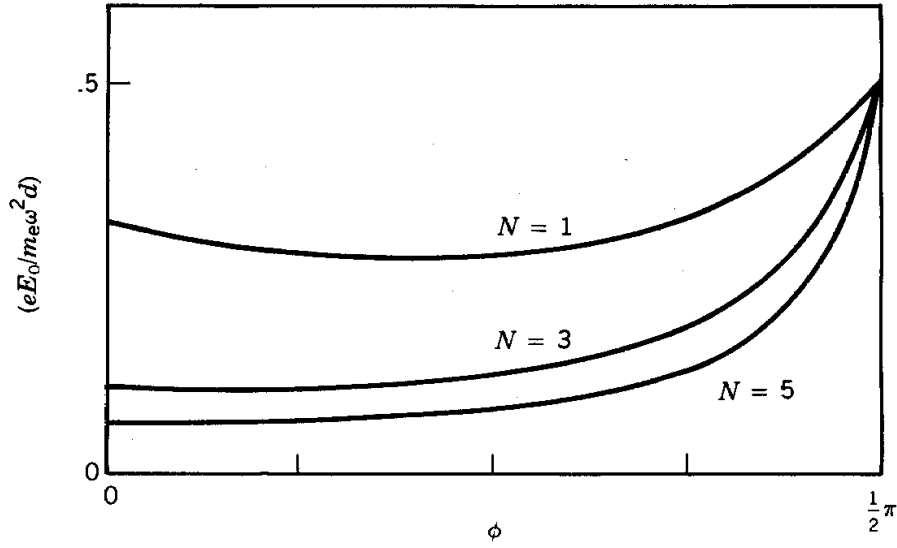


Figure 14.23 Conditions for electron multipactoring in planar gap of width d . Normalized resonant electric field, $eE_0/m_e\omega^2d$, versus rf phase at time of electron emission: E_0 , peak electric field; ω , rf angular frequency; N , number of rf half-periods during electron transit.

Figure 14.23 is a plot of Eq. (14.77) showing the breakdown parameter $(eE_0/m_e\omega^2d)$ versus the rf phase at which electrons leave the surface. Electron resonance is possible, in principle, over a range of gap voltage from 0 to $V = m_e\omega^2d^2/2e$.

Electron multipactoring is a significant problem in the low-energy sections of linear ion accelerators. Consider, for example, an acceleration gap for 2-MeV protons. Assume that the proton transit time Δt is such that $\omega\Delta t = 1$. This implies that $\omega d = \beta c$. Substituting the above condition in Eq. (14.78) and taking the $n = 0$ resonance condition, the electron energy at impact is $E_c = (2/\pi^2) (\beta \cos\phi)^2 (m_e c^2)$. The quantity β equals 0.065 for 2-MeV protons. The peak electron energy occurs when $\cos\phi = 1$ ($\phi = 0$); for the example it is 440 eV. Table 14.4 shows that this value is close to the energy of peak secondary electron emission. Electrons emitted at other phases arrive at the opposing electron with lower energy; therefore, they are not as likely to initiate a resonant breakdown. For this reason, the electron multipactoring condition is often quoted as

$$V_o = (d\omega)^2 m_e / \pi e = (2\pi d/\lambda)^2 (m_e c^2) / \pi e. \quad (14.80)$$

Equation (14.80) is expressed in terms of λ , the vacuum wavelength of the rf oscillations.

Electron multipactoring for the case quoted is probably not significant for values of n greater than zero because the peak electron energy is reduced by a factor of about $2n^2$. Therefore, breakdowns are usually not observed until the gap reaches a voltage level near that of Eq. (14.80). For an rf frequency $f = 400$ MHz, an acceleration gap 0.8 cm in width has $\omega\Delta t = 1$ for 2-MeV

Radio-frequency Linear Accelerators

protons. This corresponds to a peak voltage of 730 V. At higher field levels, the resonance condition can be met over longer pathlengths at higher field stresses. This corresponds to high-energy electrons, which generally have secondary emission coefficients less than unity. Therefore, with clean surfaces it is possible to proceed beyond multipactoring by raising the rf electric field level rapidly. This may not be the case with contaminated electrodes; surface effects contribute much of the mystery and aggravation associated with rf breakdown.

The ultimate limits for rf breakdown in clean acceleration gaps were investigated experimentally by Kilpatrick [W.D. Kilpatrick, "Criterion for Vacuum Sparking to Include Both RF and DC," University of California Radiation Laboratory, UCRL-2321, 1953]. The following formula is consistent with a wide variety of observations:

$$V_K = (2\pi d/\lambda)^2 (m_p c^2)/\pi e. \quad (14.81)$$

Note that Eq. (14.81) is identical to Eq. 14.80 with the replacement of the electron mass by that of the proton. The Kilpatrick voltage limit is about a factor of 2000 times the electron multipactoring condition. The similarity of the equations suggests proton multipactoring as a mechanism for high-voltage rf breakdown. The precise mechanisms of proton production on electrode surfaces are unknown. Proton production may be associated with thin surface coatings. Present research on extending rf systems past the Kilpatrick limit centers on the use of proton-free electrodes.

14.6 RADIO-FREQUENCY QUADRUPOLE

The rf quadrupole [I.M. Kapchinskii and V. A. Teplyakov, *Priboty i Teknika Eksperimenta* **2**, 19 (1970); R. H. Stokes, K. R. Crandall, J. E. Stovall, and D. A. Swenson, *IEEE Trans. Nucl. Sci.* **NS-26**, 3469 (1979)] is an ion accelerator in which both acceleration and transverse focusing are performed by rf fields. The derivations of Section 14.4 (showing lack of absolute stability in an rf accelerator) were specific to a cylindrical system; the fields in an RFQ are azimuthally asymmetric. There is no moving frame of reference in which RFQ fields can be represented as an electrostatic distribution. We shall see that the electric fields in the RFQ consist of positive and negative traveling waves; the positive wave continually accelerates ions in the range of stable phase. The beam is focused by oscillating transverse electric field components. These fields provide net beam focusing if the accelerating fields are not too high.

The major application of the RFQ is in low-energy ion acceleration. In the past, low-velocity ion acceleration presented one of the main technological difficulties for high-flux accelerators. A conventional ion beam injector consists of an ion source floating at high voltage and an electrostatic acceleration column. Space charge forces are strong for low-velocity ion beams; this

Radio-frequency Linear Accelerators

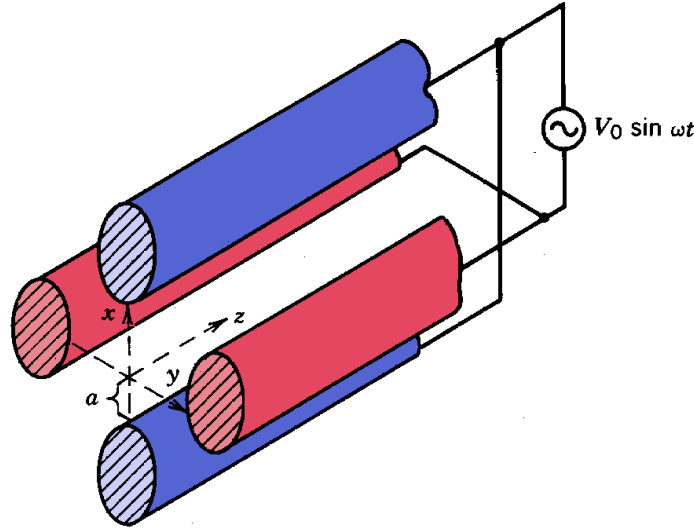


Figure 14.24 Radio-frequency electrostatic quadrupole for transverse confinement of charged particles.

fact motivates the choice of a high injection voltage, typically greater than 1 MV. The resulting system with adequate insulation occupies a large volume. The extracted beam must be bunched for injection into an rf accelerator. This implies long transport sections with magnetic quadrupole lenses. Magnetic lenses are ineffective for focusing low-energy ion beams, so that flux limits are low.

In contrast, the RFQ relies on strong electrostatic focusing in a narrow channel; this allows proton beam current in the range of 10 to 100 mA. An additional advantage of the RFQ is that it can combine the functions of acceleration and bunching. This is accomplished by varying the geometry of electrodes so that the relative magnitudes of transverse and longitudinal electric fields vary through the machine. A steady-state beam can be injected directly into the RFQ and reversibly bunched while it is being accelerated.

The quadrupole focusing channel treated in Chapter 8 has static fields with periodically alternating field polarity along the beam axis. In order to understand the RFQ, we will consider the geometry illustrated in Figure 14.24. The quadrupole electrodes are axially uniform but have time-varying voltage of the form $V_0 \sin \omega t$. It is valid to treat the fields near the axis in the electrostatic limit if $a \ll c/\omega$, where a is the distance between the electrodes and the axis. In this case, the electric fields are simply the expressions of Eqs. (4.22) and (4.23) multiplied by $\sin \omega t$:

$$E_x(x, y, z, t) = (E_0 x/a) \sin \omega t, \quad (14.82)$$

$$E_y(x, y, z, t) = - (E_0 y/a) \sin \omega t. \quad (14.83)$$

The oscillating electric fields near the axis are supported by excitation of surrounding microwave structures. Off-axis fields must be described by the full set of Maxwell equations.

Radio-frequency Linear Accelerators

The non-relativistic equation for particle motion in the x direction is

$$m (d^2x/dt^2) = (qE_0 x/a) \sin\omega t. \quad (14.84)$$

Equation (14.84) can be solved by the theory of the Mathieu equations. We will take a simpler approach to arrive at an approximate solution. Assume that the period for a transverse particle orbit oscillation is long compared to $2\pi/\omega$. In this limit, particle motion has two components; a slow betatron oscillation (parametrized by frequency Ω) and a rapid small-amplitude motion at frequency ω . We shall seek a solution by iteration using the trial solution

$$x(t) = x_0 \sin\Omega t + x_1 \sin\omega t. \quad (14.85)$$

where

$$x_1 \ll x_0, \quad (14.86)$$

$$\Omega \ll \omega, \quad (14.87)$$

$$\Omega^2 x_0 \ll \omega^2 x_1. \quad (14.88)$$

Substituting Eq. (14.85) into Eq. (14.84), we find that

$$-\Omega^2 x_0 \sin\Omega t - \omega^2 x_1 \sin\omega t = (qE_0/ma) \sin\omega t (x_0 \sin\Omega t + x_1 \sin\omega t). \quad (14.89)$$

The first term on the left-hand side and the second term on the right-hand side of Eq. (14.89) are dropped according to Eqs. (14.88) and (14.86). The result is an equation for the high-frequency motion:

$$-\omega^2 x_1 \cong [qE_0 x_0 \sin(\Omega t)/a]/m$$

or

$$x_1 \cong - [qE_0 x_0 \sin(\Omega t)/a]/m\omega^2. \quad (14.90)$$

The second step is to substitute Eq. (14.90) into Eq. (14.84) and average over a fast oscillation period to find the long-term motion. Terms containing $\sin\omega t$ average to zero. The remaining terms imply the following approximate equation for x_0 :

Radio-frequency Linear Accelerators

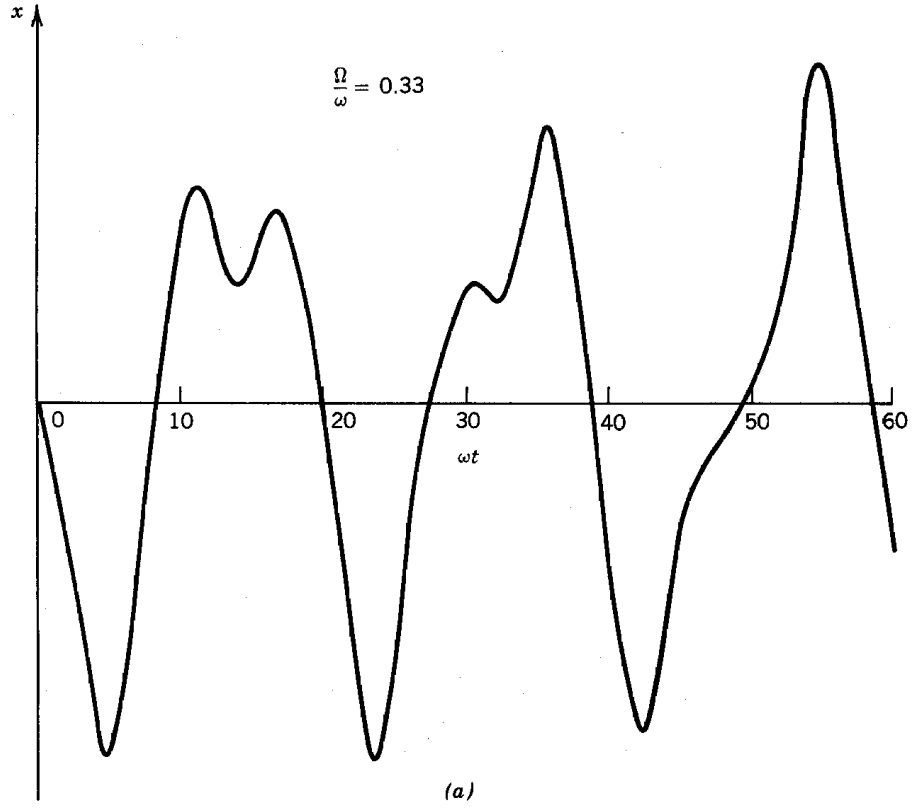


Figure 14.25 Numerical solutions for transverse motion of non-relativistic particle in oscillating electrostatic quadrupole field: $\Omega = (qE_0/m_0 a \omega)/\sqrt{2}$; E_0 , peak electric field at electrode tip; a , distance from axis to electrode tip; m_0 , particle rest mass; ω , rf angular frequency. (a) $\Omega/\omega = 0.33$. (b) $\Omega/\omega = 0.1$.

$$-\Omega^2 x_0 \sin \Omega t \cong - (qE_0/ma)^2 (x_0 \sin \Omega t) \overline{(\sin^2 \omega t)}/\omega^2, \quad (14.91)$$

where $\overline{\sin^2 \omega t}$ denotes the average over a time $2\pi/\omega$. Equation (14.91) implies that Ω has the real value

$$\Omega = (eE_0/ma\omega)/\sqrt{2}. \quad (14.92)$$

The long-term motion is oscillatory; the time-varying quadrupole fields provide net focusing. Numerical solutions to Eq. (14.84) are plotted in Figure 14.25 for $\omega=3\Omega$ and $\omega=10\Omega$. The phase relationship of Eq. (14.90) guarantees that particles are at a larger displacement when the fields are focusing. This is the origin of the average focusing effect. Orbit solutions in the y direction are similar.

Radio-frequency Linear Accelerators

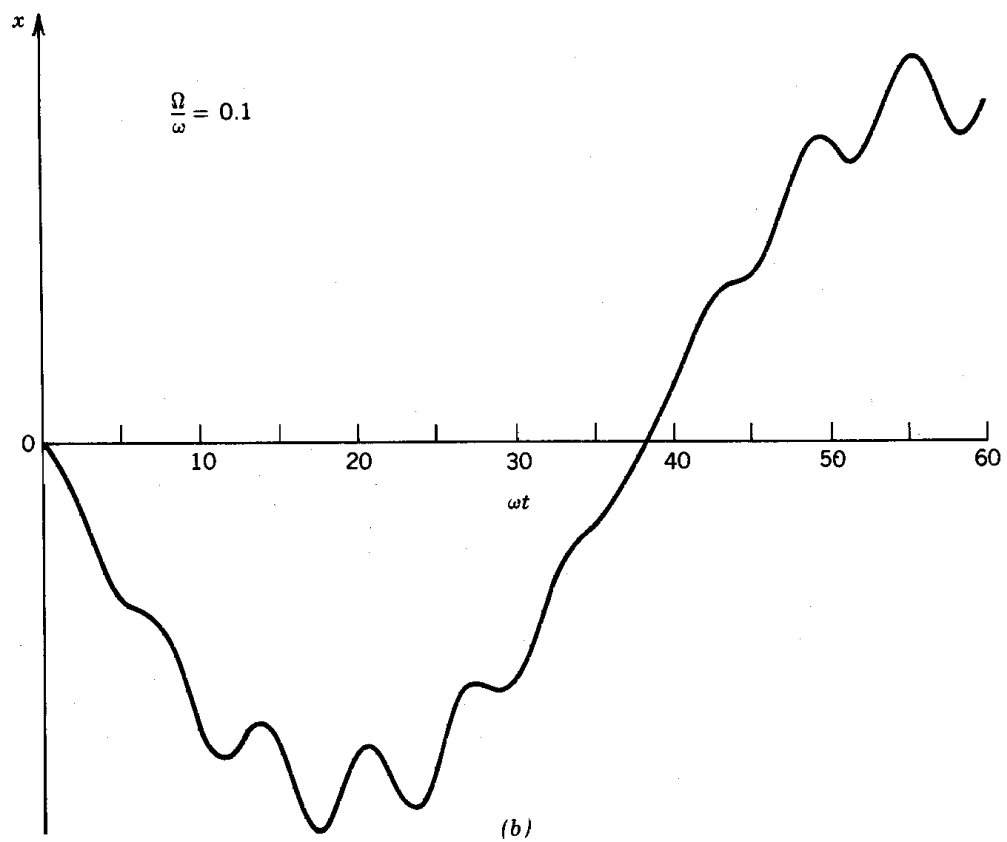


Figure 14.25 (Continued).

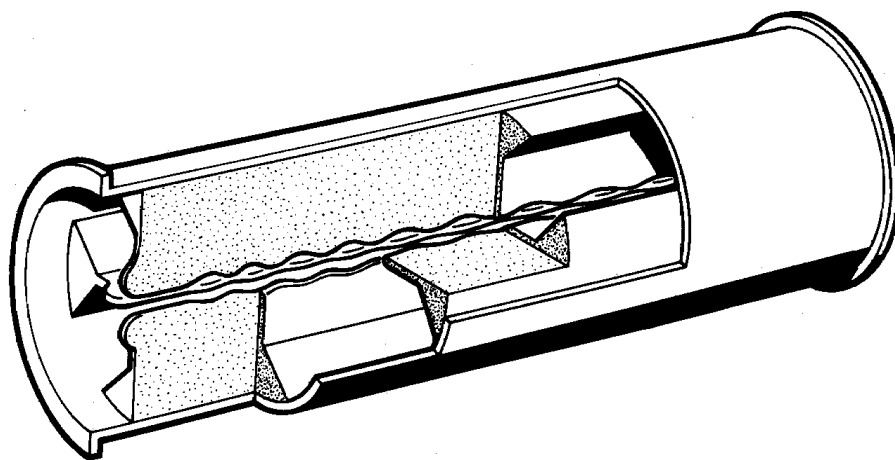


Figure 14.26 General configuration of rf quadrupole. (Courtesy, A. Wadlinger, Los Alamos National Laboratory).

Radio-frequency Linear Accelerators

The quadrupole lens of Figure 14.24 is useful only for focusing. It exerts no longitudinal force on ions. Axial field components are introduced if the shape of the electrodes is modified to that of Figure 14.26. The distance between the horizontal electrodes and the axis is modulated with spatial period D . There is a similar modulation of the vertical electrodes 90° out of phase. We postulate transverse fields of the form

$$E_x(x,y,z,t) = (E_o x/a) [1 + \varepsilon \sin(2\pi z/D)] \sin \omega t, \quad (14.93)$$

$$E_y(x,y,z,t) = - (E_o y/a) [1 - \varepsilon \sin(2\pi z/D)] \sin \omega t. \quad (14.94)$$

Again, the electrostatic approximation is invoked near the axis. Following the discussion of Section 4.4, Eqs. (14.93) and (14.94) are valid if (1) they are consistent with the Laplace equation and (2) the generating electrode surfaces lie on an equipotential. We shall show that both conditions can be satisfied.

Assume that a particle enters the system at the origin near time $t \leq \pi/2\omega$. The electric fields in the x - z plane are plotted in Figure 14.27a. The particle experiences a defocusing, quadrupolelike transverse field but also sees an accelerating component of field. Assume further than the particle moves a distance $D/4$ in the time interval $\pi/2\omega$. The particle position and field configuration are sketched at $t = 3\pi/2\omega$ in Figure 14.27c. Transverse fields are focusing, while the axial component of the electric field is still positive. A synchronous particle orbit can be defined for the system.

We can find the synchronous orbit by determining the axial electric fields and solving the longitudinal equation of motion. If the electrostatic potential field pattern satisfies the Laplace equation, then

$$\partial E_z / \partial z = - (\partial E_x / \partial x + \partial E_y / \partial y). \quad (14.95)$$

Substituting from Eqs. (14.93) and (14.94) and integrating, we find

$$E_z(x,y,z,t) = - (2\varepsilon E_o D/2\pi a) \cos(2\pi z/D) \sin \omega t. \quad (14.96)$$

The standing wave pattern of Eq. (14.96) can be resolved into two traveling waves,

$$E_z = (\varepsilon E_o D/2\pi a) [\sin(2\pi z/D + \omega t) - \sin(2\pi z/D - \omega t)]. \quad (14.97)$$

The negative-going wave in the first term can be neglected. The positive-going component will interact strongly with particles moving at the synchronous velocity,

$$v_s = D\omega/2\pi. \quad (14.98)$$

Assume that the synchronous particle enters the system at the origin of Figure 14.27 with velocity v_s at time $t = 0 + \phi/\omega$. Subsequently, the synchronous particle experiences a constant accelerating axial electric field of magnitude

Radio-frequency Linear Accelerators

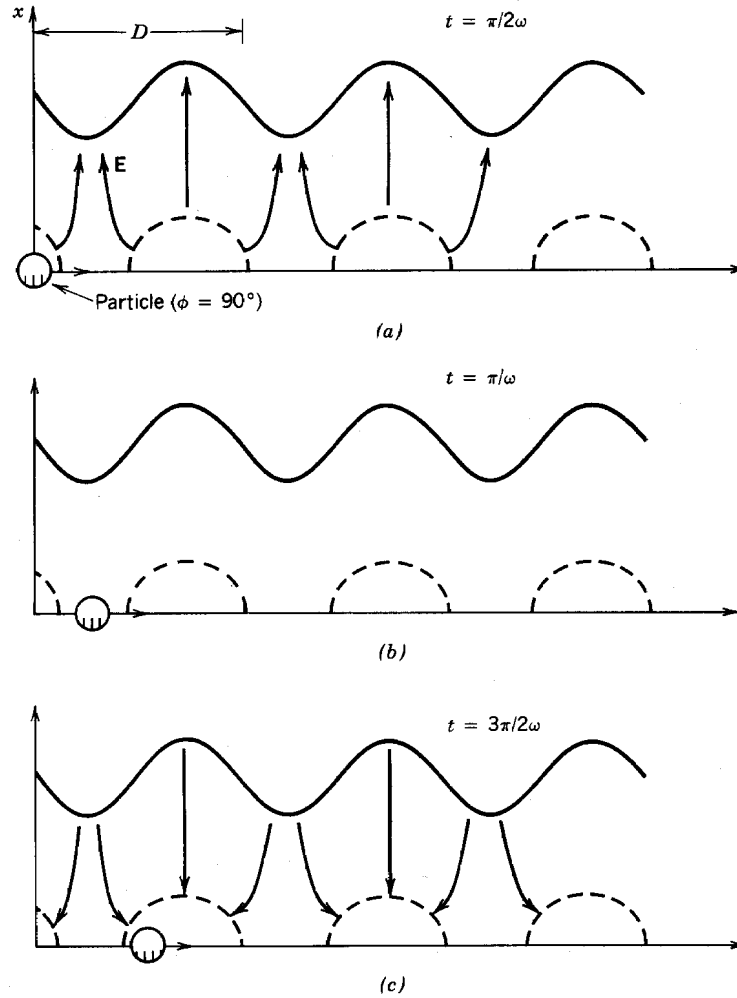


Figure 14.27 Particle motion and electric fields (projected in x - z plane) in beam transport region of rf quadrupole. Profile of vertical electrode (vane) designated as solid line; location of horizontal electrode extensions (toward axis) indicated by dashed lines. Particle position corresponds to synchronous particle injected with $\phi_s = 90^\circ$; time measured from zero crossing (positive slope) of vertical vane voltage. (a) $t = \pi/2\omega$, particle injected at $z = 0$. (b) $t = \pi\omega$. (c) $t = 3\pi/2\omega$.

$$E_{zs} = (\epsilon E_o D / 2\pi a) \sin\phi. \quad (14.99)$$

The choice of axial origin and rf field phase illustrated in Figure 14.27 makes ϕ synonymous with the particle phase defined in Figure 13.3. As we found in Section 13.1, particle bunches have longitudinal stability if the synchronous phase is in the range $0 < \phi < 90^\circ$. In contrast to a drift tube accelerator, an RFQ can be designed with only two traveling wave components. An alternate view is that the RFQ provides almost continuous acceleration. The equation of motion for the synchronous particle is

Radio-frequency Linear Accelerators

$$m (dv_s/dt) = (\epsilon q E_o D / 2\pi a) \sin\phi. \quad (14.100)$$

Substituting from Eq. (14.98), Eq. (14.100) can be rewritten as

$$dD/dz = (2\pi\epsilon q E_o \sin\phi / m\omega^2 a). \quad (14.101)$$

If the field modulation factor ϵ is constant, Eq. (14.101) indicates that the length of modulations should increase linearly moving from entrance to exit of the RFQ.

The transverse equation of motion for a particle passing $z = 0$ at time ϕ/ω is

$$\begin{aligned} d^2x/dt^2 &= (qE_o x/ma) [1 + \epsilon \sin(2\pi z/D)] \sin(\omega t + \phi) \\ &= (qE_o x/ma) \sin(\omega t + \phi) + (\epsilon q E_o x/2ma) [\cos(2\pi z/D - \omega t - \phi) - \cos(2\pi z/D + \omega t + \phi)]. \end{aligned} \quad (14.102)$$

Again, we retain only the part of the force resonant with synchronous particles. Applying the synchronous condition [Eq. (14.98)], Eq. (14.102) becomes

$$d^2x/dt^2 = (qE_o x/ma) \sin(\omega t + \phi) + (\epsilon q E_o x/2ma) \cos\phi. \quad (14.103)$$

The first term on the right-hand side represents the usual transverse focusing from the rf quadrupole. This component of motion is solved by the same method as the axially uniform oscillating quadrupole. The second term represents a defocusing force arising from the axial modulation of the quadrupole electrodes. The origin of this force can be understood by inspection of Figure 14.27. A sequence of particle position and electrode polarities is shown for a particle with a phase near 90° . On the average, the electrode spacing in the x direction is smaller during transverse defocusing and larger during the focusing phase for $\phi < 90^\circ$. This brings about a reduction of the average focusing force.

The solution for average betatron oscillations of particles is

$$x(t) = x_0 \cos\Omega t$$

where

$$\Omega = \sqrt{\frac{1}{2}(qE_o/ma\omega)^2 - (\epsilon q E_o/2ma) \cos\phi}$$

Radio-frequency Linear Accelerators

The same result is determined for motion in the y direction. There is net transverse focusing if Ω is a real number, or

$$\varepsilon \leq qE_o/(ma\omega^2 \cos\phi). \quad (14.105)$$

The longitudinal electric field is proportional to ε . Therefore, there are limits on the accelerating gradient that can be achieved while preserving transverse focusing:

$$E_z \leq (qE_o^2 D \tan\phi)/(2\pi a^2 m\omega^2). \quad (14.106)$$

Note that high longitudinal gradient is favored by high pole tip field (E_o) and a narrow beam channel (a).

The following parameters illustrate the results for the output portion of a 2.5-MeV RFQ operating at 440 MHz. The channel radius is $a = 0.0025$ m, the synchronous phase is $\phi = 60^\circ$, the cell length is 0.05 m, and the pole tip field is 10 MV/m, well below the Kilpatrick limit. The limiting longitudinal gradient is 4.4 MV/m. The corresponding modulation factor is $\varepsilon = 0.05$. A typical RFQ design accelerates protons to 2.5 MeV in a length less than 2 m.

Equations (14.93), (14.94), and (14.96) can be used to find the electrostatic potential function following the same method used in Section 4.4. The result is

$$\begin{aligned} \Phi(x,y,z) = & (E_o x^2/2a) [1 + \varepsilon \sin(2\pi z/D)] \\ & - (E_o y^2/2a) [1 - \varepsilon \sin(2\pi z/D)] + (\varepsilon E_o D^2/4\pi^2 a) \sin(2\pi z/D). \end{aligned} \quad (14.107)$$

The equipotential surfaces $\Phi = \pm E_o a/2$ determine the three-dimensional electrode shape. The equation for the minimum displacement of the vertical vanes from the axis is

$$x_{\min}^2 = [a^2 - (\varepsilon D^2/2\pi^2) \sin(2\pi z/D)]/[1 + \varepsilon \sin(2\pi z/D)].$$

This function is plotted in Figure 14.28. For a modulation factor $\varepsilon = 0.02$ and an average minimum electrode displacement of 0.0025 m, the distance from the electrode to the axis varies between 0.0019 and 0.0030 m.

The design of RFQ electrodes becomes more complex if the modulation factor is varied to add bunching capability. The design procedure couples results from particle orbit computer codes into a computer-controlled mill to generate complex electrodes such as that illustrated in Figure 14.29. The structure transports an incoming 30-mA, 30-keV proton beam. Electrode modulations increase gradually along the direction of propagation, adding longitudinal field components. The synchronous phase rises from 0 to the final value. Note the increasing modulation depth and cell

Radio-frequency Linear Accelerators

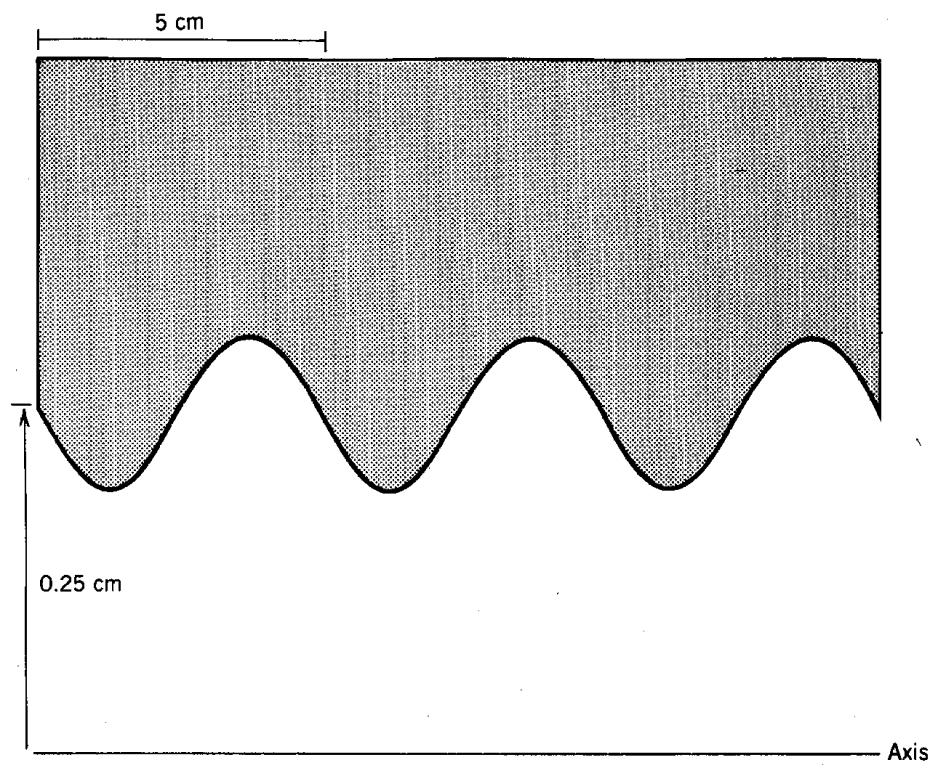


Figure 14.28 Profile of RFQ electrode. Parameters: $D = 0.05$ m, $a = 0.0025$ m, $\epsilon = 0.02$.

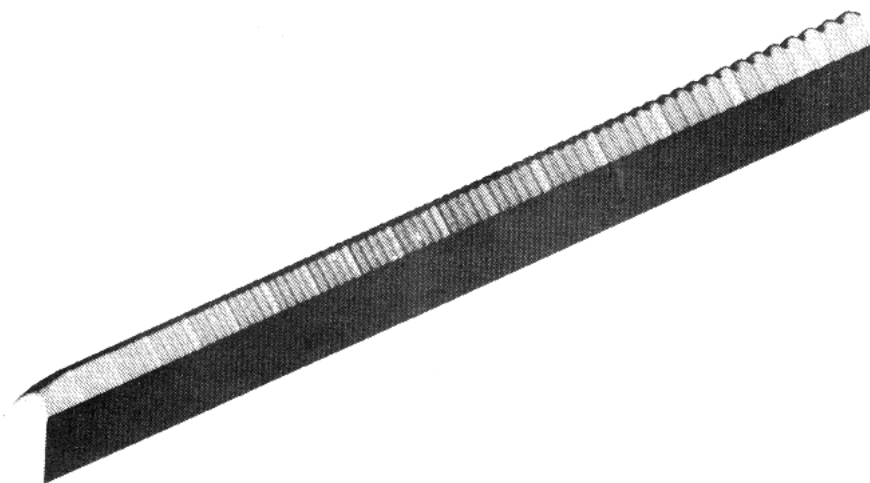


Figure 14.29 Computer-generated view of RFQ electrode designed for adiabatic bunching and acceleration of low-energy protons. Particles injected at left side. (Courtesy R. Jameson, Los Alamos National Laboratory.)

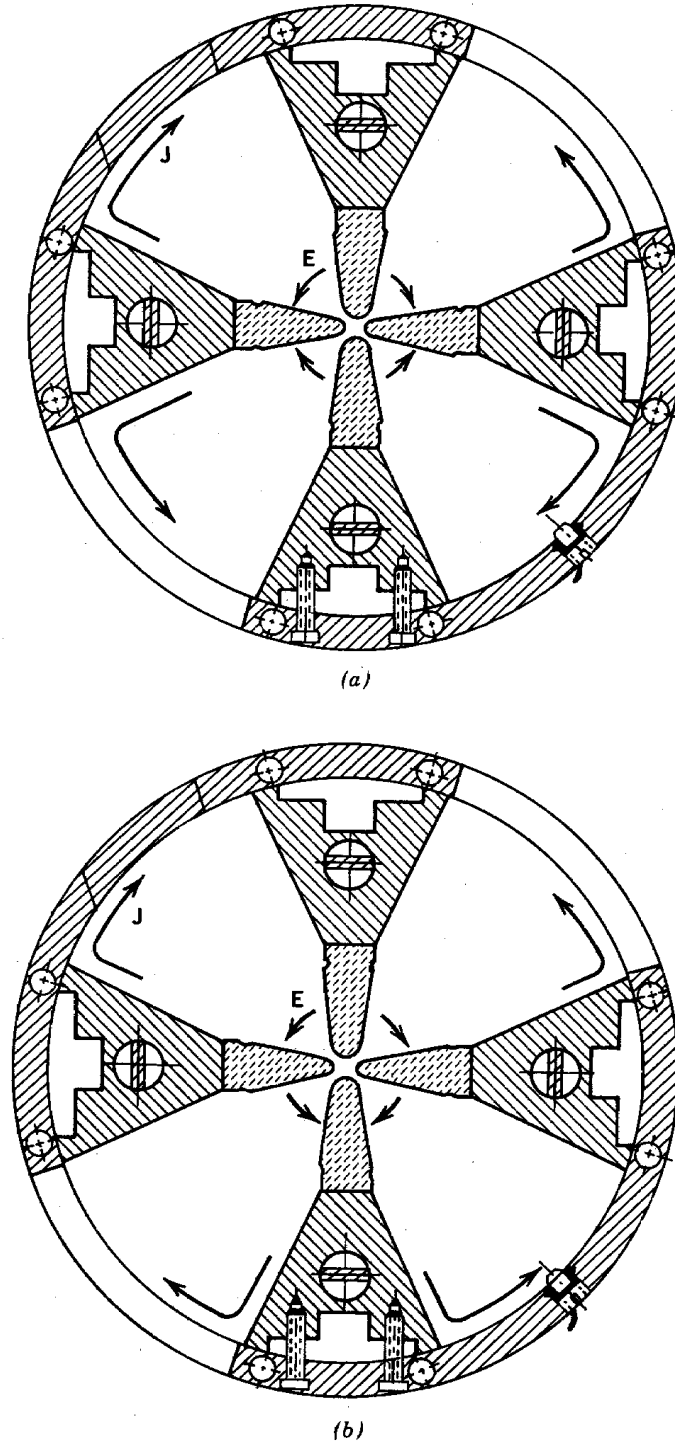


Figure 14.30 Diagram of rf modes in RFQ resonant structure; electric fields and wall currents outside beam transport region. (a) Quadrupole model (b) Dipole mode.

Radio-frequency Linear Accelerators

length along the direction of acceleration.

A cross section of a complete RFQ is illustrated in Figure 14.30. The volume outside the transport region is composed of four coupled cylindrical section cavities. The desired excitation modes for the cavities have axial magnetic fields and properties which are uniform along the longitudinal direction. Field polarities and current flows are illustrated for the quadrupole mode. A 440-MHz cavity has a radius of about 0.2 m. The mode for the quadrupole oscillation in all four cavities is designated TE_{210} . This terminology implies the following:

1. Electric fields are transverse to the z direction in the rf portion of the cavity.
2. Field quantities vary in azimuth according to $\cos(2\theta)$.
3. The electric field is maximum on axis and decreases monotonically toward the wall.
4. There is no axial variation of field magnitudes in the standing wave.

Coupling of the four lines through the narrow transport region is not strong; equal distribution of energy demands separate drives for each of the lines. The usual procedure is to surround the RFQ with an annular resonator (*manifold*) driven at a single feed point. The manifold symmetrizes the rf energy; it is connected to the transmission lines by multiple coupling slots.

Other modes of oscillation are possible in an RFQ cavity. The dipole mode illustrated in Figure 14.30b is particularly undesirable since it results in electrostatic deflections and beam loss. The dipole mode frequency does not differ greatly from that of the quadrupole. Another practical problem is setting end conditions on the electrodes to maintain a uniform electric field magnitude over the length. Problems of mode coupling and field uniformity multiply as the length of the RFQ increases. This is the main reason why RFQ applications are presently limited to low-energy acceleration. The RFQ has been studied as a pre-accelerator for heavy ions. In this case, the frequency is low. Low-frequency RFQs are sometimes fabricated as a nonresonant structure driven by an oscillator like the Wideröe accelerator.

14.7 RACETRACK MICROTRON

The extensive applications of synchrotron radiation to atomic and solid-state physics research has renewed interest in electron accelerators in the GeV range. The microtron is one of the most promising electron accelerators for research. Its outstanding feature is the ability to generate a continuous beam of high-energy electrons with average current approaching 100 μ A. The time-average output of a microtron is much higher than a synchrotron or high-electron linac, which produce pulses of electrons at relatively low repetition rates.

The racetrack microtron [V.Veksler, *Compt. Rend. Acad. Sci. U. S. S. R.* **43**, 444 (1944)] is illustrated in Figure 14.31a. Electrons are accelerated in a short linac section. Uniform field sector

Radio-frequency Linear Accelerators

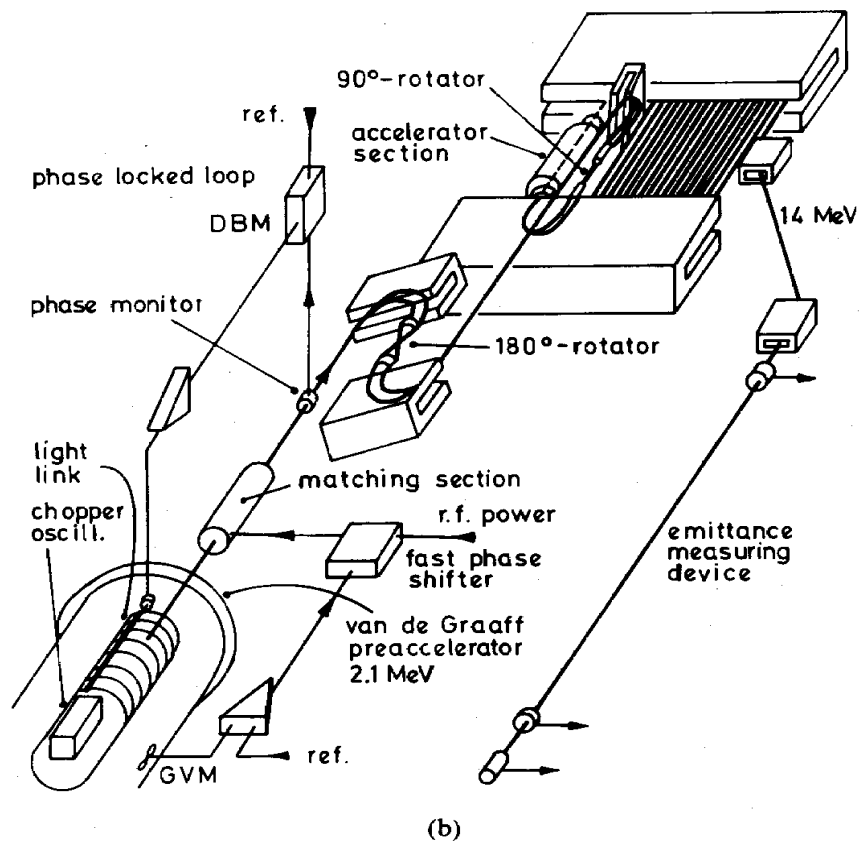
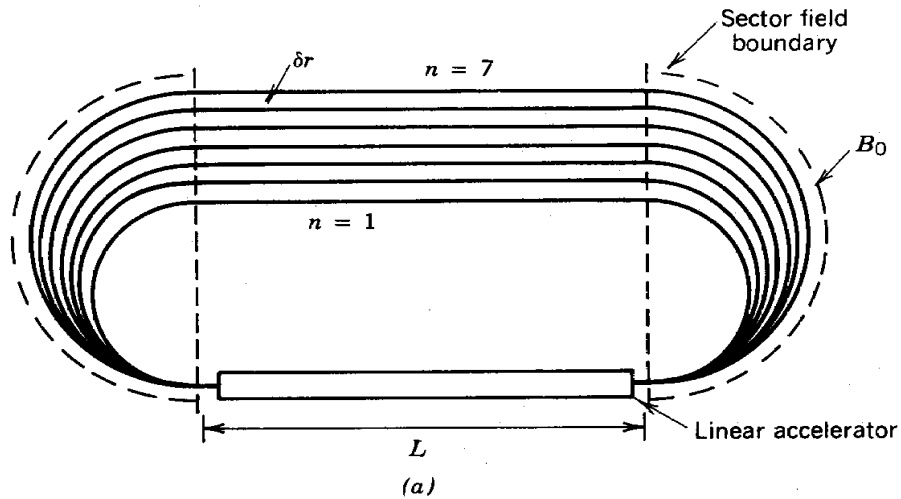


Figure 14.31 Racetrack microtron. (a) Section view of components and electron orbits after from one to seven passes through linear accelerator. (b) Isometric view of microtron components and injection system for MAMI I. (Courtesy H. Herminghaus, Universität Mainz.)

Radio-frequency Linear Accelerators

magnets at each end of the accelerator confine the electrons. Electrons at a variety of energy levels are contained simultaneously in the machine. Electron orbits in the magnets are half-circles. It is easily demonstrated that electrons return to the linear accelerator axis after each revolution, independent of their energy. The size of the orbit increases as the electron energy increases.

The microtron combines linear accelerator technology with circular accelerator particle dynamics. Beam recirculation allows more efficient utilization of the linac. In contrast to the high-energy electron linear accelerators of Section 14.1 (where the machine length is a major constraint), acceleration gradient is not the primary concern in the microtron. This means that the accelerator need not operate at high field stress; therefore, power dissipation is a factor of 25-100 times lower than a high-gradient electron linac. This accounts for the capability of CW steady-state operation. The phase velocity of traveling wave components in the microtron linac is equal to the speed of light. In contrast to high-energy electron linacs, microtrons have phase stability. The orbit size (and, hence, the time to return to the linac) depends on electron energy. Therefore, electrons can be longitudinally confined during acceleration, even at low values of accelerating gradient.

Some parameters of a medium-energy microtron are listed in Table 14.5. The machine is designed as a pre-accelerator in a three-microtron facility to produce an 840-MeV beam. The 14-MeV microtron with its associated injection and extraction system is illustrated in Figure 14.31b. The injected beam is generated by a 2-MV Van de Graaff accelerator. A beam chopper in the terminal of the electrostatic accelerator produces short pulses of electrons phased-matched to the linac. The complex series of lenses and deflection magnets matches the transverse and longitudinal distributions of the electron beam to the acceptance of the microtron. The origin of the parameters in Table 14.5 will be evident after we develop the theory of microtron equilibrium orbits.

In order to describe the microtron analytically, assume that the sector fields have sharp boundaries and a uniform field magnitude, B_0 . Electrons are injected with initial total energy U_0 and gain an energy ΔU in each pass through the linear accelerator. Assume, further, that $U_0 \gg m_e c^2$, so that the electron velocity is always approximately equal to the speed of light. We have shown that acceleration in linear accelerators arises from a traveling wave component of the form

$$E_z = E_0 \sin(\omega t - \omega z/c).$$

The energy gain of a relativistic electron traversing an accelerator of length L is

$$\Delta U = eE_0 L \sin\phi,$$

where ϕ is the phase of the particle with respect to the traveling wave. The energy gain for synchronous electrons passing through the linac is independent of their total energy.

The index n designates the number of times that an electron has passed through the linear accelerator; the orbits in Figure 14.31 are labeled accordingly. The time for an electron to traverse the microtron is

$$\Delta t_n = 2L/c + 2\pi r_{gn}/c, \quad (14.108)$$

Radio-frequency Linear Accelerators

TABLE 14.5 Parameters of MAMI, Stages I and II^a

	Stage I	Stage II
<i>General</i>		
Input energy	2.1 MeV	14 MeV
Output energy	14 MeV	175 MeV
Number of traversals	20	51
Power consumption (total)	280 kW	
Design current	100 μ A	
<i>Magnet System</i>		
Magnet separation	1.66 m	5.59 m
Magnetic field	0.10 T	0.54 T
Maximum orbit diameter	0.97 m	2.17 m
Magnet weight (each)	1.3 tonne	43 tonne
Gap width	6 cm	7 cm
<i>rf System</i>		
Linac length	0.80 m	3.55 m
Numbers of klystrons	2	
Frequency	2.449 GHz	
rf power	9 kW	64 kW
Beam load	1.2 kW	16 kW
Energy gain per turn	0.59 MeV	3.16 MeV

^aNuclear Physics Institute, University of Mainz.

where

$$r_{gn} = \gamma_n m_e c / e B_o = U_n / e B_o c.$$

The quantity U is the total energy of an electron on the n th orbit:

$$U_n = U_o + n\Delta U. \quad (14.109)$$

The condition for synchronous electrons is that they arrive at the entrance to the linac at the same phase of the rf period. In other words, the traversal time must be an integer multiple of the rf period. Letting ω be the frequency of rf oscillations in the linac, this condition is written

$$\Delta t_n = 2L/c + 2\pi U_n / e B_o c^2 = m(2\pi/\omega). \quad (14.110)$$

Radio-frequency Linear Accelerators

As electrons gain energy, the particle velocity is constant but the orbit size increases. The traversal time of high-energy particles is longer than that of low-energy particles. The difference in traversal times between particles on the n and $n-1$ orbits is

$$\Delta t_n - \Delta t_{n-1} = 2\pi\Delta U/eB_o c^2. \quad (14.111)$$

Clearly, for synchronization Δt_n must also equal an integer multiple of the rf period:

$$2\pi\Delta U/eB_o c^2 = q (2\pi/\omega). \quad (14.112)$$

As an example, we pick $q = 1$. This means that electrons take one extra rf period for a traversal with each energy increment. Following Table 14.5, assume a 20-turn microtron with an injection energy of 2 MeV. The bending magnetic field is 0.1 T, and the linear accelerator length is 0.8 M. The energy gain per turn is $\Delta U = 0.6$ MeV, implying an average acceleration gradient of 0.75 MV/m. Substituting into Eq. (14.112), the matched frequency is $\omega = 1.5 \times 10^{10} \text{ s}^{-1}$, or $f = 2.4$ GHz. Electrons injected at 2 MeV are boosted to 2.6 MeV in their first passage through the linac. The initial gyroradius in the bending field is 0.174 m; the total distance around the system on the first orbit is 2.7 m. Equation 14.111 implies that the time for the first traversal equals 22 rf periods. This is a high number; the particle must return to the linac entrance with equal phase after an interval of $22(2\pi/\omega)$. Synchronization requires excellent bending field uniformity and a constant energy input beam with little velocity dispersion. The problem becomes more acute as electrons are accelerated. Electrons on the highest-energy orbit take 42 rf periods to traverse the system. The synchronization problem limits the practical number of turns in a single microtron. A choice of $q > 1$ worsens the problem.

The separation between adjacent orbits on the side opposite the linac is

$$\delta r \cong 2\Delta r_g \cong \Delta U/eB_o c.$$

For the parameters of the example, $\delta r = 0.04$ in. The large orbit separation makes extraction of high-energy electrons relatively easy.

The two main problems of microtrons are beam steering and beam breakup instabilities. Regarding the first problem, the uniform magnetic field of the microtron has horizontal focusing but no vertical focusing. Lenses must be added to each beam line on the straight sections opposite the accelerator. Even with the best efforts to achieve bending field uniformity, it is necessary to add beam steering magnets with active beam sensing and compensation to meet the synchronization condition. The beam breakup instability is severe in the microtron because the current of all beams is concentrated in the high-Q resonant cavities of the linear accelerator. The beam breakup instability is the main reason why microtron average currents are limited to less than 1 mA. It has also impeded the development of microtrons with superconducting linear accelerator cavities. These cavities have extremely high values of Q for all modes.

Radio-frequency Linear Accelerators

Phase stability is an interesting feature of microtrons. In contrast to high-energy electron linear accelerators, variations of electron energy lead to phase shifts because of the change in orbit pathlength. For instance, a particle with energy greater than that of the synchronous particle has a larger gyroradius; therefore, it enters the linac with increased phase. For longitudinal stability, the higher-energy electrons must receive a reduced energy increment in the linac. This is true if the synchronous phase is in a region of decreasing field, $90^\circ \leq \phi_s \leq 180^\circ$. Particle phase orbits are the inverse of those in a linear ion accelerator.

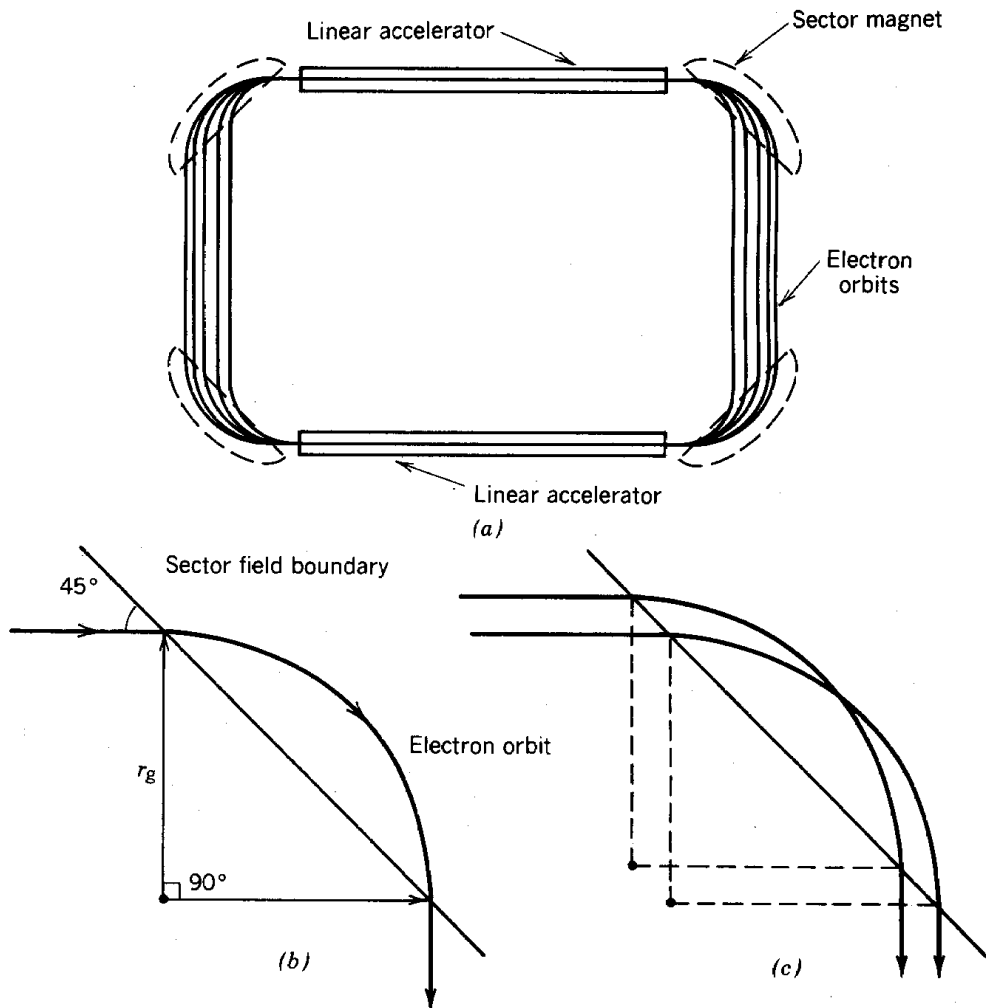


Figure 14.32 Double-sided microtron. (a) Sectional view of components and particle orbits. (b) Specular reflection of particle orbit incident on 45° sector magnet. (c) Neutral focusing property of 45° sector magnet.

Radio-frequency Linear Accelerators

The double-sided microtron (DSM) illustrated in Figure 14.32a is an alternative to the racetrack microtron. The DSM has linear accelerators in both straight sections. Beam deflection is performed by four 45° sector magnets. The major advantage, compared to the racetrack microtron, is that approximately double the electron energy can be achieved for the same magnet mass. The 45° sector magnet has the feature that the orbits of electrons of any energy are reflected at exactly 90° (see Fig. 14.32b).

Unfortunately, the DSM has unfavorable properties for electron focusing. Figure 14.32c shows a particle trajectory on the main orbit compared to an orbit displaced horizontally off-axis. Note that there is no focusing; the DSM has neutral stability in the horizontal direction. Furthermore, the sector magnets contribute defocusing forces in the vertical direction. There are edge-focusing effects because the magnets boundaries are inclined 45° to the particle orbits. Reference to Section 6.9, shows that the inclination gives a negative focal length resulting in defocusing.

15

Cyclotrons and Synchrotrons

The term *circular accelerator* refers to any machine in which beams describe a closed orbit. All circular accelerators have a vertical magnetic field to bend particle trajectories and one or more gaps coupled to inductively isolated cavities to accelerate particles. Beam orbits are often not true circles; for instance, large synchrotrons are composed of alternating straight and circular sections. The main characteristic of resonant circular accelerators is synchronization between oscillating acceleration fields and the revolution frequency of particles.

Particle recirculation is a major advantage of resonant circular accelerators over rf linacs. In a circular machine, particles pass through the same acceleration gap many times (10^2 to greater than 10^8). High kinetic energy can be achieved with relatively low gap voltage. One criterion to compare circular and linear accelerators for high-energy applications is the energy gain per length of the machine; the cost of many accelerator components is linearly proportional to the length of the beamline. Dividing the energy of a beam from a conventional synchrotron by the circumference of the machine gives effective gradients exceeding 50 MV/m. The gradient is considerably higher for accelerators with superconducting magnets. This figure of merit has not been approached in either conventional or collective linear accelerators.

There are numerous types of resonant circular accelerators, some with specific advantages and some of mainly historic significance. Before beginning a detailed study, it is useful to review briefly existing classes of accelerators. In the following outline, a standard terminology is defined and the significance of each device is emphasized.

Cyclotrons and Synchrotrons

Most resonant circular accelerators can be classed as either cyclotrons or synchrotrons. One exception is the microtron (Section 14.7), which is technologically akin to linear accelerators. The microtron may be classified as a cyclotron for relativistic electrons, operating well beyond the transition energy (see Section 15.6). The other exception is the synchrocyclotron (Section 15.4).

A. Cyclotron

A cyclotron has constant magnetic field magnitude and constant rf frequency. Beam energy is limited by relativistic effects, which destroy synchronization between particle orbits and rf fields. Therefore, the cyclotron is useful only for ion acceleration. The virtue of cyclotrons is that they generate a continuous train of beam micropulses. Cyclotrons are characterized by large-area magnetic fields to confine ions from zero energy to the output energy.

1. Uniform-Field Cyclotron

The uniform-field cyclotron has considerable historic significance. It was the first accelerator to generate multi-MeV particle beams for nuclear physics research. The vertical field is uniform in azimuth. The field magnitude is almost constant in the radial direction, with small positive field index for vertical focusing. Resonant acceleration in the uniform-field cyclotron depends on the constancy of the non-relativistic gyrofrequency. The energy limit for light ion beams is about 15-20 MeV, determined by relativistic mass increase and the decrease of magnetic field with radius. There is no synchronous phase in a uniform-field cyclotron.

2. Azimuthally-Varying-Field (AVF) Cyclotron

The AVF cyclotron is a major improvement over the uniform-field cyclotron. Variations are added to the confining magnetic field by attaching wedge-shaped inserts at periodic azimuthal positions of the magnet poles. The extra horizontal-field components enhance vertical focusing. It is possible to tolerate an average negative-field index so that the bending field increases with radius. With proper choice of focusing elements and field index variation, the magnetic field variation balances the relativistic mass increase, resulting in a constant-revolution frequency. An AVF cyclotron with this property is called an isochronous cyclotron. An additional advantage of AVF cyclotrons is that the stronger vertical focusing allows higher beam intensity. AVF machines have supplanted the uniform-field cyclotron, even in low-energy applications.

3. Separated-Sector Cyclotron

The separated-sector cyclotron is a special case of the AVF cyclotron. The azimuthal field variation results from splitting the bending magnet into a number of sectors. The advantages of the separated sector cyclotron are (1) modular magnet construction and (2) the ability to locate rf

Cyclotrons and Synchrotrons

feeds and acceleration gaps between the sectors. The design of separated-sector cyclotrons is complicated by the fact that particles cannot be accelerated from low energy. This feature can be used to advantage; beams with lower emittance (better coherence) are achieved if an independent accelerator is used for low-energy acceleration.

4. Spiral Cyclotron

The pole inserts in a spiral cyclotron have spiral boundaries. Spiral shaping is used in both standard AVF and separated-sector machines. In a spiral cyclotron, ion orbits have an inclination at the boundaries of high-field regions. Vertical confinement is enhanced by edge focusing (Section 6.9). The combined effects of edge focusing and defocusing lead to an additional vertical confinement force.

5. Superconducting Cyclotron

Superconducting cyclotrons have shaped iron magnet poles that utilize the focusing techniques outlined above. The magnetizing force is supplied by superconducting coils, which consume little power. Superconducting cyclotrons are typically compact machines because they are operated at high fields, well above the saturation level of the iron poles. In this situation, all the magnetic dipoles in the poles are aligned; the net fields can be predicted accurately.

B. Synchrocyclotron

The synchrocyclotron is a precursor of the synchrotron. It represents an early effort to extend the kinetic energy limits of cyclotrons. Synchrocyclotrons have a constant magnetic field with geometry similar to the uniform-field cyclotron. The main difference is that the rf frequency is varied to maintain particle synchronization into the relativistic regime. Synchrocyclotrons are cyclic machines with a greatly reduced time-averaged output flux compared to a cyclotron. Kinetic energies for protons to 1 GeV have been achieved. In the sub-GeV energy range, synchrocyclotrons were supplanted by AVF cyclotrons, which generate a continuous beam. Synchrocyclotrons have not been extended to higher energy because of technological and economic difficulties in fabricating the huge, monolithic magnets that characterize the machine.

C. Synchrotron

Synchrotrons are the present standard accelerators for particle physics research. They are cyclic machines. Both the magnitude of the magnetic field and the rf frequency are varied to maintain a synchronous particle at a constant orbit radius. The constant-radius feature is very important; bending and focusing fields need extend over only a small ring-shaped volume. This minimizes the

Cyclotrons and Synchrotrons

cost of the magnets, allowing construction of large-diameter machines for ion energies of up to 800 GeV. Synchrotrons are used to accelerate both ions and electrons, although electron machines are limited in energy by emission of synchrotron radiation. The main limits on achievable energy for ions are the cost of the machine and availability of real estate. Cycling times are long in the largest machines, typically many seconds. Electron synchrotrons and proton boosters cycle at frequencies in the range of 15 to 60 Hz.

1. Weak Focusing Synchrotron

Early synchrotrons used weak focusing. The bending magnets were shaped to produce a field with index in the range $0 < n < 1$. With low focusing force, the combined effects of transverse particle velocity and synchrotron oscillations (see Section 15.6) resulted in beams with large cross section. This implies costly, large-bore magnets.

2. Strong Focusing Synchrotron

All modern synchrotrons use transverse focusing systems composed of strong lenses in a focusing-defocusing array. Strong focusing minimizes the beam cross section, reducing the magnet size. Beam dynamics are more complex in a strong focusing synchrotron. The magnets must be constructed and aligned with high precision, and care must be taken to avoid resonance instabilities. Advances in magnet technology and beam theory have made it possible to overcome these difficulties.

Alternating Gradient Synchrotron (AGS). The bending field in an alternating gradient synchrotron is produced by a ring of wedge-shaped magnets which fit together to form an annular region of vertical field. The magnets have alternate positive and negative field gradient with $n \gg 1$. The combination of focusing and defocusing in the horizontal and vertical directions leads to net beam confinement.

Separated Function Synchrotron. Most modern synchrotrons are configured as separated function synchrotrons. The bending field is provided by sector magnets with uniform vertical field. Focusing is performed by quadrupole magnetic lens set between the bending magnets. Other magnets may be included for correction of beam optics.

3. Storage Ring

A storage ring usually has the same focusing and bending field configuration as a separated function synchrotron, but provides no acceleration. The magnetic fields are constant in time. An rf cavity may be included for longitudinal beam manipulations such as stacking or, in the case of

Cyclotrons and Synchrotrons

electrons, maintaining kinetic energy in the presence of radiation loss. A storage ring contains energetic particles at constant energy for long periods of time. The primary applications are for colliding beam experiments and synchrotron radiation production.

4. Collider

A collider is a synchrotron, storage ring, dual synchrotron, or dual storage ring with special geometry to allow high-energy charged particles moving in opposite directions to collide head-on at a number of positions in the machine. The use of colliding beams significantly increases the amount of energy available to probe the structure of matter for elementary particle physics. Colliders have been operated (or are planned) for counter-rotating beams of protons (pp collider), electrons and positrons (e^-e^+), and protons and antiprotons ($p\bar{p}$).

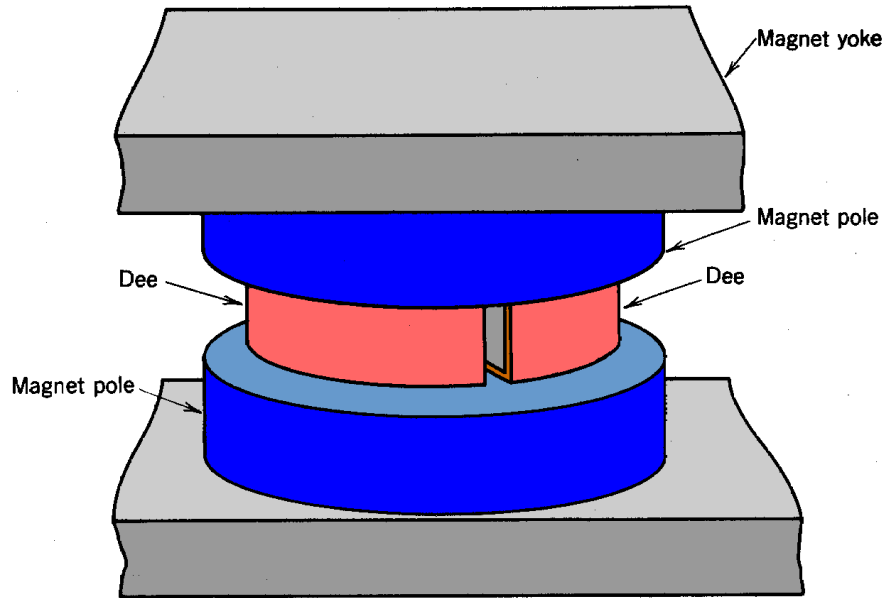
Section 15.1 introduces the uniform-field cyclotron and the principles of circular resonant accelerators. The longitudinal dynamics of the uniform-field cyclotron is reviewed in Section 15.2. The calculations deal with an interesting application of the phase equations when there is no synchronous particle. The model leads to the choice of optimum acceleration history and to limits on achievable kinetic energy. Sections 15.3 and 15.4 are concerned with AVF, or isochronous, cyclotrons. Transverse focusing is treated in the first section. Section 15.4 summarizes relationships between magnetic field and rf frequency to preserve synchronization in fixed-field, fixed-frequency machines. There is also a description of the synchrocyclotron.

Sections 15.5-15.7 are devoted to the synchrotron. The first section describes general features of synchrotrons, including focusing systems, energy limits, synchrotron radiation, and the kinematics of colliding beams. The longitudinal dynamics of synchrotrons is the subject of Section 15.6. Material includes constraints on magnetic field and rf frequency variation for synchronization, synchrotron oscillations, and the transition energy. To conclude, Section 15.7 summarizes the principles and benefits of strong focusing. Derivations are given to illustrate the effects of alignment errors in a strong focusing system. Forbidden numbers of betatron wavelengths and mode coupling are discussed qualitatively.

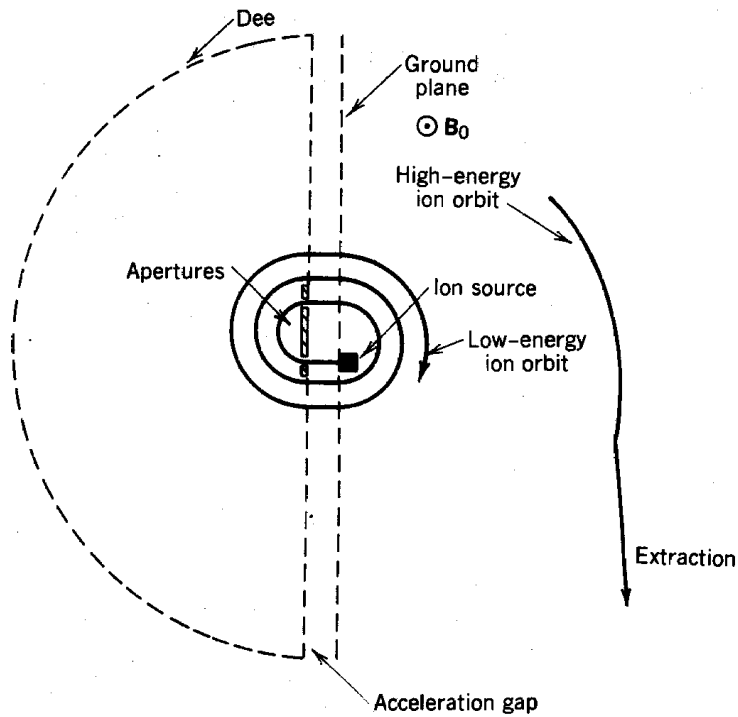
15.1 PRINCIPLES OF THE UNIFORM-FIELD CYCLOTRON

The operation of the uniform-field cyclotron [E. O. Lawrence, *Science* **72**, 376 (1930)] is based on the fact that the gyrofrequency for non-relativistic ions [Eq. (3.39)] is independent of kinetic energy. Resonance between the orbital motion and an accelerating electric field can be achieved for ion kinetic energy that is small compared to the rest energy. The configuration of the uniform-field cyclotron is illustrated in Figure 15.1a. Ions are constrained to circular orbits by a

Cyclotrons and Synchrotrons



(a)



(b)

Figure 15.1 Uniform-field cyclotron. (a) General layout of beam acceleration region. (b) Overhead sectional view of acceleration region, showing a cyclotron with one dee and a ground plane. A single dee facilitates injection and extraction.

Cyclotrons and Synchrotrons

vertical field between the poles of a magnet. The ions are accelerated in the gap between two D-shaped metal structures (dees) located within the field region. An ac voltage is applied to the dees by an rf resonator. The resonator is tuned to oscillate near ω_g .

The acceleration history of an ion is indicated in Figure 15.1b. The accelerator illustrated has only one dee excited by a bipolar waveform to facilitate extraction. A source, located at the center of the machine continuously generates ions. The low-energy ions are accelerated to the opposite electrode during the positive-polarity half of the rf cycle. After crossing the gap, the ions are shielded from electric fields so that they follow a circular orbit. When the ions return to the gap after a time interval π/ω_g they are again accelerated because the polarity of the dee voltage is reversed. An aperture located at the entrance to the acceleration gap limits ions to a small range of phase with respect to the rf field. If the ions were not limited to a small phase range, the output beam would have an unacceptably large energy spread. In subsequent gap crossings, the ion kinetic energy and gyroradius increase until the ions are extracted at the periphery of the magnet. The cyclotron is similar to the Wideröe linear accelerator (Section 14.2); the increase in the gyroradius with energy is analogous to the increase in drift-tube length for the linear machine.

The rf frequency in cyclotrons is relatively low. The ion gyrofrequency is

$$f_o = qB_o/2\pi m_i = (1.52 \times 10^7) B_o(\text{tesla})/A, \quad (15.1)$$

where A is the atomic mass number, m_i/m_p . Generally, frequency is in the range of 10 MHz for magnetic fields near 1 T. The maximum energy of ions in a cyclotron is limited by relativistic detuning and radial variations of the magnetic field magnitude. In a uniform-field magnet field, the kinetic energy and orbit radius of non-relativistic ions are related by

$$T_{\max} = 48 (Z * RB)^2/A, \quad (15.2)$$

where T_{\max} is given in MeV, R in meters, and B in tesla. For example, 30-MeV deuterons require a 1-T field with good uniformity over a 1.25-m radius.

Transverse focusing in the uniform-field cyclotron is performed by an azimuthally symmetric vertical field with a radial gradient (Section 7.3). The main differences from the betatron are that the field index is small compared to unity ($v_r \approx 1$ and $v_z \ll 1$) and that particle orbits extend over a wide range of radii. Figure 15.2 diagrams magnetic field in a typical uniform-field cyclotron magnet and indicates the radial variation of field magnitude and field index, n . The field index is not constant with radius. Symmetry requires that the field index be zero at the center of the magnet. It increases rapidly with radius at the edge of the pole. Cyclotron magnets are designed for small n over most of the field area to minimize desynchronization of particle orbits. Therefore, vertical focusing in a uniform-field cyclotron is weak.

There is no vertical magnetic focusing at the center of the magnet. By a fortunate coincidence,

Cyclotrons and Synchrotrons

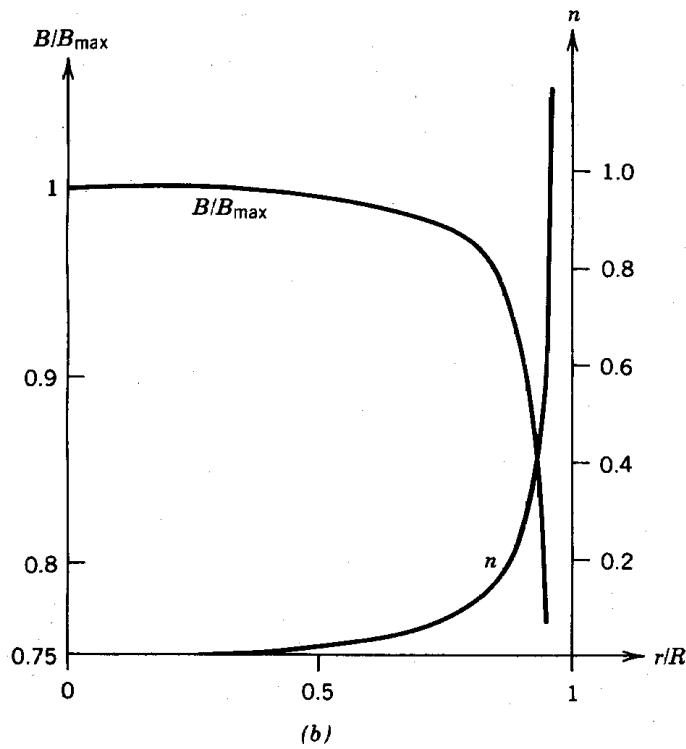
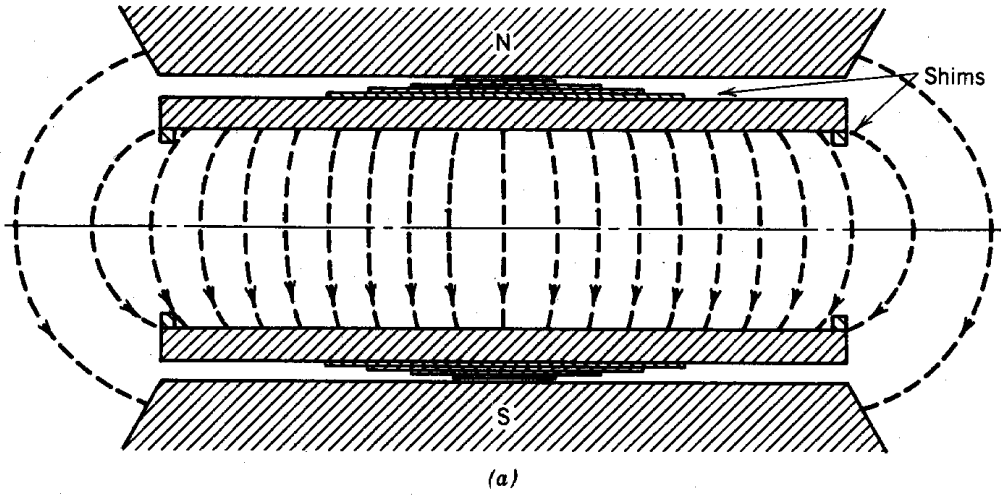


Figure 15.2 Magnetic fields of uniform-field cyclotron. (a) Sectional view of cyclotron magnetic poles showing shims for optimizing field distribution. (b) Radial variation of vertical field magnitude and field index. (M. S. Livingston and J. P. Blewett, *Particle Accelerators*, used by permission, McGraw-Hill Book Co.)

Cyclotrons and Synchrotrons

electrostatic focusing by the accelerating fields is effective for low-energy ions. The electric field pattern between the dees of a cyclotron act as the one-dimensional equivalent of the electrostatic immersion lens discussed in Section 6.6. The main difference from the electrostatic lens is that ion transit-time effects can enhance or reduce focusing. For example, consider the portion of the accelerating half-cycle when the electric field is rising. Ions are focused at the entrance side of the gap and defocused at the exit. When the transit time is comparable to the rf half-period, the transverse electric field is stronger when the ions are near the exit, thereby reducing the net focusing. The converse holds in the part of the accelerating half-cycle with falling field.

In order to extract ions from the machine at a specific location, deflection fields must be applied. Deflection fields should affect only the maximum energy ions. Ordinarily, static electric (magnetic) fields in vacuum extend a distance comparable to the spacing between electrodes (poles) by the properties of the Laplace equation (Section 4.1). Shielding of other ions is accomplished with a septum (separator), an electrode or pole that carries image charge or current to localize deflection fields. An electrostatic septum is illustrated in Figure 15.3. A strong radial electric field deflects maximum energy ions to a radius where $n > 1$. Ions spiral out of the machine

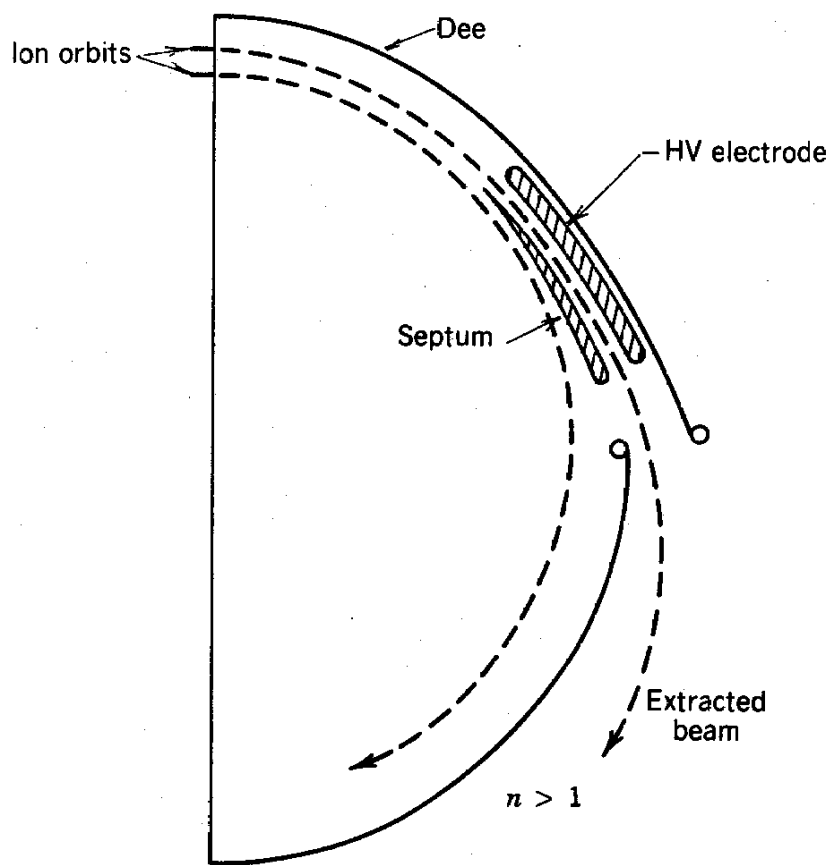


Figure 15.3 Extraction of high-energy ions from cyclotron using electrostatic septum.

Cyclotrons and Synchrotrons

along a well-defined trajectory. Clearly, a septum should not intercept a substantial fraction of the beam. Septa are useful in the cyclotron because there is a relatively large separation between orbits. The separation for non-relativistic ions is

$$\Delta R \cong (R/2) (2qV_o \sin\phi_s/T). \quad (15.3)$$

For example, with a peak dee voltage $V_o = 100$ kV, $\phi_s = 60^\circ$, $R = 1$ m, and $T = 20$ MeV, Eq. (15.3) implies that $\Delta R = 0.44$ cm.

15.2 LONGITUDINAL DYNAMICS OF THE UNIFORM-FIELD CYCLOTRON

In the uniform-field cyclotron, the oscillation frequency of gap voltage remains constant while the ion gyrofrequency continually decreases. The reduction in ω_g with energy arises from two causes: (1) the relativistic increase in ion mass and (2) the reduction of magnetic field magnitude at large radius. Models of longitudinal particle motion in a uniform-field cyclotron are similar to those for a traveling wave linear electron accelerator (Section 13.6); there is no synchronous phase. In this section, we shall develop equations to describe the phase history of ions in a uniform-field cyclotron. As in the electron linac, the behavior of a pulse of ions is found by following individual orbits rather than performing an orbit expansion about a synchronous particle. The model predicts the maximum attainable energy and energy spread as a function of the phase width of the ion pulse. The latter quantity is determined by the geometry of the aperture illustrated in Figure 15.1. The model indicates strategies to maximize beam energy.

The geometry of the calculation is illustrated in Figure 15.4. Assume that the voltage of dee1 relative to dee2 is given by

$$V(t) = V_o \sin\omega t, \quad (15.4)$$

where ω is the rf frequency. The following simplifying assumptions facilitate development of a phase equation:

1. Effects of the gap width are neglected. This is true when the gap width divided by the ion velocity is small compared to $1/\omega$.
2. The magnetic field is radially uniform. The model is easily extended to include the effects of field variations.
3. The ions circulate many times during the acceleration cycle, so that it is sufficient to approximate kinetic energy as a continuous variable and to identify the centroid of the particle orbits with the symmetry axis of the machine.

Cyclotrons and Synchrotrons

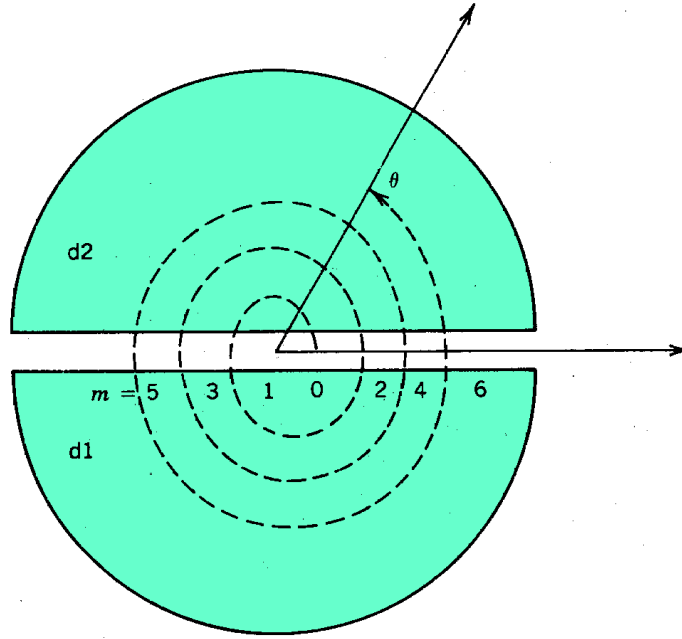


Figure 15.4 Geometry for treating longitudinal dynamics of uniform-field cyclotron.

The phase of an ion at azimuthal position θ and time t is defined as

$$\phi = \omega t - \theta(t). \quad (15.5)$$

Equation (15.5) is consistent with our previous definition of phase (Chapter 13). Particles crossing the gap from dee1 to dee2 at $t = 0$ have $\phi = 0$ and experience zero accelerating voltage. The derivative of Eq. (15.5) is

$$d\phi/dt = \omega - d\theta/dt = \omega - \omega_g, \quad (15.6)$$

where

$$\omega_g = qB_o/\gamma m_i = qc^2 B_o/E. \quad (15.7)$$

The quantity E in Eq. (15.7) is the total relativistic ion energy, $E = T + m_i c^2$. In the limit that $T \ll m_i c^2$, the gyrofrequency is almost constant and Eq. (15.6) implies that particles have constant phase during acceleration. Relativistic effects reduce the second term in Eq. (15.6). If the rf frequency equals the non-relativistic gyrofrequency $\omega = \omega_{go}$, then $d\phi/dt$ is always positive. The limit of acceleration occurs when ϕ reaches 180° . In this circumstance, ions arrive at the gap when the accelerating voltage is zero; ions are trapped at a particular energy and circulate in the cyclotron at constant radius.

Cyclotrons and Synchrotrons

Equation (15.4), combined with the assumption of small gap width, implies that particles making their m th transit of the gap with phase ϕ_m gain an energy.

$$\Delta E_m = qV_o \sin\phi_m. \quad (15.8)$$

In order to develop an analytic phase equation, it is assumed that energy increases continually and that phase is a continuous function of energy, $\phi(E)$. The change of phase for a particle during the transit through a dee is

$$\Delta\phi = (d\phi/dt) (\pi/\omega_g) = \pi [(\omega E/c^2 qB_o) - 1]. \quad (15.9)$$

Dividing Eq. (15.9) by Eq. (15.8) gives an approximate equation for $\phi(E)$:

$$\Delta\phi/\Delta E \cong d\phi/dE \cong (\pi/qV_o \sin\phi) [(\omega E/c^2 qB_o) - 1]. \quad (15.10)$$

Equation (15.10) can be rewritten

$$\sin\phi \, d\phi = (\pi/qV_o) [(\omega E/c^2 qB_o) - 1] \, dE. \quad (15.11)$$

Integration of Eq. (15.11) gives an equation for phase as a function of particle energy:

$$\cos\phi = \cos\phi_o - (\pi/qV_o) [(\omega/2c^2 qB_o) (E^2 - E_o^2) - (E - E_o)], \quad (15.12)$$

where ϕ_o is the injection phase. The cyclotron phase equation is usually expressed in terms of the kinetic energy T . Taking $T = E - m_{oc}^2$ and $\omega_{go} = qB_o/m_i$, Eq. (15.12) becomes

$$\cos\phi = \cos\phi_o - (\pi/qV_o) (1 - \omega/\omega_{go}) T - (\pi/2qV_o m_i c^2) (\omega/\omega_{go}) T^2. \quad (15.13)$$

During acceleration, ion phase may traverse the range $0^\circ < \phi < 180^\circ$. The content of Eq. (15.13) can be visualized with the help of Figure 15.5. The quantity $\cos\phi$ is plotted versus T with ϕ_o as a parameter. The curves are parabolas. In Figure 15.5a, the magnetic field is adjusted so that $\omega = \omega_o$. The maximum kinetic energy is defined by the intersection of the curve with $\cos\phi = -1$. The best strategy is to inject the particles in a narrow range near $\phi_o = 0$. Clearly, higher kinetic energy can be obtained if $\omega < \omega_o$ (Fig. 15.5b). The particle is injected with $\phi_o > 0$. It initially gains on the rf field phase and then lags. A particle phase history is valid only if $\cos\phi$ remains between -1 and +1. In Figure 15.5b, the orbit with $\phi_o = 45^\circ$ is not consistent with acceleration to high energy. The curve for $\phi_o = 90^\circ$ leads to a higher final energy than $\phi_o = 135^\circ$.

Cyclotrons and Synchrotrons

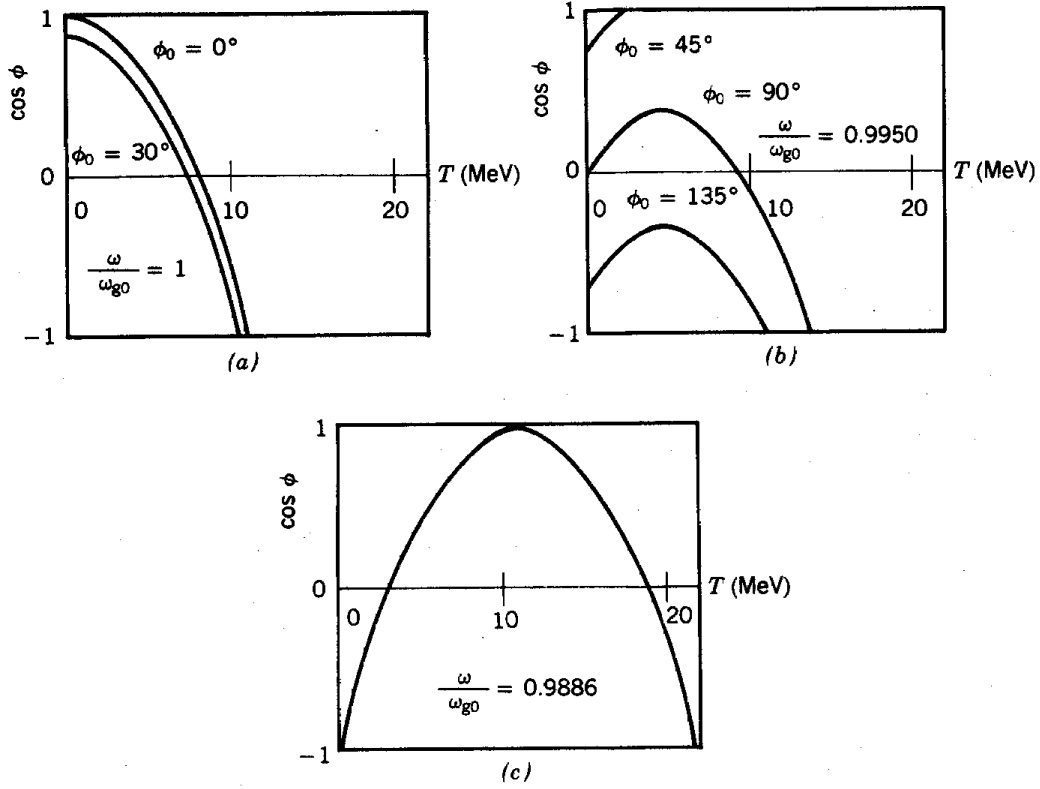


Figure 15.5 Phase histories of protons in uniform-field cyclotron; $\cos \phi$ versus kinetic energy (T) for different injection phase (ϕ_0). (a) $\omega/\omega_{g0} = 1$, where ω is rf angular frequency and ω_{g0} is nonrelativistic gyrofrequency. (b) $\omega/\omega_{g0} = 0.9950$. (c) $\omega/\omega_{g0} = 0.9886$, $\phi_0 = 180^\circ$ (parameters for maximum kinetic energy).

The curves of Figure 15.5 depend on V_o , m_i , and ω/ω_{g0} . The maximum achievable energy corresponds to the curve illustrated in Figure 15.5c. The particle is injected at $\phi_0 = 180^\circ$. The rf frequency is set lower than the non-relativistic ion gyrofrequency. The two frequencies are equal when ϕ approaches 0° . The curve of Figure 15.5c represents the maximum possible phase excursion of ions during acceleration and therefore the longest possible time of acceleration. Defining T_{\max} as the maximum kinetic energy, Figure 15.5c implies, the constraints

$$\cos \phi = -1 \quad \text{for} \quad T = T_{\max} \quad (15.14)$$

and

$$\cos \phi = +1 \quad \text{for} \quad T = \frac{1}{2}T_{\max}. \quad (15.15)$$

The last condition proceeds from the symmetric shape of the parabolic curve. Substitution of Eqs. (15.14) and (15.15) in Eq. (15.13) gives two equations in two unknowns for T_{\max} and ω/ω_{g0} . The

Cyclotrons and Synchrotrons

solution is

$$\omega/\omega_{go} = 1/(1 + T_{\max}/2m_i c^2) \quad (15.16)$$

and

$$T_{\max} \cong \sqrt{16qV_o m_i c^2/\pi}. \quad (15.17)$$

Equation (15.17) is a good approximation when $T \ll m_i c^2$.

Note that the final kinetic energy is maximized by taking V_o large. This comes about because a high gap voltage accelerates particles in fewer revolutions so that there is less opportunity for particles to get out of synchronization. Typical acceleration gap voltages are ± 100 kV. Inspection of Eq. (15.17) indicates that the maximum kinetic energy attainable is quite small compared to $m_i c^2$. In a typical cyclotron, the relativistic mass increase amounts to less than 2%. The small relativistic effects are important because they accumulate over many particle revolutions.

To illustrate typical parameters, consider acceleration of deuterium ions. The rest energy is 1.9 GeV. If $V_o = 100$ kV, Eq. (15.17) implies that $T_{\max} = 31$ MeV. The peak energy will be lower if radial variations of magnetic field are included. With $B_o = 1.5$ T, the non-relativistic gyrofrequency is $f_o = 13.6$ MHz. For peak kinetic energy, the rf frequency should be about 13.5 MHz. The ions make approximately 500 revolutions during acceleration.

15.3 FOCUSING BY AZIMUTHALLY VARYING FIELDS (AVF)

Inspection of Eqs. (15.6) and (15.7) shows that synchronization in a cyclotron can be preserved only if the average bending magnetic field increases with radius. A positive field gradient corresponds to a negative field index in a magnetic field with azimuthal symmetry, leading to vertical defocusing. A positive field index can be tolerated if there is an extra source of vertical focusing. One way to provide additional focusing is to introduce azimuthal variations in the bending field. In this section, we shall study particle orbits in azimuthally varying fields. The intent is to achieve a physical understanding of AVF focusing through simple models. The actual design of accelerators with AVF focusing [K.R. Symon, *et. al.*, Phys. Rev. **103**, 1837 (1956); F.T. Cole, *et. al.*, Rev. Sci. Instrum. **28**, 403 (1957)] is carried out using complex analytic calculations and, inevitably, numerical solution of particle orbits. The results of this section will be applied to isochronous cyclotrons in Section 15.4. In principle, azimuthally varying fields could be used for focusing in accelerators with constant particle orbit radius, such as synchrotrons or betatrons. These configurations are usually referred to as FFAG (fixed-field, alternating-gradient) accelerators. In practice, the cost of magnets in FFAG machines is considerably higher than more conventional approaches, so AVF focusing is presently limited to cyclotrons.

Cyclotrons and Synchrotrons

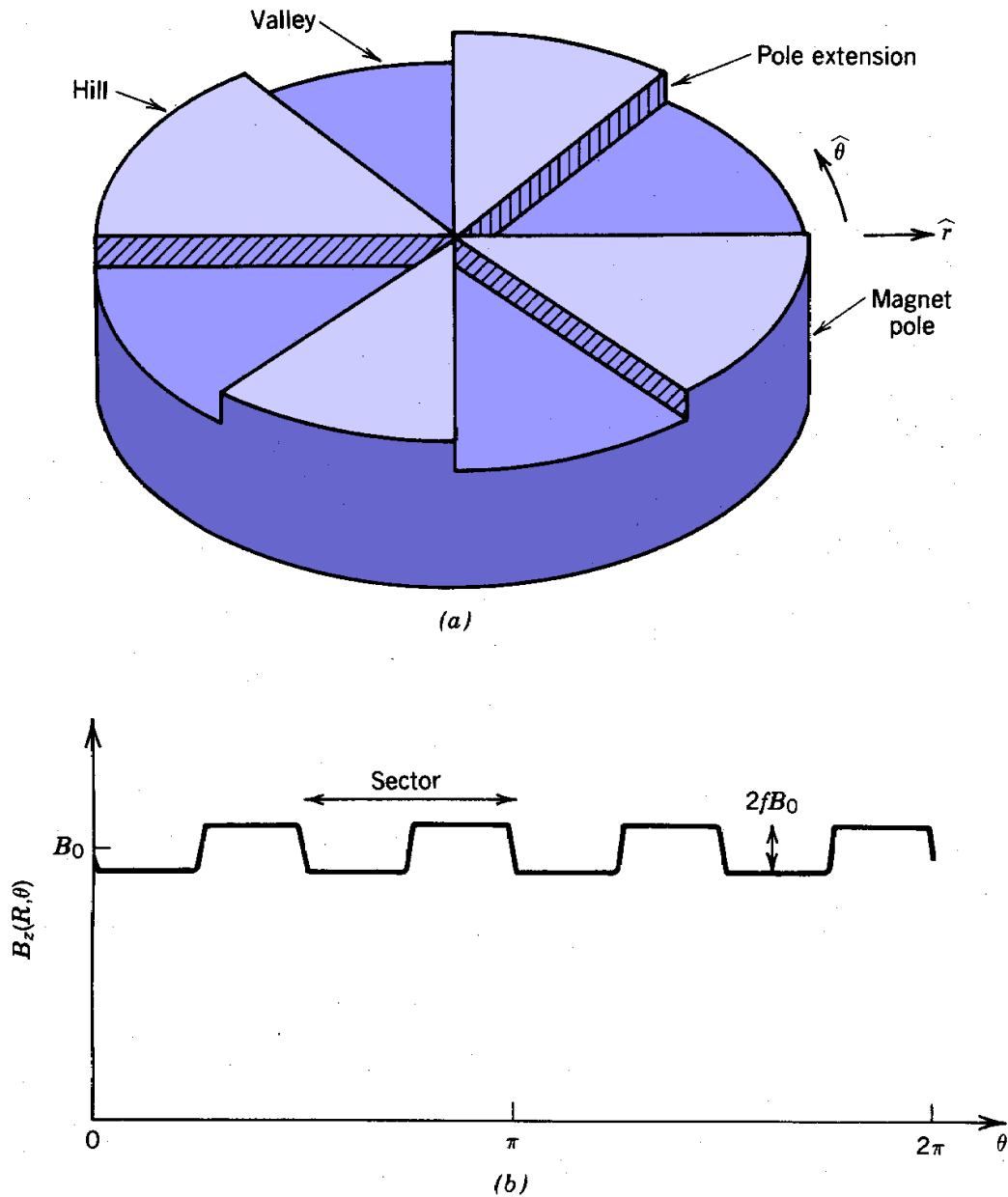


Figure 15.6 Magnetic fields in AVF cyclotron. (a) Magnet pole of AVF cyclotron, no spiral angle. (b) Vertical field amplitude as function of azimuth at constant radius.

Figure 15.6a illustrates an AVF cyclotron field generated by circular magnet poles with wedge-shaped extensions attached. We begin by considering extensions with boundaries that lie along diameters of the poles; more general extension shapes, such as sections with spiral boundaries, are discussed below. Focusing by fields produced by wedge-shaped extensions is usually referred to as *Thomas focusing* [L.H. Thomas, Phys. Rev. **54**, 580 (1938)]. The raised

Cyclotrons and Synchrotrons

regions are called hills, and the recessed regions are called valleys. The magnitude of the vertical magnetic field is approximately inversely proportional to gap width; therefore, the field is stronger in hill regions. An element of field periodicity along a particle orbit is called a *sector*; a sector contains one hill and one valley. The number of sectors equals the number of pole extensions and is denoted N . Figure 15.6a shows a magnetic field with $N = 3$. The variation of magnetic with azimuth along a circle of radius R is plotted in Figure 15.6b. The definition of sector (as applied to the AVF cyclotron) should be noted carefully to avoid confusion with the term *sector magnet*.

The terminology associated with AVF focusing systems is illustrated in Figure 15.6b. The azimuthal variation of magnetic field is called *flutter*. Flutter is represented as a function of position by

$$B_z(R, \theta) = B_o(R) \Phi(R, \theta), \quad (15.18)$$

where $\Phi(R, \theta)$ is the *modulation function* which parametrizes the relative changes of magnetic field with azimuth. The modulation function is usually resolved as

$$\Phi(R, \theta) = 1 + f(R) g(\theta), \quad (15.19)$$

where $g(\theta)$ is a function with maximum amplitude equal to 1 and an average value equal to zero. The modulation function has a θ -averaged value of 1. The function $f(R)$ in Eq. (15.19) is the *flutter amplitude*.

The modulation function illustrated in Figure 15.6b is a step function. Other types of variation are possible. The magnetic field corresponding to a sinusoidal variation of gap width is approximately

$$B_z(R, \theta) = B_o(R) [1 + f(R) \sin N\theta], \quad (15.20)$$

so that

$$\Phi(\theta) = 1 + f(R) \sin N\theta. \quad (15.21)$$

The *flutter function* $F(R)$ is defined as the mean-squared relative azimuthal fluctuation of magnetic field along a circle of radius R :

$$F(R) = \overline{[(B_z(R, \theta) - B_o(R))/B_o(R)]^2} = (1/2\pi) \int_0^{2\pi} [\Phi(R, \theta) - 1]^2 d\theta. \quad (15.22)$$

For example, $F(R) = f(R)^2$ for a step-function variation and $F(R) = \frac{1}{2} f(R)^2$ for the sinusoidal variation of Eq. (15.21).

Particle orbits in azimuthally varying magnetic bending fields are generally complex. In order to develop an analytic orbit theory, simplifying assumptions will be adopted. We limit consideration

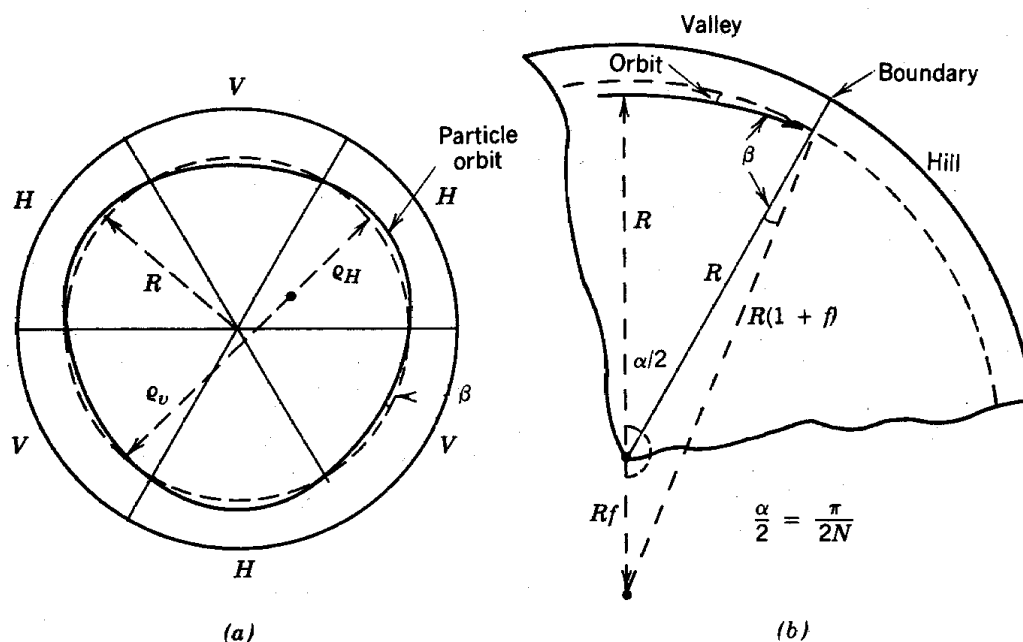


Figure 15.7 Thomas focusing with sharp field region boundaries in the limit of small flutter amplitude. (a) Main orbits: dashed line, uniform field; solid line, field with flutter. (b) Geometry for calculating focusing effect of fringing fields at valley–hill transition.

to a field with sharp transitions of magnitude between hills and valleys (Fig. 15.6b). The hills and valleys occupy equal angles. The step-function assumption is not too restrictive; similar particle orbits result from continuous variations of gap width. Two limiting cases will be considered to illustrate the main features of AVF focusing: (1) small magnetic field variations ($f \ll 1$) and (2) large field variations with zero magnetic field in the valleys. In the latter case, the bending field is produced by a number of separated sector magnets. Methods developed in Chapters 6 and 8 for periodic focusing can be applied to derive particle orbits.

To begin, take $f \ll 1$. As usual, the strategy is to find the equilibrium orbit and then to investigate focusing forces in the radial and vertical directions. The magnetic field magnitude is assumed independent of radius; effects of average field gradient will be introduced in Section 15.4. In the absence of flutter, the equilibrium orbit is a circle of radius $R = \gamma m_i c / q B_o$. With flutter, the equilibrium orbit is changed from the circular orbit to the orbit of Figure 15.7a. In the sharp field boundary approximation, the modified orbit is composed of circular sections. In the hill regions, the radius of curvature is reduced, while the radius of curvature is increased in the valley regions. The main result is that the equilibrium orbit is not normal to the field boundaries at the hill-valley transitions.

There is strong radial focusing in a bending field with zero average field index; therefore, flutter has little relative effect on radial focusing in the limit $f \ll 1$. Focusing in a cyclotron is conveniently characterized by the dimensionless parameter ν (see Section 7.2), the number of betatron wavelengths during a particle revolution. Following the discussion of Section 7.3, we find that

Cyclotrons and Synchrotrons

$$v_r^2 \approx 1 \quad (15.23)$$

for a radially uniform average field magnitude.

In contrast, flutter plays an important part in vertical focusing. Inspection of Figure 15.7a shows that the equilibrium orbit crosses between hill and valley regions at an angle to the boundary. The vertical forces acting on the particle are similar to those encountered in edge focusing (Section 6.9). The field can be resolved into a uniform magnetic field of magnitude $B_0[1 - f(R)]$ superimposed on fields of magnitude $2B_0f(R)$ in the hill regions. Comparing Figure 15.7a to Figure 6.20, the orbit is inclined so that there is focusing at both the entrance and exit of a hill region. The vertical force arises from the fringing fields at the boundary; the horizontal field components are proportional to the change in magnetic field, $2B_0f(R)$. Following Eq. 6.30, the boundary fields act as a thin lens with positive focal length

$$focal\ length \approx (\gamma m_e c / q [2B_0 f]) / |\tan\beta| = -R/2f |\tan\beta|, \quad (15.24)$$

where β is the angle of inclination of the orbit to the boundary. The ray transfer matrix corresponding to transit across a boundary is

$$\mathbf{A}_b = \begin{bmatrix} 1 & 0 \\ -2f \tan\beta/R & 1 \end{bmatrix} \quad (15.25)$$

The inclination angle can be evaluated from the geometric construction of Figure 15.7b. The equilibrium orbit crosses the boundary at about $r = R$. The orbit radii of curvature in the hill and valley regions are $R(1 \pm f)$. To first order, the inclination angle is

$$|\beta| = \pi f/2N, \quad (15.26)$$

where N is the number of sectors. The ray transfer matrix for a boundary is expressed as

$$\mathbf{A}_b = \begin{bmatrix} 1 & 0 \\ -\pi f^2/NR & 1 \end{bmatrix} \quad (15.26)$$

for small β . Neglecting variations in the orbit length through hills and valleys caused by the flutter, the transfer matrix for drift is

$$\mathbf{A}_d = \begin{bmatrix} 1 & \pi R/N \\ 0 & 1 \end{bmatrix} \quad (15.26)$$

Cyclotrons and Synchrotrons

A focusing cell, the smallest element of periodicity, consists of half a sector (a drift region and one boundary transition). The total ray transfer matrix is

$$\mathbf{A} = \begin{bmatrix} 1 & \pi R/N \\ -\pi f^2/NR & 1 - \frac{1}{2}(\pi f/N)^2 \end{bmatrix} \quad (15.29)$$

The phase advance in the vertical direction is

$$\cos \mu \cong 1 - \frac{1}{2}\mu^2 = \frac{1}{2}\text{Tr}\mathbf{A} = 1 - \frac{1}{2}(\pi f/N)^2, \quad (15.30)$$

or

$$\mu \cong \pi f/N. \quad (15.31)$$

The net phase advance during one revolution is equal to $2N\mu$. The number of betatron oscillations per revolution is therefore

$$\nu_z = 2N\mu/2\pi = f. \quad (15.32)$$

The final form is derived by substituting from Eq. (15.31). The vertical number of betatron wavelengths can also be expressed in terms of a flutter function as

$$\nu_z^2 = F. \quad (15.33)$$

Equation (15.33) is-not specific to a step-function field. It applies generally for all modulation functions.

Stronger vertical focusing results if the hill-valley boundaries are modified from the simple diametric lines of Figure 15.6. Consider, for instance, spiral-shaped pole extensions, as shown in Figure 15.8. At a radius R , the boundaries between hills and valleys are inclined at an angle $\zeta(R)$ with respect to a diameter. Spiral-shaped pole extensions lead to an additional inclination of magnitude $\zeta(R)$ between the equilibrium particle orbit and the boundary. The edge fields from the spiral inclination act to alternately focus and defocus particles, depending on whether the particle is entering or leaving a hill region. For example, the spiral of Figure 15.8 is defocusing at a hill-to-valley transition. A focusing-defocusing lens array provides net focusing.

The effect of boundary inclination can easily be derived in the limit that $f \ll 1$ and combined with Thomas focusing for a total ν_z . A focusing cell extends over a sector; a cell consists of a drift region of length $\pi R/N$, a thin lens of focal length $+2f \tan \zeta/R$, a second drift region, and a lens with focal length $-2f \tan \zeta/R$. The total ray transfer matrix for a sector is

Cyclotrons and Synchrotrons

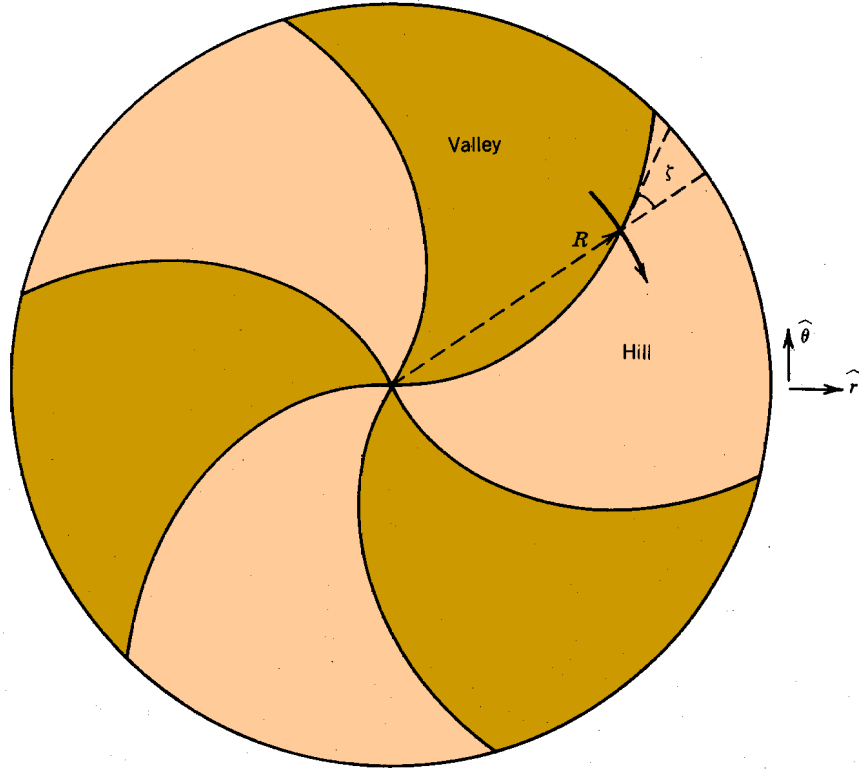


Figure 15.8 Geometry of magnet pole of spiral cyclotron showing inclination angle $\zeta(R)$.

$$A = \begin{bmatrix} [1 + 2f\pi \tan\zeta/N - (2\pi f \tan\zeta/N)^2] & [2\pi R/N - 2f\pi^2 R \tan\zeta/N^2] \\ [-4\pi f^2 \tan^2\zeta/NR] & [1 - 2\pi f \tan\zeta/N] \end{bmatrix} \quad (15.34)$$

Again, identifying $\text{Tr}A$ with $\cos\mu$, we find that

$$\mu \approx \sqrt{2\pi f \tan\zeta} / N. \quad (15.35)$$

Following the method used above, the number of vertical betatron oscillations per revolution is expressed simply as

$$v_z^2 = f^2 (1 + 2\tan\zeta) = F (1 + 2\tan\zeta). \quad (15.36)$$

Vertical focusing forces can be varied with radius through the choice of the spiral shape. The Archimedean spiral is often used; the boundaries of the pole extensions are defined by

Cyclotrons and Synchrotrons

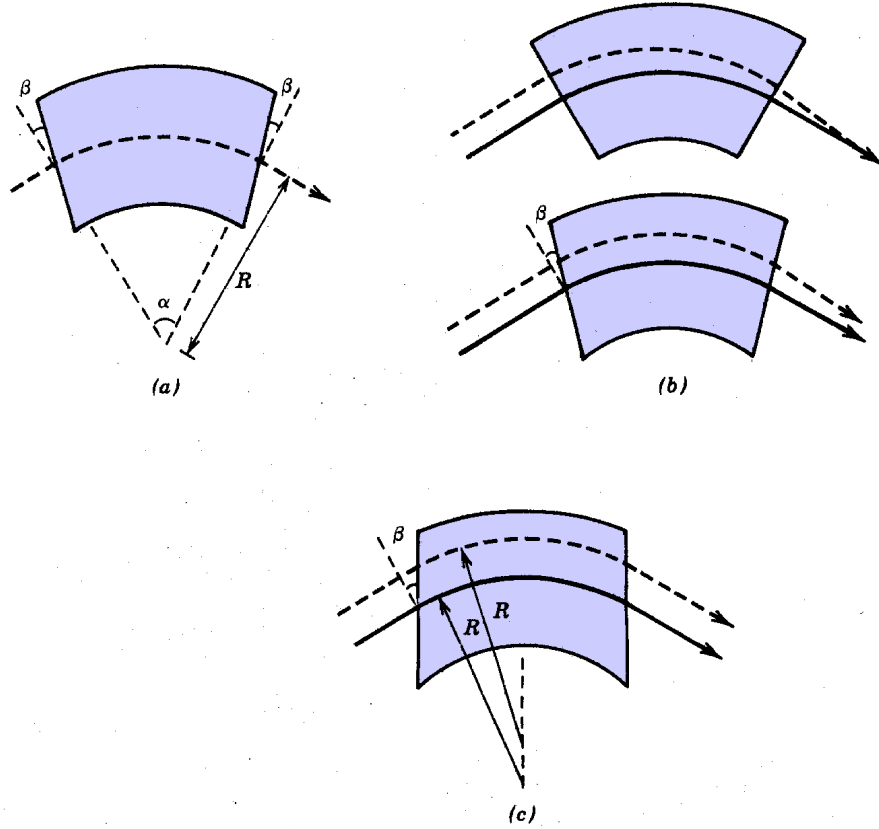


Figure 15.9 Focusing properties of a uniform field sector magnet with inclined boundaries. (a) Definition of angular extent of sector magnet (α) and boundary inclination angle (β) with respect to entering or exiting main particle orbit. (b) Horizontal trajectories of initially parallel particle orbits on main orbit (solid line) and displaced from main orbit (dashed line) with (bottom) and without (top) boundary inclination ($\beta < \frac{1}{2}\alpha$). (c) Horizontal orbits when $\beta = \frac{1}{2}\alpha$.

$$r = A [\theta + 2\pi J/2N], \quad (15.37)$$

where $J = 0, 1, 2, \dots, 2N - 1$. The corresponding inclination angle is

$$\tan \zeta(r) = d(r\theta)/dr = 2r/A. \quad (15.38)$$

Archimedean spiral pole extensions lead to vertical focusing forces that increase with radius.

An analytical treatment of AVF focusing is also possible for a step-function field with $f = 1$. In this case (corresponding to the separated sector cyclotron), the bending field consists of regions of uniform magnetic field separated by field-free regions. Focusing forces arise from the shape of the sector magnet boundaries. As an introduction, consider vertical and radial focusing in a single-sector magnet with inclined boundaries (Fig. 15.9a). The equilibrium orbit in the magnetic field region is a circular section of radius R centered vertically in the gap. The circular section

Cyclotrons and Synchrotrons

subtends an angle α . Assume that the boundary inclinations, β , are equal at the entrance and exit of the magnet.

In the vertical direction, the ray transfer matrix for the magnet is the product of matrices representing edge focusing at the entrance, a drift distance αR , and focusing at the exit. We can apply Eqs. (15.27) and (15.28) to calculate the total ray transfer matrix. In order to calculate focusing in the radial direction, we must include the effect of the missing sector field introduced by the inclination angle P . For the geometry of Figure 15.9a, the inclination reduces radial focusing in the sector magnet. Orbits with and without a boundary inclination are plotted in Figure 15.9b. Figure 15.9c shows the equilibrium particle orbit and an off-axis parallel orbit in a sector magnet with $\beta = \frac{1}{2}\alpha$. The boundary is parallel to a line through the midplane of the magnet; the gyrocenters of both orbits also lie on this line. Therefore, the orbits are parallel throughout the sector and there is no focusing. A value of inclination $\beta < \frac{1}{2}\alpha$ moves the gyrocenter of the off-axis particle to the left; the particle emerges from the sector focused toward the axis. The limit on for radial focusing in a uniform-field sector magnet is

$$\beta = \frac{1}{2}\alpha \quad (15.39)$$

We now turn our attention to the AVF sector field with diametric boundaries shown in Figure 15.10. The equilibrium orbits can be constructed with compass and straightedge. The orbits are circles in the sector magnets and straight lines in between. They must match in position and angle at the boundaries. Figures 15.10a, b show solutions with $N = 2$ and $N = 3$ for hills and valleys occupying equal azimuths ($\alpha = \pi/N$). Note that in all cases the inclination angle of the orbit at a boundary is one-half the angular extent of the sector, $\beta = \frac{1}{2}\alpha$. Figures 15.10c and d illustrate the geometric construction of off-axis horizontal orbits for conditions corresponding to stability ($\alpha > \pi/N, \beta < \frac{1}{2}\alpha$) and instability ($\alpha < \pi/N, \beta > \frac{1}{2}\alpha$). The case of $N = 2$ is unstable for all choices of α . This arises because particles are overfocused when $\alpha > \pi/N$. This effect is clearly visible in Figure 15.10e. It is generally true that particle orbits are unstable in any type of AVF field with $N = 2$.

Spiral boundaries may also be utilized in separated sector fields. Depending on whether the particles are entering or leaving a sector, the edge-focusing effects are either focusing or defocusing in the vertical direction. Applying matrix algebra and the results of Section 6.9, it is easy to show that v_z is

$$v_z^2 = (1 + 2 \tan \zeta) \quad (15.40)$$

for $\alpha = \pi/N$. Spiral boundaries contribute alternate focusing and defocusing forces in the radial direction that are 180° out of phase with the axial forces. For $\alpha = \pi/N$, the number of radial betatron oscillations per revolution is approximately

$$v_r^2 \cong 2 \tan \zeta. \quad (15.41)$$

Cyclotrons and Synchrotrons

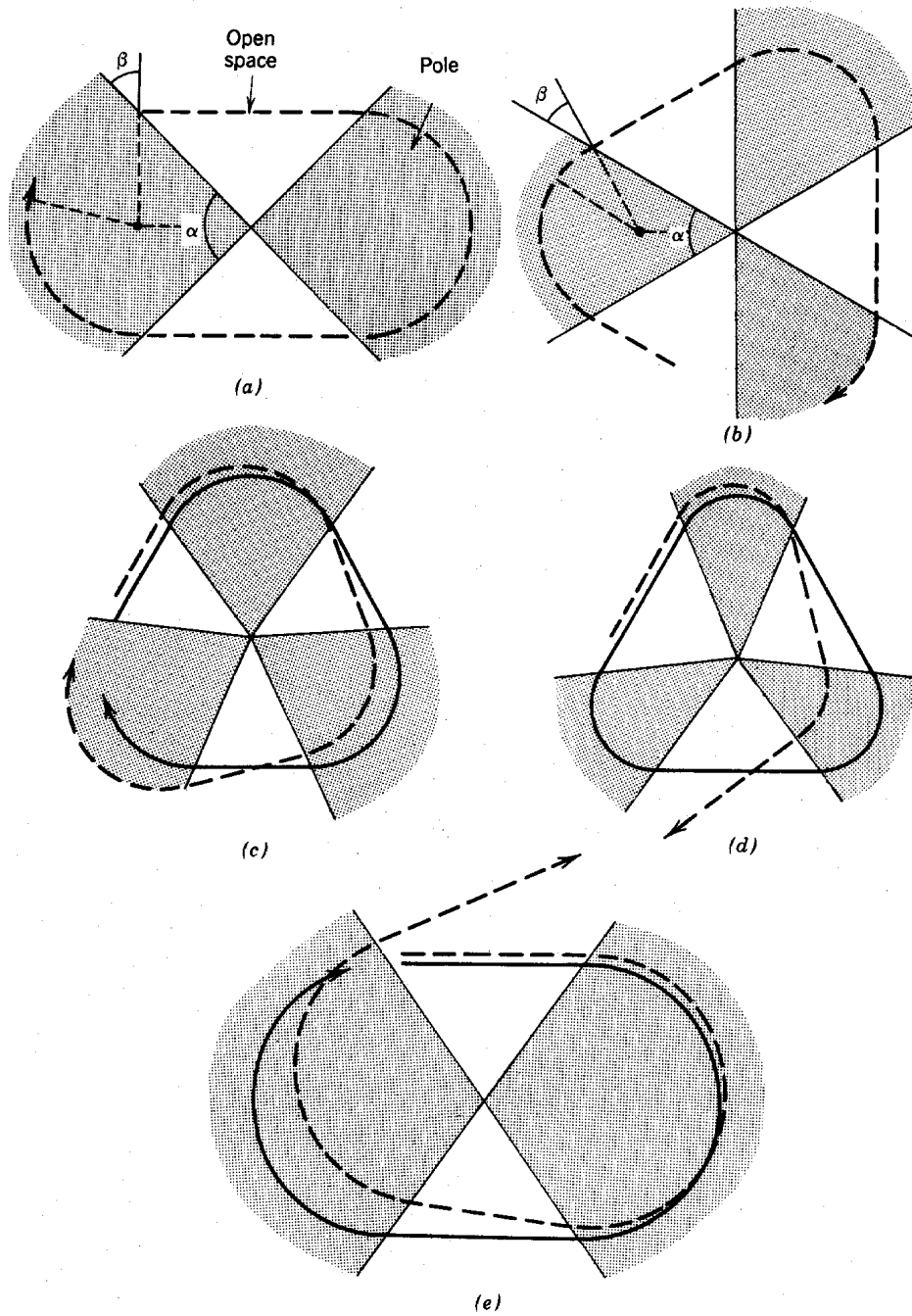


Figure 15.10 Horizontal particle orbits constructed with compass and straightedge in separated sector cyclotron with sector boundaries on diameter showing sector angular extent (α) and boundary inclination angle (β). (a) Main orbit with hills and valleys of equal angular extent ($\beta = \frac{1}{2}\alpha$), $N = 2$. (b) Main orbit with $\beta = \frac{1}{2}\alpha$, $N = 3$. (c) Stable horizontal orbits in three-sector field with $\beta < \frac{1}{2}\alpha$. Solid line, main orbit; dashed line, off-axis orbit. (d) Unstable horizontal orbits when $\beta > \frac{1}{2}\alpha$. (e) Illustration of instability in two-sector field with $\beta < \frac{1}{2}\alpha$.

15.4 THE SYNCHROCYCLOTRON AND THE AVF CYCLOTRON

Following the success of the uniform-field cyclotron, efforts were made to reach higher beam kinetic energy. Two descendants of the cyclotron are the synchrocyclotron and the AVF (isochronous) cyclotron. The machines resolve the problem of detuning between particle revolutions and rf field in quite different ways. Synchrocyclotrons have the same geometry as the SF cyclotron. A large magnet with circular poles produces an azimuthally symmetric vertical field with positive field index. Ions are accelerated from rest to high energy by an oscillating voltage applied between dees. The main difference is that the frequency is varied to preserve synchronism.

There are a number of differences in the operation of synchrocyclotrons and cyclotrons. Synchrocyclotrons are cycled, rather than continuous; therefore, the time-average beam current is much lower. The longitudinal dynamics of particles in a synchrocyclotron do not follow the model of Section 15.2 because there is a synchronous phase. The models for phase dynamics developed in Chapter 13 can be adapted to the synchrocyclotron. The machine can contain a number of confined particle bunches with phase parameters centered about the bunch that has ideal matching to the rf frequency. The beam bunches are distributed as a group of closely spaced turns of slightly different energy. The acceptance of the rf buckets decreases moving away from the ideal match, defining a range of time over which particles can be injected into the machine. In research applications, the number of bunches contained in the machine in a cycle is constrained by the allowed energy spread of the output beam.

There are technological limits on the rate at which the frequency of oscillators can be swept. These limits were particularly severe in early synchrocyclotrons that used movable mechanical tuners rather than the ferrite tuners common on modern synchrotrons. The result is that the acceleration cycle of a synchrocyclotron extends over a longer period than the acceleration time for an ion in a cyclotron. Typically, ions perform between 10,000 and 50,000 revolutions during acceleration in a synchrocyclotron. The high recirculation factor implies lower voltage between the dees. The cycled operation of the synchrocyclotron leads to different methods of beam extraction compared to cyclotrons. The low dee voltage implies that orbits have small separation (< 1 mm), ruling out the use of a septum. On the other hand, all turns can be extracted at the same time by a pulsed field because they are closely spaced in radius. Figure 15.11 illustrates one method of beam extraction from a synchrocyclotron. A pulsed electric field is used to deflect ions on to a perturbed orbit which leads them to a magnetic shield. The risetime of voltage on the kicker electrodes should be short compared to the revolution time of ions. Pulsed extraction is characteristic of cycled machines like the synchrocyclotron and synchrotron. In large synchrotrons with relatively long revolution time, pulsed magnets with ferrite cores are used for beam deflection.

Containment of high-energy ions requires large magnets. For example, a 600-MeV proton has a gyroradius of 2.4 m in a 1.5-T field. This implies a pole diameter greater than 15 ft. Synchro-cyclotron magnets are among the largest monolithic, iron core magnets ever built. The limitation of this approach is evident; the volume of iron required rises roughly as the cube of the kinetic energy. Two synchrocyclotrons are still in operation: the 184-in. machine at Lawrence Berkeley Laboratory and the CERN SC.

Cyclotrons and Synchrotrons

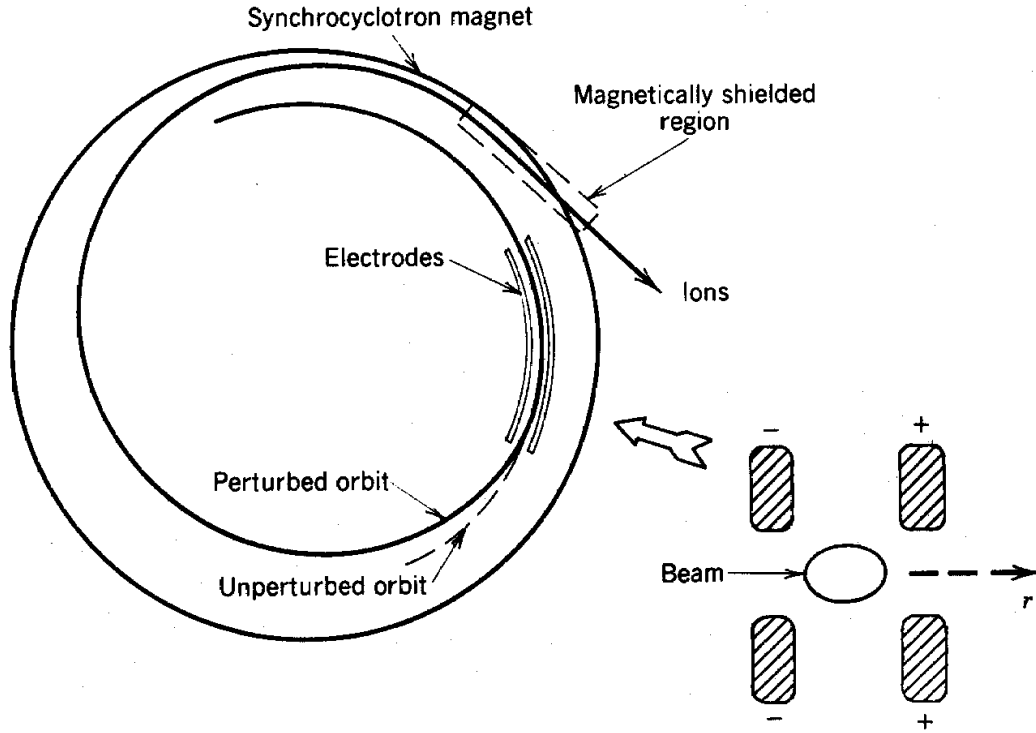


Figure 15.11 Beam extraction from a synchrocyclotron by a pulsed radial electric field.

The AVF cyclotron has fixed magnetic field and rf frequency; it generates a continuous-beam pulse train. Compensation for relativistic mass increase is accomplished by a magnetic field that increases with radius. The vertical defocusing of the negative field index is overcome by the focusing methods described in Section 15.3.

We begin by calculating the radial field variations of the θ -averaged vertical field necessary for synchronization. The quantity $B(R)$ is the averaged field around a circle of radius R and B_0 is the field at the center of the machine. Assume that flutter is small, so that particle orbits approximate circles of radius R , and let $B(R)$ represent the average bending field at R . Near the origin ($R = 0$), the AVF cyclotron has the same characteristics as a uniform field cyclotron; therefore, the rf frequency is

$$\omega = qB_0/m_i, \quad (14.42)$$

where m_i is the rest energy of the ion. Synchronization with the fixed frequency at all radii implies that

$$B(R) = \gamma(R)m_i\omega/q, \quad (15.43)$$

or

Cyclotrons and Synchrotrons

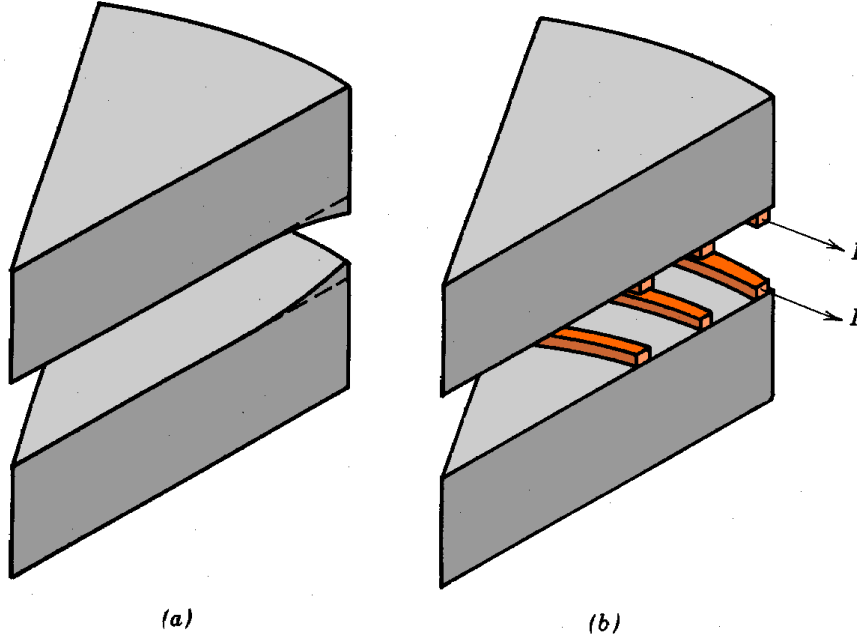


Figure 15.12 Methods for generating vertical magnetic field with negative field index (positive radial gradient). (a) Radial variation of gap width. (b) Trim coils.

$$B(R)/B_o = \gamma(R). \quad (15.44)$$

The average magnetic field is also related to the average orbit radius and ion energy through Eq. (3.38):

$$R = \frac{\gamma(R) \beta m_i c}{qB(R)} = \frac{m_i c}{qB(R)} \sqrt{\gamma^2 - 1} = \frac{m_i c}{qB_o} \frac{\sqrt{\gamma^2 - 1}}{\gamma}. \quad (15.45)$$

Combining Eqs. (15.44) and (15.45), we find

$$B(R)/B_o = \gamma(R) = \sqrt{1 - (qB_o R/m_i c^2)^2}. \quad (15.46)$$

Equation (15.46) gives the following radial variation of the field index:

$$n(R) = - [R/B(R)] [dB(R)/dR] = - (\gamma^2 - 1). \quad (15.47)$$

Two methods for generating a bending field with negative field index (positive radial gradient) are illustrated in Figure 15.12. In the first, the distance between poles decreases as a function of

Cyclotrons and Synchrotrons

radius. This method is useful mainly in small, low-energy cyclotrons. It has the following drawbacks for large research machines:

1. The constricted gap can interfere with the dees.
2. The poles must be shaped with great accuracy.
3. A particular pole shape is suitable for only a single type of ion.

A better method to generate average radial field gradient is the use of *trimming coils*, illustrated in Figure 15.12b. Trimming coils (or *k* coils) are a set of adjustable concentric coils located on the pole pieces inside the magnet gap. They are used to shift the distribution of vertical field. With adjustable trimming coils, an AVF cyclotron can accelerate a wide range of ion species.

In the limit of small flutter amplitude ($f \ll 1$), the radial and vertical betatron oscillations per revolution in an AVF cyclotron are given approximately by

$$v_r^2 \cong 1 - n + F(R)n^2/N^2 + \dots, \quad (15.48)$$

$$v_z^2 \cong n + F(R) + 2F(R) \tan^2 \zeta + F(R)n^2/N^2 + \dots \quad (15.49)$$

Equations (15.48) and (15.49) are derived through a linear analysis of orbits in an AVF field in the small flutter limit. The terms on the right-hand side represent contributions from various types of focusing forces. In Eq. (15.48), the terms have the following interpretations:

Term 1: Normal radial focusing in a bending field.

Term 2: Contribution from an average field gradient ($n < 0$ in an AVF cyclotron).

Term 3: Alternating-gradient focusing arising from the change in the actual field index between hills and valleys. Usually, this is a small effect.

A term involving the spiral angle ζ is absent from the radial equation. This comes about because of cancellation between the spiral term and a term arising from differences of the centrifugal force on particles between hills and valleys.

The terms on the right-hand side of Eq. (15.49) for vertical motion represent the following contributions:

Term 1: Defocusing by the average radial field gradient.

Term 2: Thomas focusing.

Cyclotrons and Synchrotrons

Term 3: FD focusing by the edge fields of a spiral boundary.

Term 4: Same as the third term of Eq. (15.48).

Symmetry considerations dictate that the field index and spiral angle near the center of an AVF cyclotron approach zero. The flutter amplitude also approaches zero at the center because the effects of hills and valleys on the field cancel out at radii comparable to or less than the gap width between poles. As in the conventional cyclotron, electrostatic focusing at the acceleration gaps plays an important role for vertical focusing of low-energy ions. At large radius, there is little problem in ensuring good radial focusing. Neglecting the third term, Eq. (15.48) may be rewritten as

$$v_r \cong \gamma \quad (15.50)$$

using Eq. (15.47). The quantity v_r is always greater than unity; radial focusing is strong. Regarding vertical focusing, the combination of Thomas focusing and spiral focusing in Eq. (15.49) must increase with radius to compensate for the increase in field index. This can be accomplished by a radial increase of $F(R)$ or $\zeta(R)$. In the latter case, boundary curves with increasing ζ (such as the Archimedean spiral) can be used. Isochronous cyclotrons have the property that the revolution time is independent of the energy history of the ions. Therefore, there are no phase oscillations, and ions have neutral stability with respect to the rf phase. The magnet poles of high-energy isochronous cyclotrons must be designed with high accuracy so that particle synchronization is maintained through the acceleration process.

In addition to high-energy applications, AVF cyclotrons are well suited to low-energy medical and industrial applications. The increased vertical focusing compared to a simple gradient field means that the accelerator has greater transverse acceptance. Higher beam currents can be contained, and the machine is more tolerant to field errors (see Section 15.7). Phase stability is helpful, even in low-energy machines. The existence of a synchronous phase implies higher longitudinal acceptance and lower beam energy spread. The AVF cyclotron is much less expensive per ion produced than a uniform-field cyclotron.

In the range of kinetic energy above 100 MeV, the separated sector cyclotron is a better choice than the single-magnet AVF cyclotron. The separated sector cyclotron consists of three or more bending magnets separated by field-free regions. It has the following advantages:

1. Radio-frequency cavities for beam acceleration can be located between the sectors rather than between the magnet poles. This allows greater latitude in designing the focusing magnetic field and the acceleration system. Multiple acceleration gaps can be accommodated, leading to rapid acceleration and large orbit separation.
2. The bending field is produced by a number of modular magnets rather than a single larger unit. Modular construction reduces the problems of fabrication and mechanical stress. This is particularly important at high energy.

Cyclotrons and Synchrotrons

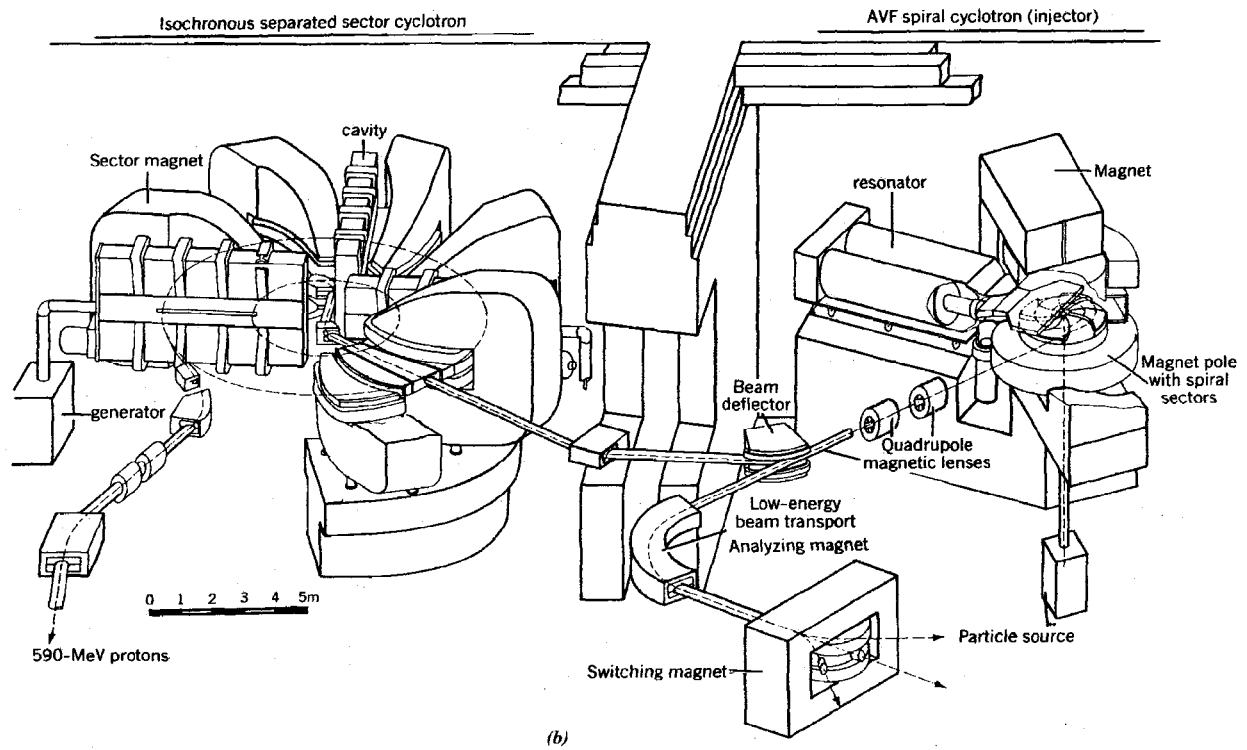
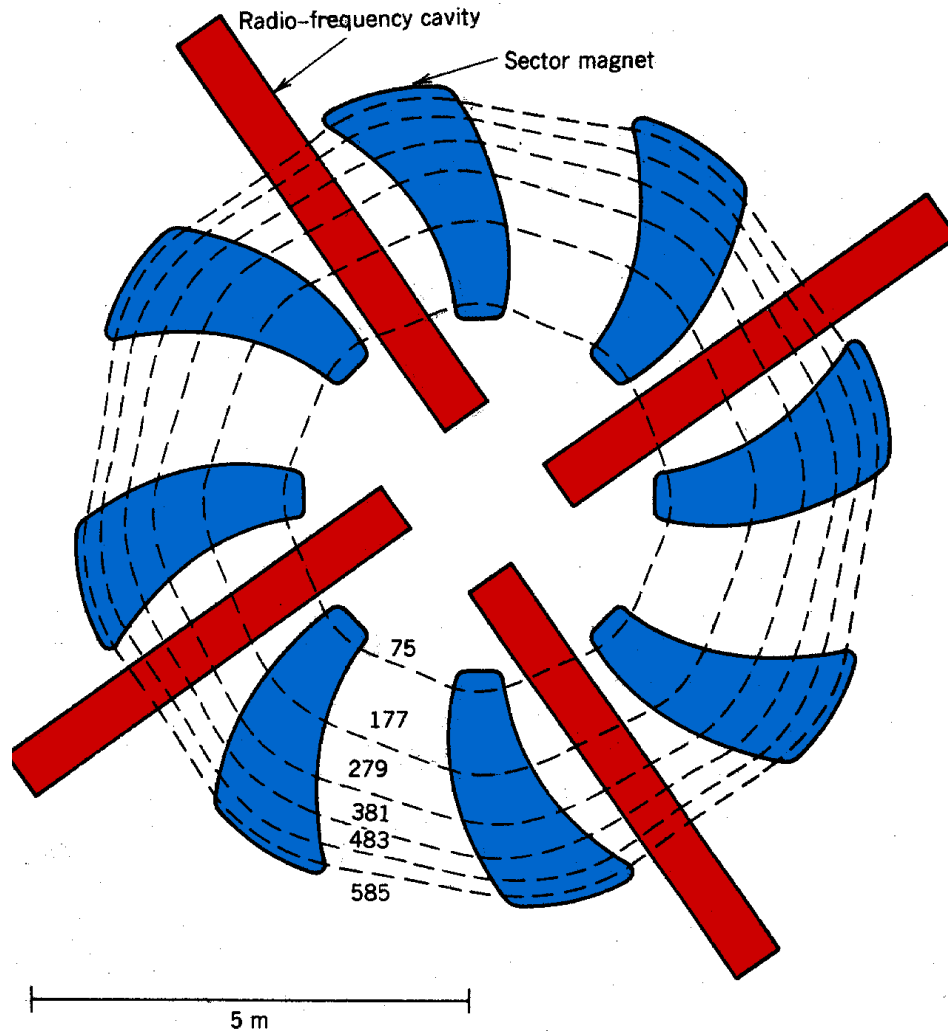


Figure 15.13 SIN Cyclotron. (a) Scale drawing, showing injector AVF cyclotron with spiral extensions of magnet pole and separated sector cyclotron with spiral field boundaries. (b) Overhead view of field boundaries in separated sector cyclotron with calculated proton orbits at 75, 177, 279, 381, 483, and 585 MeV. (Courtesy W. Joho, Swiss Institute for Nuclear Studies.)

Cyclotrons and Synchrotrons



(b)

Figure 15.13 (Continued)

The main drawback of the separated sector cyclotron is that it cannot accelerate ions from zero energy. The beam transport region is annular because structures for mechanical support of the individual magnet poles must be located on axis. Ions are pre-accelerated for injection into a separated sector cyclotron. Pre-acceleration can be accomplished with a low-energy AVF cyclotron or a linac. The injector must be synchronized so that micropulses are injected into the high-energy machine at the proper phase.

Figure 15.13a shows the separated sector cyclotron at the Swiss Nuclear Institute. Parameters of the machine are summarized in Table 15.1. The machine was designed for a high average flux of light ions to generate mesons for applications to radiation therapy and nuclear research. The accelerator has eight spiral sector magnets with a maximum hill field of 2.1 T. Large waveguides

Cyclotrons and Synchrotrons

TABLE 15.1 Parameters of SIN 590 MeV Cyclotron^a

<i>Injector Cyclotron</i>	
Configuration	AVF cyclotron with spiral-shaped sectors
Injection radius	1.5 cm
Extraction radius	105 cm
Pole diameter	250 cm
Peak magnetic field	1.65 T
Number of sectors	4
Maximum spiral angle	55°
Number of trimming coils	12
Magnet power	500 kW
Number of dees	1
rf frequency	4.6–17 MHz (tunable)
Maximum energy gain/turn	160 kV/turn
Beam energy (protons)	10–72 MeV
Beam current (protons)	170 μ A
<i>590-MeV Separated Sector Cyclotron</i>	
Main applications	Research in nuclear physics, solid-state physics and chemistry, pion therapy
Injection radius	210 cm
Extraction radius	445 cm
Peak magnetic field	2.09 T
Averaged field at exit radius	0.87 T
Number of sector magnets	8
Maximum spiral angle	35°
Number of trimming coils	18
Magnet power	670 MW
Number of acceleration cavities	4
rf frequency	50.63 MHz
Maximum energy gain/turn	2200 kV/turn
rf power (maximum)	800 MW
Extraction system	Electrostatic septum

^aSwiss Nuclear Research Institute.

Cyclotrons and Synchrotrons

connect rf supplies to a four acceleration gaps. In operation, the machine requires 0.5 MW of rf input power. The peak acceleration gap voltage is 500 kV. The maximum orbit diameter of the cyclotron is 9 in for a maximum output energy of 590 MeV (protons). The time-averaged beam current is 200 μ A. A standard AVF cyclotron with four spiral-shaped sectors is used as an injector. An increase of average beam current to 1 mA is expected with the addition of a new injector. The injector is a spiral cyclotron with four sectors. The injector operates at 50.7 MHz and generates 72-MeV protons. Figure 15.13b is an overhead view of the magnets and rf cavities in the separated sector cyclotron. Six selected orbits are illustrated at equal energy intervals from 72 to 590 MeV. Note that the distance an ion travels through the sector field increases with orbit radius (negative effective field index). The diagram also indicates the radial increase of the inclination angle between sector field boundaries and the particle orbits.

15.5 PRINCIPLES OF THE SYNCHROTRON

Synchrotrons are resonant circular particle accelerators in which both the magnitude of the bending magnetic field and the rf frequency are cycled. An additional feature of most modern synchrotrons is that focusing forces are adjustable independent of the bending field. Independent variation of the focusing forces, beam-bending field, and rf frequency gives synchrotrons two capabilities that lead to beam energies far higher than those from other types of circular accelerators:

1. The betatron wavelength of particles can be maintained constant as acceleration proceeds. This makes it possible to avoid the orbital resonances that limit the output energy of the AVF cyclotron.
2. The magnetic field amplitude is varied to preserve a constant particle orbit radius during acceleration. Therefore, the bending field need extend over only a small annulus rather than fill a complete circle. This implies large savings in the cost of the accelerator magnets. Furthermore, the magnets can be fabricated as modules and assembled into ring accelerators exceeding 6 km in circumference.

The main problems of the synchrotron are (1) a complex operation cycle and (2) low average flux.

The components of a modern separated function synchrotron are illustrated in Figure 15.14. An ultra-high-vacuum chamber for beam transport forms a closed loop. Circular sections may be interrupted by straight sections to facilitate beam injection, beam extraction, and experiments. Acceleration takes place in a cavity filled with ferrite cores to provide inductive iso a over a broad frequency range. The cavity is similar to a linear induction accelerator cavity. The two differences are (1) an ac voltage is applied across the gap and (2) the ferrites are not driven to saturation to minimize power loss.

Cyclotrons and Synchrotrons

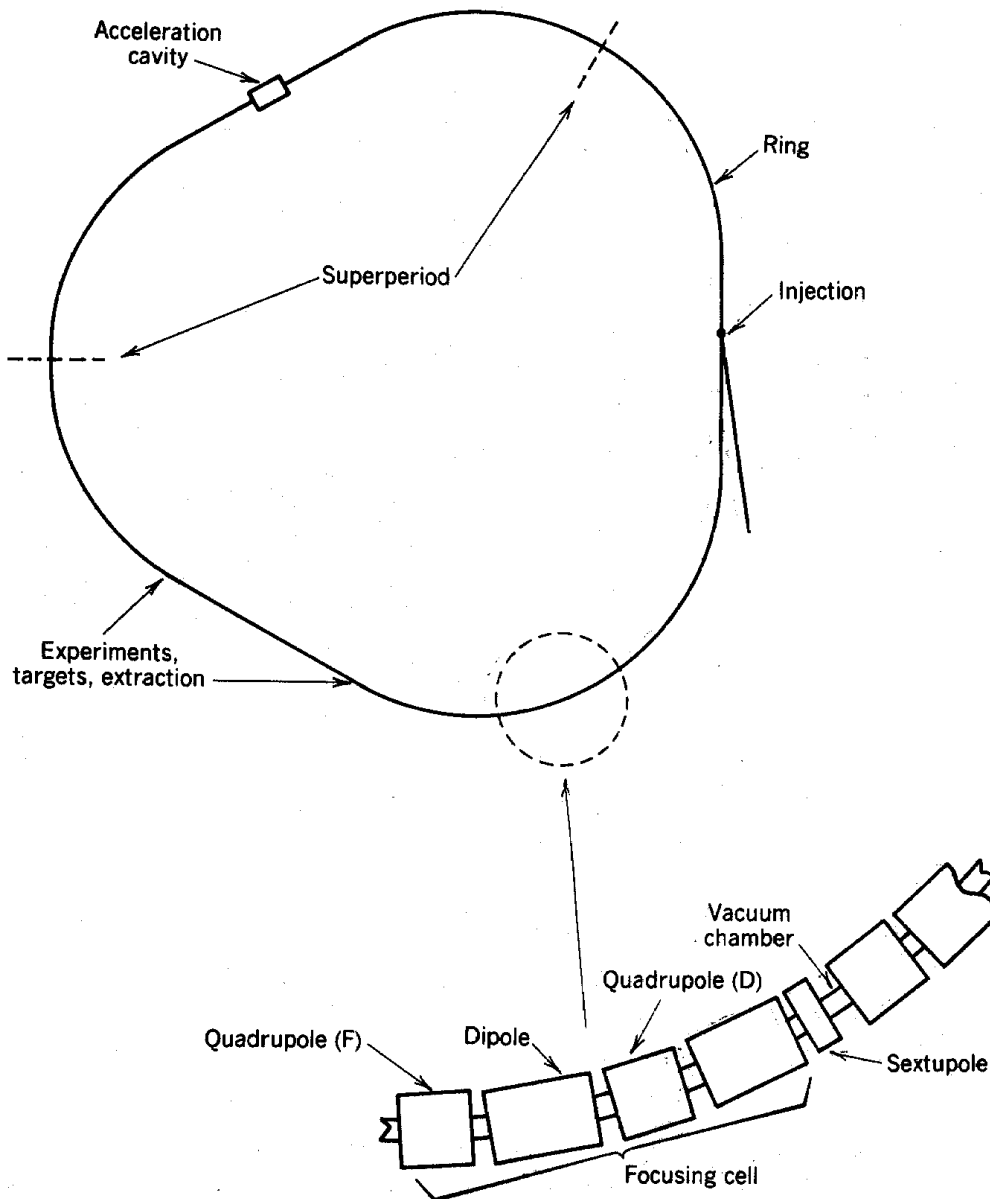


Figure 15.14 Major components and definition of terms in separated function synchrotron.

Beam bending and focusing are accomplished with magnetic fields. The separated function synchrotron usually has three types of magnets, classified according to the number of poles used to generate the field. *Dipole magnets* (Fig. 15.15a) bend the beam in a closed orbit. *Quadrupole magnets* (Fig. 15.15b) (grouped as quadrupole lens sets) focus the beam. *Sextupole magnets* (Fig. 15.15c) are usually included to increase the tolerance of the focusing system to beam energy spread. The global arrangement of magnets around the synchrotron is referred to as a *focusing lattice*. The lattice is carefully designed to maintain a stationary beam envelope. In order to avoid

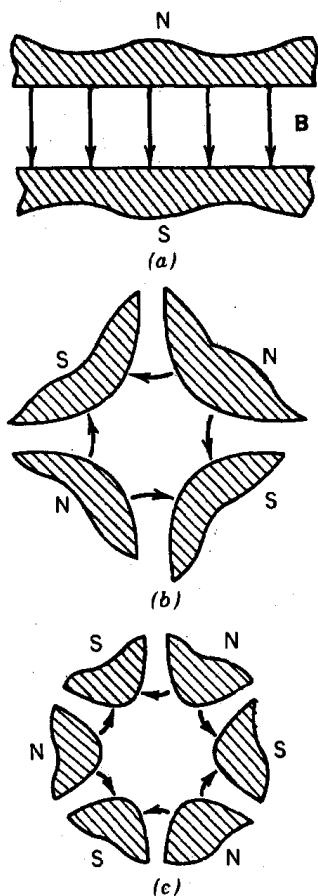


Figure 15.15 Classification of synchrotron magnets. (a) Dipole magnet (bending particle orbits). (b) Quadrupole (transverse focusing). (c) Sextupole (chromatic correction; assuring that particles in a range of energy about the mean have the same ν).

resonance instabilities, the lattice design must not allow betatron wavelengths to equal a characteristic dimension of the machine (such as the circumference). Resonance conditions are parametrized in terms of *forbidden values* of ν_r and ν_z .

A focusing cell is strictly defined as the smallest element of periodicity in a focusing system. A period of a noncircular synchrotron contains a large number of optical elements. A cell may encompass a curved section, a straight section, focusing and bending magnets, and transition elements between the sections. The term *superperiod* is usually used to designate the minimum periodic division of a synchrotron, while focusing cell is applied to a local element of periodicity within a superperiod. The most common local cell configuration is the *FODO* cell. It consists of a focusing quadrupole (relative to the r or z direction), a dipole magnet, a defocusing quadrupole, and another dipole. Horizontal focusing forces in the bending magnets are small compared to that in the quadrupoles. For transverse focusing, the cell is represented as a series of focusing and defocusing lenses separated by drift (open) spaces.

The alternating-gradient synchrotron (AGS) is the precursor of the separated function synchrotron. The AGS has a ring of magnets which combine the functions of beam bending and focusing. Cross sections of AGS magnets are illustrated in Figure 15.16. A strong positive or

Cyclotrons and Synchrotrons

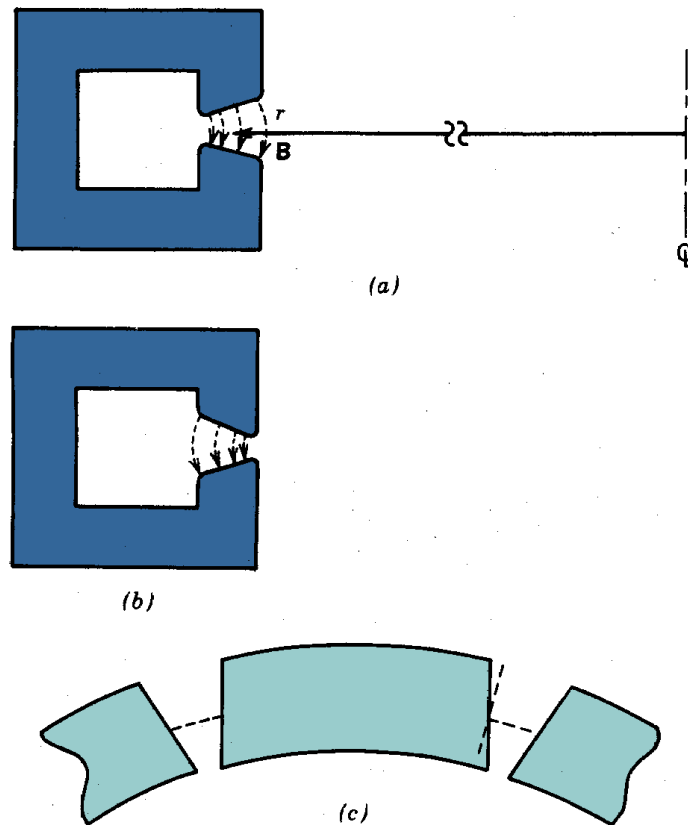


Figure 15.16 Synchrotron Magnets. (a) Magnet in alternating-gradient synchrotron with strong radial focusing and vertical defocusing. (b) AGS magnet with strong vertical focusing and radial defocusing. (c) Overhead view of uniform-field sector magnet boundaries in zero-gradient synchrotron.

negative radial gradient is superimposed on the bending field; horizontal and vertical focusing arises from the transverse fields associated with the gradient (Section 7.3). The magnet of Figure 15.16a gives strong radial focusing and horizontal defocusing, while the opposite holds for the magnet of Figure 15.16b.

Early synchrotrons utilized simple gradient focusing in an azimuthally symmetric field. They were constructed from a number of adjacent bending magnets with uniform field index in the range $0 < n < 1$. These machines are now referred to as *weak focusing synchrotrons* because the betatron wavelength of particles was larger than the machine circumference. The zero-gradient synchrotron (ZGS) (Fig. 15.16c) was an interesting variant of the weak focusing machine. Bending and focusing were performed by sector magnets with uniform-field magnitude (zero gradient). The sector field boundaries were inclined with respect to the orbits to give vertical focusing [via edge focusing (Section 6.9)] and horizontal focusing [via sector focusing (Section 6.8)]. The advantage of the ZGS compared to other weak focusing machines was that higher bending fields could be achieved without local saturation of the poles.

Cyclotrons and Synchrotrons

The limit on kinetic energy in an ion synchrotron is set by the bending magnetic field magnitude and the area available for the machine. The ring radius of relativistic protons is given by

$$R = 3.3E/\bar{B} \quad (m), \quad (15.51)$$

where \bar{B} is the average magnetic field (in tesla) and E is the total ion energy in GeV. Most ion synchrotrons accelerate protons; protons have the highest charge-to-mass ratio and reach the highest kinetic energy per nucleon for a given magnetic field. Synchrotrons have been used for heavy-ion acceleration. In this application, ions are pre-accelerated in a linear accelerator and directed through a thin foil to strip electrons. Only ions with high charge states are selected for injection into the synchrotron.

The maximum energy in an electron synchrotron is set by emission of *synchrotron radiation*. Synchrotron radiation results from the continuous transverse acceleration of particles in a circular orbit. The total power emitted per particle is

$$P = 2cE^4 r_o / 3R^2 (m_o c^2)^3 \quad (\text{watts}), \quad (15.52)$$

where E is the total particle energy and R is the radius of the circle. Power in Eq. (15.52) is given in electron volts per second if all energies on the right-hand side are expressed in electron volts. The quantity r_o is the classical radius of the particle,

$$r_o = q^2 / 4\pi\epsilon_o m_o c^2. \quad (15.53)$$

The classical radius of the electron is

$$r_e = 2.82 \times 10^{-15} \text{ m}. \quad (15.54)$$

Inspection of Eqs. (15.52) and (15.53) shows that synchrotron radiation has a negligible effect in ion accelerators. Compared to electrons, the power loss is reduced by a factor of $(m_e/m_i)^4$. To illustrate the significance of synchrotron radiation in electron accelerators, consider a synchrotron in which electrons gain an energy eV_o per turn. The power input to electrons (in eV/s) is

$$P = cV_o / 2\pi R. \quad (15.55)$$

Setting Eqs. (15.52) and (15.55) equal, the maximum allowed total energy is

$$E \leq [3V_o (m_o c^2)^3 R / 4\pi r_o]^{0.25}. \quad (15.56)$$

Cyclotrons and Synchrotrons

For example, with $R = 20$ m and $V_o = 100$ kV, the maximum energy is $E = 2.2$ GeV. Higher energies result from a larger ring radius and higher power input to the accelerating cavities, but the scaling is weak. The peak energy achieved in electron synchrotrons is about 12 GeV for $R = 130$ m. Linear accelerators are the only viable choice to reach higher electron energy for particle physics research. Nonetheless, electron synchrotrons are actively employed in other areas of applied physics research. They are a unique source of intense radiation over a wide spectral range via synchrotron radiation. New synchrotron radiation facilities are planned as research tools in atomic and solid-state physics.

Synchrotron radiation has some advantageous effects on electron beam dynamics in synchrotrons. The quality of the beam (or the degree to which particle orbit parameters are identical) is actually enhanced by radiation. Consider, for instance, the spread in longitudinal energy in a beam bunch. Synchrotron radiation is emitted over a narrow cone of angle

$$\Delta\theta = (m_e c^2/E) \quad (15.57)$$

in the forward direction relative to the instantaneous electron motion. Therefore, the emission of photons slows electrons along their main direction of motion while making a small contribution to transverse motion. According to Eq. (15.52), higher-energy electrons lose more energy; therefore, the energy spread of an electron bunch decreases. This is the simplest example of beam cooling. The process results in a reduction of the random spread of particle orbits about a mean; hence, the term *cooling*.

The highest-energy accelerator currently in operation is located at the Fermi National Accelerator Laboratory. The 2-km-diameter proton synchrotron consists of two accelerating rings, built in two stages. In the main ring (completed in 1971), beam focusing and bending are performed by conventional magnets. Beam energies up to 450 GeV have been achieved in this ring. After seven years of operation, an additional ring was added in the tunnel beneath the main ring. This ring, known as the energy doubler, utilizes superconducting magnets. The higher magnetic field makes it possible to generate beams with 800 GeV kinetic energy. The total experimental facility, with beam transport elements and experimental areas designed to accommodate the high-energy beams, is known as the Tevatron. A scale drawing of the accelerator and experimental areas is shown in Figure 15.17a. Protons, extracted from a 750-kV electrostatic accelerator, are accelerated in a 200-MeV linear accelerator. The beam is then injected into a rapid cycling booster synchrotron which increases the energy to 8 GeV. The booster synchrotron cycles in 33 ms. The outputs from 12 cycles of the booster synchrotron are used to fill the main ring during a constant-field initial phase of the main ring acceleration cycle. The booster synchrotron has a circumference equal to 1/13.5 that of the main ring. The 12 pulses are injected head to tail to fill most of the main ring circumference.

A cross section of a superconducting bending magnet from the energy doubler is shown in Figure 15.17b. It consists of a central bore tube of average radius 7 cm surrounded by superconducting windings with a spatial distribution calculated to give a highly uniform bending field. The windings are surrounded by a layer of stainless steel laminations to clamp the windings

Cyclotrons and Synchrotrons

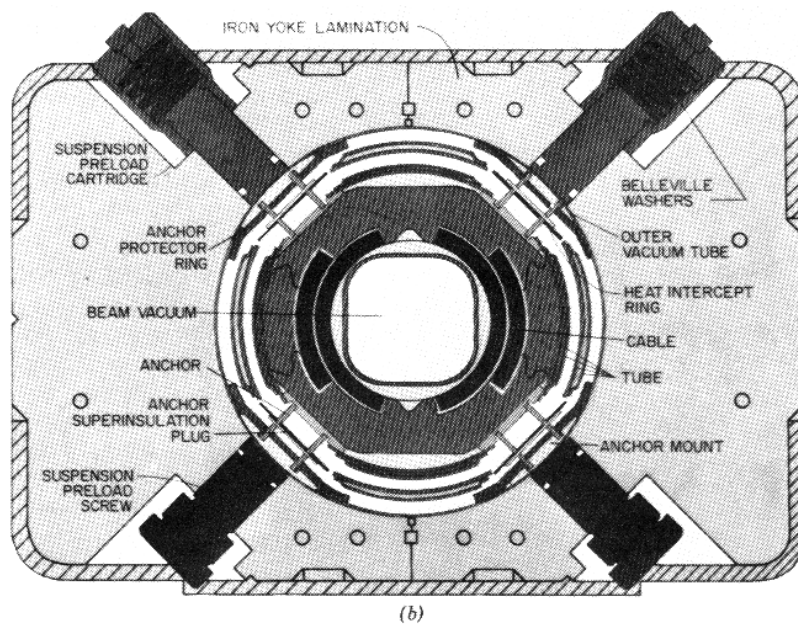
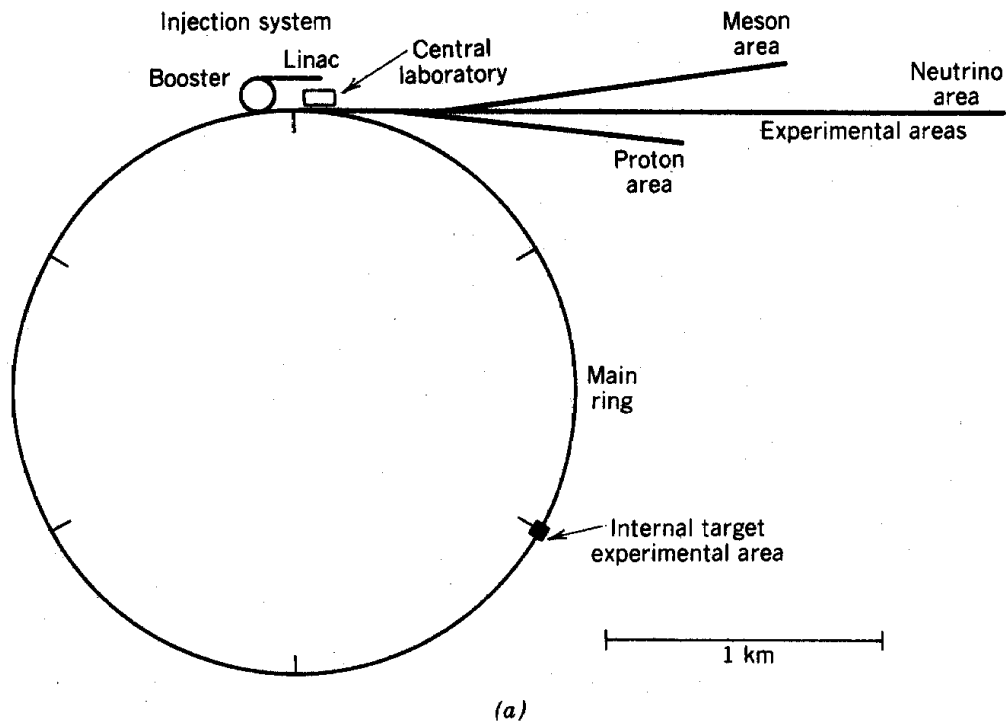


Figure 15.17 FNAL Synchrotron. (a) Scale over head view showing injector accelerators, main accelerator ring, and experimental areas for elementary particle physics research. (b) Cross-sectional view energy doubler superconducting bending magnet. (Courtesy F. Cole, Fermi National Accelerator Laboratory.)

Cyclotrons and Synchrotrons

TABLE 15.2 Parameters of 400-GeV Synchrotron^a

<i>Injector</i>	
Beam energy	750 keV
Particle	p^+
Beam current	200 mA
<i>Linac</i>	
Beam energy	200 MeV
Beam current	100 mA
Beam macropulse length	3–12 μ s
Length	140 m
Configuration	Drift tube linac
Number of drift tubes	295
Frequency	200 MHz
<i>Booster Synchrotron</i>	
Radius	74.1 m
Beam energy	8 GeV
Cycle time	0.067 s
Peak magnetic field	0.7 T
Energy gain/turn	0.7 MeV/turn
Configuration	Alternating gradient, H-type magnets
Number of magnets	96
Pulse rate	15 Hz
Number of rf cavities	16
Frequency excursion	30–53 MHz
Transition energy	4.2 GeV
Peak intensity	10^{12} protons/pulse
<i>Main Ring</i>	
Configuration	Separated function, bending dipole magnets, and quadrupole focusing magnets
Number of magnets	1014
Peak magnetic field	2.0 T
Magnet alignment accuracy	$< \pm 1$ mm
Injection pulses	12
Radius	1000 m
Energy gain rate	100–125 GeV/s
Cycling time (400 GeV)	12 s
Energy gain/turn	2.5 MeV
ν	19.4

^aFermi National Accelerator Laboratory.

Cyclotrons and Synchrotrons

securely to the tube. The assembly is supported in a vacuum cryostat by fiberglass supports, surrounded by a thermal shield at liquid nitrogen temperature. A flow of liquid helium maintains the low temperature of the magnet coils. Bending magnets in the energy doubler are 6.4 m in length. A total of 774 units are necessary. Quadrupoles are constructed in a similar manner; a total of 216 focusing magnets are required. The parameters of the FNAL accelerator are listed in Table 15.2.

Storage rings consist of bending and focusing magnets and a vacuum chamber in which high-energy particles can be stored for long periods of time. The background pressure must be very low to prevent particle loss through collisions. Storage rings are filled with particles by a high-energy synchrotron or a linear accelerator. Their geometry is almost identical to the separated function synchrotron. The main difference is that the particle energy remains constant. The magnetic field is constant, resulting in considerable simplification of the design. A storage ring may have one or more acceleration cavities to compensate for radiative energy loss of electrons or for longitudinal bunching of ions.

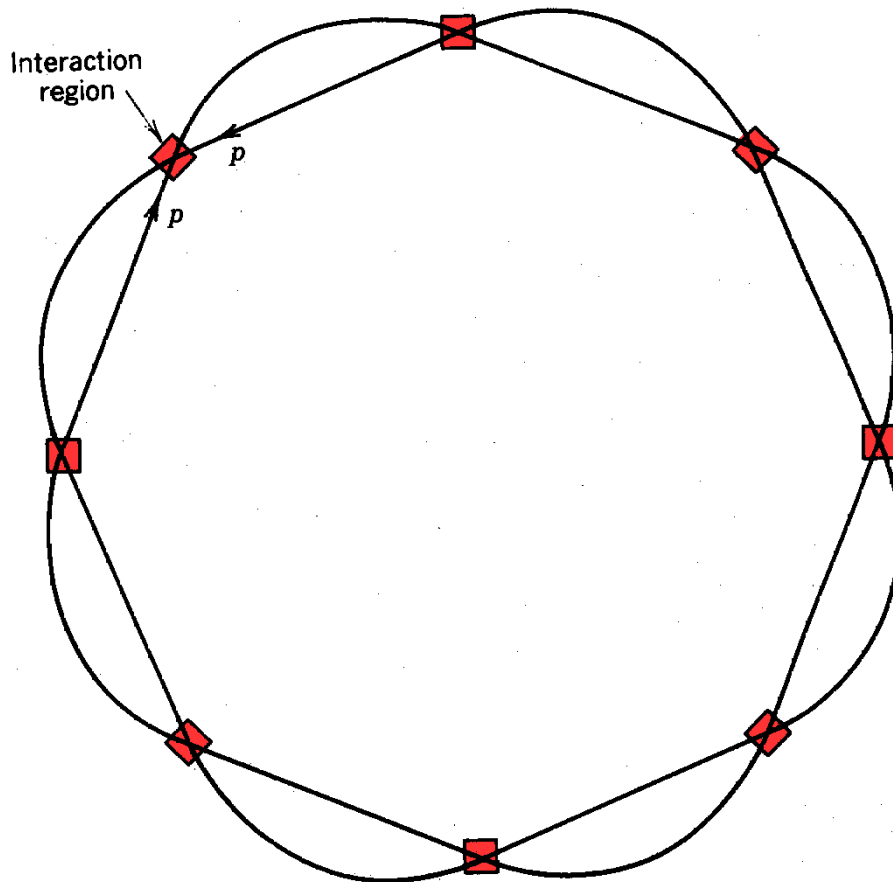


Figure 15.18 Arrangement of Intersecting Storage Ring, CERN.

Cyclotrons and Synchrotrons

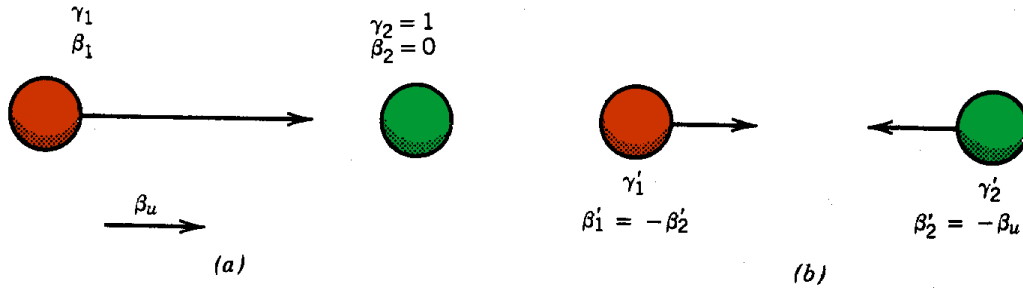


Figure 15.19 Collision of high-energy particle with target particle of equal rest mass. (a) View in stationary frame. (b) View in center-of-momentum frame.

One of the main applications of storage rings is in colliding beam facilities for high-energy particle physics. A geometry used in the ISR (intersecting storage ring) at CERN is shown in Figure 15.18. Two storage rings with straight and curved sections are interleaved. Proton beams circulating in opposite directions intersect at small angles at eight points of the ring.

Proton-proton interactions are studied by detectors located near the intersection points.

Colliding beams have a significant advantage for high-energy physics research. The main requisite for probing the nature of elementary particles is that a large amount of energy must be available to drive reactions with a high threshold. When a moving beam strikes a stationary target (Fig. 15.19a), the kinetic energy of the incident particle is used inefficiently. Conservation of momentum dictates that a large portion of the energy is transformed to kinetic energy of the reaction products. The maximum energy available to drive a reaction in Figure 15.19a can be calculated by a transformation to the center-of-momentum (CM) frame. In the CM frame, the incident and target particles move toward one another with equal and opposite momenta. The reaction products need not have kinetic energy to conserve momentum when viewed in the CM frame; therefore, all the initial kinetic energy is available for the reaction.

For simplicity, assume that the rest mass of the incident particle is equal to that of the target particle. Assume the CM frame moves at a velocity $c\beta_u$ relative to the stationary frame. Using Eq. (2.30), the velocity of the target particle in the CM frame is given by

$$c\beta'_2 = -c\beta_u, \quad (15.58)$$

and the transformed velocity of the incident particle is

$$c\beta'_1 = c(\beta_1 - \beta_u) / (1 - \beta_u\beta_1). \quad (15.59)$$

Both particles have the same value of γ' in the CM frame; the condition of equal and opposite momenta implies

Cyclotrons and Synchrotrons

**TABLE 15.3 Stationary Target: Available Reaction Energy (T_{cm})
Versus Incident Particle Kinetic Energy (T)**

γ	γ'	T_{cm}/T $2(\gamma' - 1)/(\gamma - 1)$	T (protons) (GeV)	T_{cm} (protons) (GeV)
2.00	1.22	0.449	0.94	0.42
4.00	1.58	0.387	2.81	1.09
8.00	2.12	0.320	6.57	2.10
16.00	2.96	0.255	14.07	3.59
32.00	4.06	0.198	29.08	5.76
64.00	5.70	0.149	59.09	8.81
128.00	8.03	0.111	119.13	13.22
256.00	11.34	0.081	239.19	19.37
512.00	16.14	0.059	479.32	28.27
1024.00	23.41	0.044	959.57	42.22

$$-\beta'_2 = \beta'_1. \quad (15.60)$$

Combining Eqs. (15.58), (15.59), and (15.60), we find that

$$\beta_u = (1/\beta_1) - \sqrt{(1/\beta_1^2) - 1}. \quad (15.61)$$

Equation (15.61) allows us to compare the energy invested in the incident particle,

$$T = (\gamma_1 - 1) m_o c^2, \quad (15.62)$$

to the maximum energy available for particle reactions,

$$T_{cm} = 2 (\gamma'_1 - 1) m_o c^2, \quad (15.63)$$

where

$$\gamma_1 = 1/\sqrt{1-\beta_1^2}, \quad \gamma'_1 = 1/\sqrt{1-\beta_u^2}.$$

Cyclotrons and Synchrotrons

Table 15.3 shows T_{cm}/T as a function of γ_1 , along with equivalent kinetic energy values for protons. In the non-relativistic range, half the energy is available. The fraction drops off at high kinetic energy. Increasing the kinetic energy of particles striking a stationary target gives diminishing returns. The situation is much more favorable in an intersecting storage ring. The stationary frame is the CM frame. The CM energy available from ring particles with γ_1 is

$$T_{cm} = 2 (\gamma_1 - 1) m_o c^2. \quad (15.63)$$

TABLE 15.4 High-Energy Accelerators and Storage Rings

Machine	Location	Particle	Energy
<i>Synchrotrons</i>			
KEK	Tsukuba, Japan	p^+	12
ZGS (Zero-gradient synchrotron)	Argonne, Illinois, U.S.A.	p^+	12
CERN PS	Geneva, Switzerland	p^+	28
AGS (Alternating-gradient synchrotron)	Upton, New York, U.S.A.	p^+	32
Serpukhov	Serpukhov, USSR.	p^+	76
CERN SPS	Geneva, Switzerland	p^+	400
Fermilab	Batavia, Illinois, U.S.A.	p^+	800
Cornell Electron Synchrotron	Ithaca, New York, U.S.A.	e^-	12
DESY	Hamburg, Germany	e^-	7
<i>Linear Accelerator</i>			
SLAC	Stanford, California, U.S.A.	e^-	25
<i>Colliding Beam Storage Rings</i>			
ADONE	Frascati, Italy	$e^- e^+$	1.5 + 1.5
DCI	Orsay, France	$e^- e^+$	1.8 + 1.8
SLAC-SPEAR	Stanford, California, U.S.A.	$e^- e^+$	4 + 4
DESY-DORIS	Hamburg, Germany	$e^- e^+$	5 + 5
VEPP-4	Novosibirsk, USSR	$e^- e^+$	7 + 7
CESR	Ithaca, New York, U.S.A.	$e^- e^+$	8 + 8
SLAC-PEP	Stanford, California,	$e^- e^+$	18 + 18
DESY-PETRA	Hamburg, Germany	$e^- e^+$	19 + 19
CERN-ISR	Geneva, Switzerland	$p\bar{p}$	30 + 30

Cyclotrons and Synchrotrons

For example, a 21-GeV proton accelerator operated in conjunction with an intersecting storage ring can investigate the same reactions as a 1000-GeV accelerator with a stationary target. The price to pay for this advantage is reduction in the number of measurable events for physics experiments. A stationary target is usually at solid density. The density of a stored beam is more than 10 orders of magnitude lower. A major concern in intersecting storage rings is *luminosity*, a measure of beam density in physical space and velocity space. Given a velocity-dependent cross section, the luminosity determines the reaction rate between the beams. The required luminosity depends on the cross section of the reaction and the nature of the event detectors.

A list of accelerators and storage rings with the most energetic beams is given in Table 15.4. The energy figure is the kinetic energy measured in the accelerator frame. The history of accelerators for particle physics during the last 50 years has been one of an exponential increase in the available CM energy. Although this is attributable in part to an increase in the size of equipment, the main reason for the dramatic improvement has been the introduction of new acceleration techniques. When a particular technology reached the knee of its growth curve, a new type of accelerator was developed. For example, proton accelerators evolved from electrostatic machines to cyclotrons. The energy limit of cyclotrons was resolved by synchrocyclotrons which lead to the weak focusing synchrotron. The development of strong focusing made the construction of large synchrotrons possible. Subsequently, colliding beam techniques brought about a substantial increase in CM energy from existing machines. At present, there is considerable activity in converting the largest synchrotrons to colliding beam facilities.

In the continuing quest for high-energy proton beams for elementary particle research, the next stated goal is to reach a proton kinetic energy of 20 TeV (20×10^{12} eV). At present, the only identified technique to achieve such an extrapolation is to build an extremely large machine. A 20-TeV synchrotron with conventional magnets operating at an average field of 1 T has a radius of 66 km and a circumference of 414 km. The power requirements of conventional magnets in such a large machine are prohibitive; superconducting magnets are essential. Superconducting magnets can be designed in two ranges. Superconducting coils can be combined with a conventional pole assembly for fields below saturation. Because superconducting coils sustain a field with little power input, there is also the option for high-field magnets with completely saturated poles. A machine with 6-T magnets has a circumference of 70 km.

Studies have recently been carried out for a superconducting super collider (SSC) [see, M. Tigner, Ed., *Accelerator Physics Issues for a Superconducting Super Collider*, University of Michigan, UM HE 84-1, 1984]. This machine is envisioned as two interleaved 20-TeV proton synchrotrons with counter-rotating beams and a number of beam intersection regions. Estimates of the circumference of the machine range from 90 to 160 km, depending on details of the magnet design. The CM energy is a factor of 40 higher than that attainable in existing accelerators. If it is constructed, the SSC may mark the termination point of accelerator technology in terms of particle energy; it is difficult to imagine a larger machine. Considerations of cost versus rewards in building the SSC raise interesting questions about economic limits to our knowledge of the

universe.

15.6 LONGITUDINAL DYNAMICS OF SYNCHROTRONS

The description of longitudinal particle motion in synchrotrons has two unique aspects compared to synchrocyclotrons and AVF cyclotrons. The features arise from the geometry of the machine and the high energy of the particles:

1. Variations of longitudinal energy associated with stable phase confinement of particles in an rf bucket result in horizontal particle oscillations. The synchrotron oscillations sum with the usual betatron oscillations that arise from spreads in transverse velocity. Synchrotron oscillations must be taken into account in choosing the size of the *good field* region of focusing magnets.

2. The range of stable synchronous phase in a synchrotron depends on the energy of particles. This effect is easily understood. At energies comparable to or less than m_0c^2 , particles are non-relativistic; therefore, their velocity depends on energy. In this regime, low-energy particles in a beam bunch take a longer time to complete a circuit of the accelerator and return to the acceleration cavity. Therefore, the accelerating voltage must rise with time at ϕ_s for phase stability ($0 < \phi_s < \pi/2$). At relativistic energies, particle velocity is almost independent of energy; the particle orbit circumference is the main determinant of the revolution time. Low-energy particles have smaller orbit radii and therefore take less time to return to the acceleration gap. In this case, the range of stable phase is $\pi/2 < \phi_s < \pi$. The energy that divides the regimes is called the *transition energy*. In synchrotrons that bridge the transition energy, it is essential to shift the phase of the rf field before the bunched structure of the beam is lost. This effect is unimportant in electron synchrotrons because electrons are always injected above the transition energy.

Models are developed in this section to describe the longitudinal dynamics of particles in synchrotrons. We begin by introducing the quantity γ_t , the transition gamma factor. The parameter characterizes the dependence of particle orbit radius in the focusing lattice to changes in momentum. We shall see that γ_t corresponds to the relativistic mass factor at the transition energy. After calculating examples of γ_t in different focusing systems, we shall investigate the equilibrium conditions that define a synchronous phase. The final step is to calculate longitudinal oscillations about the synchronous particle.

The transition gamma factor is defined by

$$\gamma_t^2 = \frac{\delta p/p_s}{\delta S/S}, \quad (15.64)$$

Cyclotrons and Synchrotrons

where p_s is the momentum of the synchronous particle and S is the pathlength of its orbit around the machine. In a circular accelerator with no straight sections, the equilibrium radius is related to pathlength by $S = 2\pi R$; therefore,

$$\gamma_t^2 = \frac{\delta p/p_s}{\delta R/R}, \quad (15.65)$$

The transition gamma factor must be evaluated numerically for noncircular machines with complex lattices. We will develop simple analytic expressions for γ_t in ideal circular accelerators with weak and strong focusing.

In a weak focusing synchrotron, momentum is related to vertical magnetic field and position by Eq. (3.38), $p = q r B$, so that

$$\delta p/p_s = (\delta r/R) + (\delta B/B_o). \quad (15.66)$$

for $\delta r \ll R$ and $\delta B \ll B_o$. The relative change in vertical field can be related to the change in radius though Eq. (7.18), so that

$$\gamma_t^2 = \frac{\delta p/p_s}{\delta r/R} = (1 - n) = \left(\frac{\omega_r}{\omega_{go}} \right)^2. \quad (15.67)$$

The requirement of stable betatron oscillations in a weak focusing machine limits γ_t to the range $0 < \gamma_t < 1$.

We can also evaluate γ_t for an ideal circular machine with uniform bending field and a strong focusing system. Focusing in the radial direction is characterized by ν_r , the number of radial betatron oscillations per revolution. For simplicity, assume that the particles are relativistic so that the magnetic forces are almost independent of energy. The quantity R is the equilibrium radius for particles of momentum $\gamma_o m_o c$. The radial force expanded about R is

$$F_r \cong -\gamma_o m_o \omega_r^2 \delta r - q B_o c, \quad (15.68)$$

where $\delta r = r - R$. The equilibrium radius for momentum $(\gamma_o + \delta\gamma) m_o c$ is determined by the balance of magnetic forces with centrifugal force, $(\gamma_o + \delta\gamma) m_o c^2/r$. Neglecting second-order terms, we find that

$$\gamma_o m_o \omega_r^2 \delta r + q B_o c \cong \gamma_o m_o c^2/R + \delta\gamma m_o c^2/R - \gamma m_o c^2 \delta r/R^2. \quad (15.69)$$

Zero-order terms cancel, leaving

Cyclotrons and Synchrotrons

$$(\delta r/R) (\omega_r^2 + \omega_{go}^2) \cong (\delta \gamma/\gamma_o) \omega_{go}^2 \cong (\delta p/p) \omega_{go}^2,$$

or

$$\gamma_t^2 \cong 1 + (\omega_r/\omega_{go})^2 = 1 + v_r^2. \quad (15.70)$$

Note that $\gamma_t \gg 1$ in a strong focusing system with high v_r . Therefore, particle position in a strong focusing system is much less sensitive to momentum errors than in a weak focusing system.

Both the magnetic field and frequency of accelerating electric fields must vary in a synchrotron to maintain a synchronous particle with constant radius R . There are a variety of possible acceleration histories corresponding to different combinations of synchronous phase, cavity voltage amplitude, magnetic field strength, and rf frequency. We shall derive equations to relate the different quantities.

We begin by calculating the momentum of the synchronous particle as a function of time. Assume the acceleration gap has narrow width δ so that transit-time effects can be neglected. The electric force acting on the synchronous particle in a gap with peak voltage V_o is

$$qE = (qV_o \sin\phi_s/\delta). \quad (15.71)$$

The momentum change passing through the gap is the electric force times the transit time, or

$$\Delta p_s = (qV_o \sin\phi_s/\delta) (\delta/v_s), \quad (15.72)$$

where v_s is the synchronous particle velocity. Acceleration occurs over a large number of revolutions; it is sufficient to approximate p_s as a continuous function of time. The smoothed derivative of p_s is found by dividing both sides of Eq. (15.72) by the revolution time

$$\tau_o = 2\pi R/v_s. \quad (15.73)$$

The result is

$$dp_s/dt \cong qV_o \sin\phi_s/2\pi R. \quad (15.74)$$

If V_o and ϕ_s are constant, Eq. (15.74) has the solution

$$p_s = p_{so} + (qV_o \sin\phi_s/2\pi R) t. \quad (15.75)$$

Either Eq. (15.74) or (15.75) can be used to find $p_s(t)$. Equation (2.37) can then be used to determine $\gamma_s(t)$ from $p_s(t)$. The time history of the frequency is then constrained. The revolution

Cyclotrons and Synchrotrons

frequency is $\omega_{go} = v_s/R = (c/R) \sqrt{1 - 1/\gamma_s^2}$ through Eq. (2.21). The rf frequency must be an integer multiple of the revolution frequency, $\omega = M\omega_{go}$. In small synchrotrons, M may equal 1 to minimize the rf frequency. In larger machines, M is usually greater than unity. In this case, there are M circulating beam bunches contained in the ring. The rf frequency is related to the particle energy by

$$\omega = (Mc/R) \sqrt{1 - 1/\gamma_s^2}. \quad (15.77)$$

Similarly, the equation $B_o = \gamma_o m_o v_s / qR$ implies that the magnetic field magnitude is

$$B_o = (m_o c / qR) \sqrt{\gamma_s^2 - 1}. \quad (15.78)$$

The rf frequency and magnetic field are related to each other by

$$\omega = \frac{MqB_o/m_o}{\sqrt{1 + (qB_o R/m_o c)^2}}. \quad (15.79)$$

As an example of the application of Eqs. (15.75), (15.77), and (15.78), consider the parameters of a moderate-energy synchrotron (the Bevatron). The injection and final energies for protons are 9.8 MeV and 6.4 GeV. The machine radius is 18.2 m and $M = 1$. The variations of rf frequency and B_o during an acceleration cycle are plotted in Figure 15.20. The magnetic field rises from 0.025 to 1.34 T and the frequency ($f = \omega/2\pi$) increases from 0.37 to 2.6 MHz.

The reasoning that leads to Eq. (15.74) can also be applied to derive a momentum equation for a nonsynchronous particle. Again, averaging the momentum change around one revolution,

$$dp/dt \cong (qV_o/2\pi R) \sin\phi, \quad (15.80)$$

where R is the average radial position of the particle. Substituting $\delta p = p - p_s$, we find (as in Section 13.3) that

$$d\delta p/dt = (qV_o/2\pi R) (\sin\phi - \sin\phi_s) = (qV_o \omega_{go}/2\beta_s c) (\sin\phi - \sin\phi_s). \quad (15.81)$$

Applying Eq. (15.6), changes of phase can be related to the difference between the orbital frequency of a nonsynchronous particle to the rf frequency,

$$d\phi/dt = \omega - M\omega_g. \quad (15.82)$$

The orbital frequency must be related to variations of relativistic momentum in order to generate a closed set of equations. The revolution time for a nonsynchronous particle is $\tau = 2\pi r/v = 2\pi/\omega_g$,

Cyclotrons and Synchrotrons

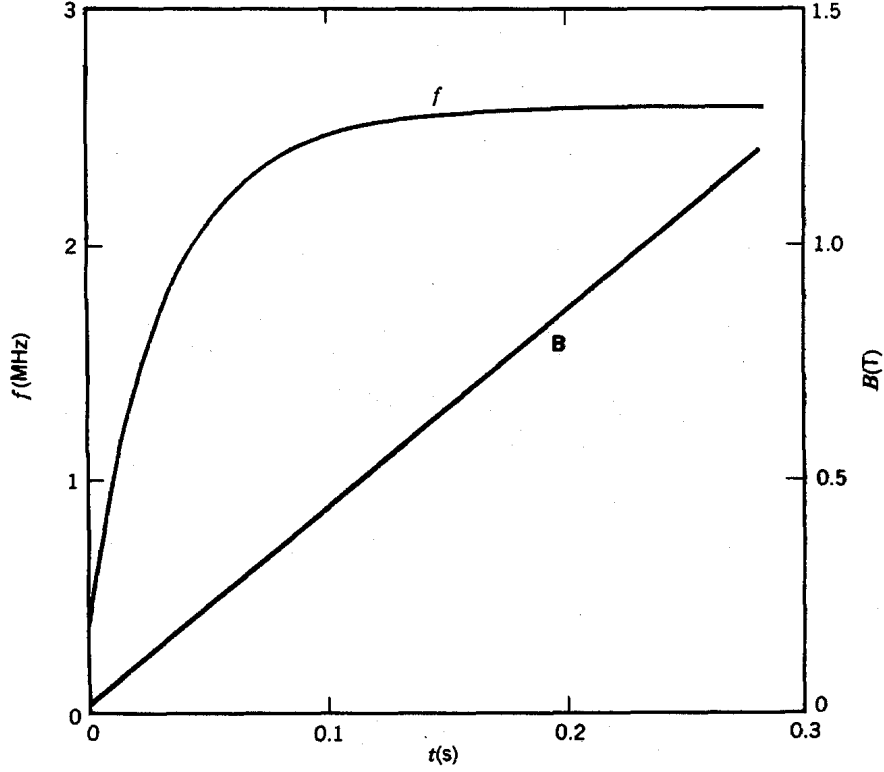


Figure 15.20 Variation of magnetic field and rf frequency during acceleration cycle of protons from 9.4 MeV to 5.6 GeV (Bevatron).

Differential changes in τ arise from variations in particle velocity and changes in orbit radius. The following equations pertain to small changes about the parameters of the synchronous particle orbit:

$$\delta\tau/\tau_o = -\delta\omega_g/\omega_{go} = (\delta r/R) - (\delta v/v_s) = (\delta r/R) - (\delta\beta/\beta_s). \quad (15.83)$$

The differential change in momentum ($p = \gamma m_o \beta c$) is

$$(\delta p/p_s) = \delta\gamma/\gamma_o + \delta\beta/\beta_s = \delta\beta/\beta_s / (1 - \beta_s^2). \quad (15.84)$$

The final form is derived from Eq. (2.22) with some algebraic manipulation. Noting that $\delta\beta/\beta_s = (1 - \beta_s^2) (\delta p/p_s)$, we find that

$$-\delta\omega_g/\omega_{go} = (\delta r/R) - (\delta p/p_s) / \gamma_s^2 = [(1/\gamma_t^2) - (1/\gamma_s^2)] (\delta p/p_s). \quad (15.85)$$

Equation (15.85) implies that

Cyclotrons and Synchrotrons

$$d\omega_g/dt = - (d\delta p/dt) (\omega_{go}/p_s) [(1/\gamma_t^2) - (1/\gamma_s^2)]. \quad (15.86)$$

Equations (15.81), (15.82), and (15.86) can be combined into a single equation for phase in the limit that the parameters of the synchronous particle and the rf frequency change slowly compared to the time scale of a phase oscillation. This is an excellent approximation for the long acceleration cycle of synchrotrons. Treating ω as a constant in Eq. (15.82), we find

$$d^2\phi/dt^2 = - M (d\omega_g/dt). \quad (15.87)$$

Combining Eqs. (15.85), (15.86), and (15.87), the following equation describes phase dynamics in the synchrotron:

$$d^2\phi/dt^2 = (M\omega_{go}^2/\gamma_o m_o c^2 \beta_s^2) (eV_o/2\pi) [(1/\gamma_t^2) - (1/\gamma_s^2)] (\sin\phi - \sin\phi_s). \quad (15.88)$$

Equation (15.88) describes a nonlinear oscillator; it is similar to Eq. (13.21) with the exception of the factor multiplying the sine functions. We discussed the implications of Eq. (13.21) in Section 13.3, including phase oscillations, regions of acceptance for longitudinal stability, and compression of phase oscillations. Phase oscillations in synchrotrons have two features that are not encountered in linear accelerators:

1. Phase oscillations lead to changes of momentum about p_s and hence to oscillation of particle orbit radii. These radial oscillations are called *synchrotron oscillations*.
2. The coefficient of the sine terms may be either positive or negative, depending on the average particle energy.

In the limit of small phase excursion ($\Delta\phi \ll 1$), the angular frequency for phase oscillations in a synchrotron is

$$\omega_s = \omega_{go} \sqrt{- \frac{M \cos\phi_s}{2\pi\beta_s^2} \frac{eV_o}{\gamma_s m_o c^2} \left(\frac{1}{\gamma_t^2} - \frac{1}{\gamma_s^2} \right)} \quad (15.89)$$

Note that the term in brackets contains dimensionless quantities and a factor proportional to the ratio of the peak energy gain in the acceleration gap divided by the particle energy. This is a very small quantity; therefore, the synchrotron oscillation frequency is small compared to the frequency for particle revolutions or betatron oscillations. The radial oscillations occur at angular frequency

Cyclotrons and Synchrotrons

w_s . In the range well beyond transition ($\gamma_s \gg \gamma_t$), the amplitude of radial oscillations can be expressed simply as

$$\delta r \cong R (\Delta\phi/M) (\omega_s/\omega_{go}), \quad (15.90)$$

where $\Delta\phi$ is the maximum phase excursion of the particle from ϕ_s .

The behavior of the expression $[(1/\gamma_t^2) - (1/\gamma_s^2)]$ determines the range of stable phase and the transition energy. For large γ_t or small γ_s , the expression is negative. In this case, the stability range is the same as in a linear accelerator, $0 < \phi_s < \pi/2$. At high values of γ_s , the sign of the expression is positive, and the stable phase regime becomes $\pi/2 < \phi_s < \pi$.

In a weak focusing synchrotron, γ_t is always less than unity; therefore, particles are in the post-transition regime at all values of energy. Transition is a problem specific to strong focusing synchrotrons. The transition energy in a strong focusing machine is given approximately by

$$E_t = (m_o c^2) \gamma_r. \quad (15.91)$$

15.7 STRONG FOCUSING

The strong focusing principle [N. C. Christofilos, U.S. Patent No. 2,736,799 (1950)] was in large part responsible for the development of synchrotrons with output beam kinetic energy exceeding 10 GeV. Strong focusing leads to a reduction in the dimensions of a beam for a given transverse velocity spread and magnetic field strength. In turn, the magnet gap and transverse extent of the *good field region* can be reduced, bringing about significant reductions in the overall size and cost of accelerator magnets.

Weak focusing refers to beam confinement systems in circular accelerators where the betatron wavelength is longer than the machine circumference. The category includes the gradient-type field of betatrons and uniform-field cyclotrons. Strong focusing accelerators have $\lambda_b < 2\pi R$, a consequence of the increased focusing forces. Examples are the alternating-gradient configuration and *FD* or *FODO* combinations of quadrupole lenses. Progress in rf linear accelerators took place largely in the early 1950s after the development of high-power rf equipment. Although some early ion linacs were built with solenoidal lenses, all modern machines use strong focusing quadrupoles, either magnetic or electric.

The advantage of strong focusing can be demonstrated by comparing the vertical acceptance of a weak focusing circular accelerator to that of an alternating-gradient (AG) machine. Assume that the AG field consists of *FD* focusing cells of length l (along the beam orbit) with field index $\pm n$, where $n \gg 1$. The vertical position of a particle at cell boundaries is given by

$$z = z_o \cos(M\mu + \phi), \quad (15.92)$$

where

Cyclotrons and Synchrotrons

$$\mu = \cos^{-1} [\cos(\sqrt{n}\omega_{go}/v_s) \cosh(\sqrt{n}\omega_{go}/v_s)]$$

and M is the cell number. For $\mu \leq 1$, the orbit consists of a sinusoidal oscillation extending over many cells with small-scale oscillations in individual magnets. Neglecting the small oscillations, the orbit equation for particles on the beam envelope is

$$z \cong z_o \cos(\mu S/l + \phi), \quad (15.93)$$

where S , the distance along the orbit, is given by $S = Ml$. The angle of the orbit is approximately

$$z' \cong - (z_o \mu / l) \sin(\mu S/l + \phi). \quad (15.94)$$

Combining Eqs. (15.93) and (15.94), the vertical acceptance is

$$A_v = \pi z_o z_o' = \pi z_o^2 \mu / l. \quad (15.95)$$

In a weak focusing system, vertical orbits are described by

$$z \cong z_o \cos(\sqrt{n}S/R + \phi). \quad (15.96)$$

Following the same development, the vertical acceptance is

$$A_v = \pi z_o^2 \sqrt{n} / R. \quad (15.97)$$

In comparing Eqs. (15.95) and (15.97), note that the field index for weak focusing must be less than unity. In contrast, the individual field indices of magnets in the alternating gradient are made as large as possible, consistent with practical magnet design. Typically, the field indices are chosen to give $\mu \sim 1$. For the same field strength, the acceptance of the strong focusing system is therefore larger by a factor on the order of R/l or $N/2\pi$, where N is the number of focusing cells. The quantity N is a large number. For example, $N = 60$ in the AGS accelerator at Brookhaven National Laboratory.

The major problem of strong focusing systems is that they are sensitive to alignment errors and other perturbations. The magnets of a strong focusing system must be located precisely. We shall estimate the effects of alignment error in a strong focusing system using the transport matrix formalism (Chapter 8). The derivation gives further insight into the origin of resonant instabilities introduced in Section 7.2.

Cyclotrons and Synchrotrons

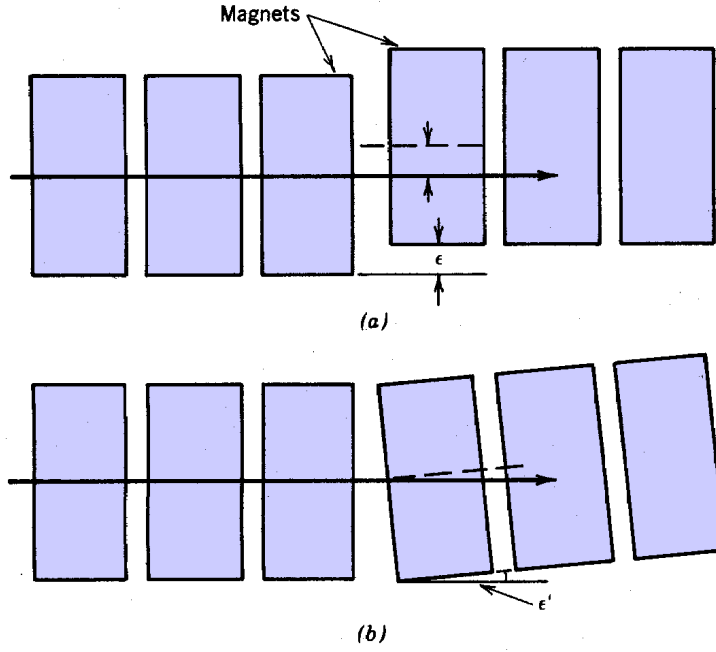


Figure 15.21 Alignment errors between magnets in strong focusing system. (a) Error in position. (b) Error in angle.

For simplicity, consider a circular strong focusing machine with uniformly distributed cells. Assume that there is an error of alignment in either the horizontal or vertical direction between two cells. The magnets may be displaced a distance ϵ , as shown in Figure 15.21a. In this case, the position component of an orbit vector is transformed according to

$$x \Rightarrow x + \epsilon \quad (15.98)$$

when the particle crosses the boundary. An error in magnet orientation by an angle ϵ' (Fig. 15.21b) causes a change in the angular part of the orbit vector:

$$x' \Rightarrow x' + \epsilon' \quad (15.99)$$

The general transformation at the boundary is

$$\mathbf{u}_{n+1} = \mathbf{u}_n + \boldsymbol{\epsilon}, \quad (15.100)$$

where $\boldsymbol{\epsilon} = (\epsilon, \epsilon')$.

Let \mathbf{A} be the transfer matrix for a unit cell of the focusing system and assume that there are N cells distributed about the circle. The initial orbit vector of a particle is \mathbf{u}_0 . For convenience, \mathbf{u}_0 is defined at a point immediately following the imperfection. After a revolution around the machine and traversal of the field error, the orbit vector becomes

Cyclotrons and Synchrotrons

$$\mathbf{u}_N = \mathbf{A}^N \mathbf{u}_0 + \boldsymbol{\varepsilon}. \quad (15.101)$$

The orbit vector after two revolutions, is

$$\mathbf{u}_{2N} = \mathbf{A}^N \mathbf{u}_N + \boldsymbol{\varepsilon} = \mathbf{A}^{2N} \mathbf{u}_0 + (\mathbf{A}^N + \mathbf{I}) \boldsymbol{\varepsilon}, \quad (15.102)$$

where \mathbf{I} is the identity matrix. By induction, the transformation of the orbit matrix for n resolutions is

$$\mathbf{u}_{nN} = \mathbf{A}^{nN} \mathbf{u}_0 + \mathbf{D}_n \boldsymbol{\varepsilon}. \quad (15.103)$$

where

$$\mathbf{D}_n = (\mathbf{A}^{(n-1)N} + \mathbf{A}^{(n-2)N} + \dots + \mathbf{A}^N + \mathbf{I}). \quad (15.104)$$

We found in Chapter 8 that the first term on the right-hand side of Eq. 1(15.103) corresponds to bounded betatron oscillations when stability criteria are satisfied. The amplitude of the term is independent of the perturbation. Particle motion induced by the alignment error is described by the second term. The expression for \mathbf{D}_n can be simplified using the eigenvectors (Section 8.6) of the matrix \mathbf{A} : \mathbf{v}_1 and \mathbf{v}_2 . The eigenvectors form a complete set; any two-dimensional vector, including $\boldsymbol{\varepsilon}$ can be resolved into a sum of eigenvectors:

$$\boldsymbol{\varepsilon} = a_1 \mathbf{v}_1 + a_2 \mathbf{v}_2. \quad (15.105)$$

We found in Section 8.6 that the eigenvalues for a transfer matrix \mathbf{A} are

$$\lambda_1 = \exp(j\mu), \quad \lambda_2 = \exp(-j\mu). \quad (15.106)$$

where μ is the phase advance in a cell. Substituting Eq. (15.106) in Eq. (15.103), we find

$$\begin{aligned} \mathbf{D}_n \boldsymbol{\varepsilon} &= a_1 \mathbf{v}_1 \left[\exp[j(n-1)N\mu] + \exp[j(n-2)N\mu] + \dots + 1 \right] \\ &+ a_2 \mathbf{v}_2 \left[\exp[-j(n-1)N\mu] + \exp[-j(n-2)N\mu] + \dots + 1 \right], \end{aligned} \quad (15.107)$$

The sums of the geometric series can be rewritten as

Cyclotrons and Synchrotrons

$$D_n \varepsilon = \frac{\exp(jnN\mu) - 1}{\exp(jN\mu) - 1} a_1 v_1 + a \frac{\exp(-jnN\mu) - 1}{\exp(-jN\mu) - 1} a_2 v_2. \quad (15.108)$$

or, alternately,

$$D_n \varepsilon = [\sin(nN\mu/2)/\sin(n\mu/2)] \times [\exp[j(n-1)N\mu/2] a_1 v_1 + \exp[-j(n-1)N\mu/2] a_2 v_2]. \quad (15.109)$$

The second term in braces is always bounded; it has a magnitude on the order of ε . The first term in brackets determines the cumulative effect of many transitions across the alignment error. The term becomes large when the denominator approaches zero; this condition occurs when

$$\mu = 2\pi M/N, \quad (15.110)$$

where M is an integer. Equation (15.110) can be rewritten in terms of ν , the number of betatron wavelengths per revolution:

$$\nu = M. \quad (15.111)$$

This is the condition for an orbital resonance. When there is a resonance, the effects of an alignment error sum on successive revolutions. The amplitude of oscillatory motion grows with time. The motion induced by an error when $\nu \neq M$ is an oscillation superimposed on betatron and synchrotron oscillations. The amplitude of the motion can be easily estimated. For instance, in the case of a position error of magnitude ε , it is $\varepsilon/\sin(N\mu/2)$.

TABLE 15.5 Forbidden ν Values^a

Condition	Description
$\nu_r, \nu_z = M$	Magnet misalignment, error in field strength
$\nu_r, \nu_z = M/2$	Error in field index of bending magnets.
$\nu_r, \nu_z = N$ or $N/2$	Particularly strong special case of conditions 1 or 2, where N is the number of focusing cells in the circular machine.
$\nu_r, \nu_z = N'$ or $N'/2$	Another special case of 1 or 2, where N' is the number of superperiods in a machine with curved and straight sections.
$\nu_r + \nu_z = M$	Linear coupling between horizontal and vertical betatron oscillations. Induced by rotational error in a quadrupole focusing magnet.

^a M , N , and N' are integers.

Cyclotrons and Synchrotrons

An alternate view of the nature of resonant instabilities, mode coupling, is useful for general treatments of particle instabilities. The viewpoint arises from conservation of energy and the second law of thermodynamics. The second law implies that there is equipartition of energy between the various modes of oscillation of a physical system in equilibrium. In the treatment of resonant instabilities in circular accelerators, we included two modes of oscillation: (1) the revolution of particles at frequency ω_{go} and (2) betatron oscillations. There is considerable longitudinal energy associated with particle revolution and, under normal circumstances, a small amount of energy in betatron oscillations.

In a linear analysis, there is no exchange of energy between the two modes. A field error introduces a nonlinear coupling term, represented by $D_n \varepsilon$ in Eq. (15.103). This term allows energy exchange. The coupling is strong when the two modes are in resonance. The second law implies that the energy of the betatron oscillations increases. A complete nonlinear analysis predicts that the system ultimately approaches an equilibrium with a thermalized distribution of particle energy in the transverse and longitudinal directions. In an accelerator, the beam is lost on vacuum chamber walls well before this state is reached.

In a large circular accelerator, there are many elements of periodicity that can induce resonance coupling of energy to betatron oscillations. In synchrotrons, where particles are contained for long periods of time, all resonance conditions must be avoided. Resonances are categorized in terms of forbidden numbers of betatron wavelengths per revolution. The physical bases of some forbidden values are listed in Table 15.5.

Bibliography

- L. L. Alston (Ed.), **High Voltage Technology**, Oxford University Press, Oxford, 1968.
- R. Bakish, **Introduction to Electron Beam Technology**, Wiley, New York, 1962.
- A. P. Banford, **The Transport of Charged Particle Beams**, Spon, London, 1966.
- A. H. W. Beck, **Space Charge Waves and Slow Electromagnetic Waves**, Pergamon Press, London, 1958.
- M. Y. Bernard, *Particles and Fields: Fundamental Equations*, in A. Septier, Ed., **Focusing of Charged Particles, Vol. 1**, Academic, New York, 1967.
- P. Bonjour, *Numerical Methods for Computing Electrostatic and Magnetic Fields*, in A. Septier, Ed., **Applied Charged Particle Optics, Part A**, Academic, New York, 1980.
- M. Born and E. Wolf, **Principles of Optics**, Pergamon Press, Oxford, 1965.
- D. Boussard, *Focusing in Linear Accelerators*, in A. Septier, Ed., **Focusing of Charged Particles, Vol. 2**, Academic, New York, 1967.
- H. Brechner, **Superconducting Magnet Systems**, Springer-Verlag, Berlin, 1973.
- L. Brillouin, **Wave Propagation in Periodic Structures**, Dover, New York, 1953.
- G. Brewer, **Ion Propulsion - Technology and Applications**, Gordon and Breach, New York, 1970.
- H. Bruck, **Accélérateurs Circulaires de Particules**, Presses Universitaires de France, Paris, 1966.
- R. A. Carrigan, F. P. Huson, and M. Month, **Summer School on High Energy Particle Accelerators**, American Institute of Physics, New York, 1981.
- J. D. Cobine, **Gaseous Conductors**, Dover, New York, 1958.

Bibliography

R. E. Collin, **Foundations for Microwave Engineering**, McGraw-Hill, New York, 1966.

T. Collins, *Concepts in the Design of Circular Accelerators*, in **Physics of High Energy Particle Accelerators** (SLAC Summer School, 1982), American Institute of Physics, New York, 1983.

J.S. Colonias, **Particle Accelerator Design - Computer Programs**, Academic, New York, 1974.

V.E. Coslett, **Introduction to Electron Optics**, Oxford University Press, Oxford, 1950.

P. Dahl, **Introduction to Electron and Ion Optics**, Academic, New York, 1973

H.A. Enge, *Deflecting Magnets*, in A. Septier, Ed., **Focusing of Charged Particles, Vol. 2**, Academic, New York, 1967.

C.Fert and P. Durandau, *Magnetic Electron Lenses*, in A. Septier, Ed., **Focusing of Charged Particles, Vol. 1**, Academic, New York, 1967.

J.F. Francis, **High Voltage Pulse Techniques**, Air Force Office of Scientific Research, AFOSR-74-2639-5, 1974.

J. C. Francken, *Analogical Methods for Resolving Laplace's and Poisson's Equation*, in A. Septier, Ed., **Focusing of Charged Particles, Vol. 1**, Academic, New York, 1967.

A.Galejs and P. H. Rose, *Optics of Electrostatic Accelerator Tubes*, in A. Septier, Ed., *Focusing of Charged Particles, Vol. 2*, Academic, New York, 1967.

C. Germain, *Measurement of Magnetic Fields*, in A. Septier, Ed., **Focusing of Charged Particles, Vol. 1**, Academic, New York, 1967.

G. N. Glasoe and J. V. Lebacqz, **Pulse Generators**, Dover, New York, 1965.

M. Goldsmith, **Europe's Giant Accelerator, the Story of the CERN 400 GeV Proton Synchrotron**, Taylor and Francis, London, 1977.

H. Goldstein, **Classical Mechanics**, Addison-Wesley, Reading, Mass., 1950.

P. Grivet and A. Septier, **Electron Optics**, Pergamon Press, Oxford, 1972.

K. J. Hanszen and R. Lauer, *Electrostatic Lenses*, in A. Septier, Ed., **Focusing of Charged Particles, Vol. 1**, Academic, New York, 1967.

Bibliography

- E. Harting and F. H. Read, **Electrostatic Lenses**, Elsevier, Amsterdam, 1976.
- W.V. Hassenzahl, R. B. Meuser, and C. Taylor, *The Technology of Superconducting Accelerator Dipoles*, in **Physics of High Energy Particle Accelerators** (SLAC Summer School, 1982), American Institute of Physics, New York, 1983.
- P. W. Hawkes, **Electron Optics and Electron Microscopy**, Taylor and Francis, London, 1972.
- P. W. Hawkes (Ed.), **Magnetic Electron Lens Properties**, Springer-Verlag, Berlin, 1980.
- P.W. Hawkes, *Methods of Computing Optical Properties and Combating Aberrations for Low-Intensity Beams*, in A. Septier, Ed., **Applied Charged Particle Optics, Part A**, Academic, New York, 1980.
- P. W. Hawkes, **Quadrupoles in Electron Lens Design**, Academic, New York, 1970.
- P. W. Hawkes, **Quadrupole Optics**, Springer-Verlag, Berlin, 1966.
- R. Hutter, *Beams with Space-charge*, in A. Septier, Ed., **Focusing of Charged Particles, Vol. 2**, Academic, New York, 1967.
- J. D. Jackson, **Classical Electrodynamics**, Wiley, New York, 1975.
- I. M. Kapchinskii, *Dynamics in Linear Resonance Accelerators*, Atomizdat, Moscow, 1966.
- S. P. Kapitza and V. N. Melekhin, **The Microtron**, Harwood Academic, New York, 1978. (I. N. Sviatoslavsky (trans.))
- E. Keil, *Computer Programs in Accelerator Physics*, in **Physics of High Energy Particle Accelerators** (SLAC Summer -School, 1982), American Institute of Physics, New York, 1983.
- O. Klemperer and M. E. Barnett, **Electron Optics**, Cambridge University Press, London, 1971.
- A. A. Kolomensky and A. N. Lebedev, **Theory of Cyclic Accelerators** (trans. from Russian by M. Barbier), North-Holland, Amsterdam, 1966.
- R. Kollath (Ed.), **Particle Accelerators** (trans. from 2nd German edition by W. Summer), Pittman and Sons, London, 1967.
- P. M. Lapostolle and A. Septier (Eds.), **Linear Accelerators**, North Holland, Amsterdam, 1970.
- L. J. Laslett, *Strong Focusing in Circular Particle Accelerators*, in A. Septier, Ed., **Focusing of**

Bibliography

Charged Particles, Vol. 2., Academic, New York, 1967.

J. D. Lawson, **The Physics of Charged-particle Beams**, Clarendon Press, Oxford, 1977.

B. Lehnert, **Dynamics of Charged Particles**, North-Holland, Amsterdam, 1964.

A. J. Lichtenberg, **Phase Space Dynamics of Particles**, Wiley, New York, 1969.

R. Littauer, *Beam Instrumentation*, in **Physics of High-energy Particle Accelerators** (SLAC Summer School, 1982), American Institute of Physics, New York, 1983.

J. J. Livingood, **Principles of Cyclic Particle Accelerators**, Van Nostrand, Princeton, New Jersey, 1961.

J. J. Livingood, **The Optics of Dipole Magnets**, Academic, New York, 1969.

M. S. Livingston (Ed.), **The Development of High Energy Particle Accelerators**, Dover, New York, 1966.

M. S. Livingston, **High Energy Accelerators**, Interscience, New York, 1954.

M. S. Livingston, **Particle Accelerators, A Brief History**, Harvard University Press, Cambridge, Mass., 1969.

M. S. Livingston and J. P. Blewett, **Particle Accelerators**, McGraw-Hill, New York, 1962.

G. A. Loew and R. Talman, *Elementary Principles of Linear Accelerators*, in **Physics of High Energy Particle Accelerators** (SLAC Summer School, 1982), American Institute of Physics, New York, 1983.

W. B. Mann, **The Cyclotron**, Methuen, London, 1953.

J. W. Mayer, L. Eriksson, and J. A. Davies, **Ion Implantation in Semiconductors**, Academic, New York, 1970.

N. W. McLachlan, **Theory and Application of Mathieu Functions**, Oxford University Press, Oxford, 1947.

A. H. Maleka, **Electron-beam Welding - Principles and Practice**, McGraw-Hill, New York, 1971.

R. B. Miller, **Intense Charged Particle Beams**, Plenum Press, New York, 1982.

Bibliography

- M. Month (Ed.), **Physics of High Energy Particle Accelerators** (SLAC Summer School, 1982), American Institute of Physics, New York, 1983.
- R. B. Neal (Ed.), **The Stanford Two-mile Accelerator**, Benjamin, Reading, Mass., 1968.
- T. J. Northrup, **The Adiabatic Motion of Charged Particles**, Interscience, New York, 1963.
- H. Patterson, **Accelerator Health Physics**, Academic, New York, 1973.
- E. Perisco, E. Ferrari, and, S. E. Segre, **Principles of Particle Accelerators**, Benjamin, New York, 1968.
- J. R. Pierce, **Theory and Design of Electron Beams**, Van Nostrand, Princeton, New Jersey 1954.
- D. Potter, **Computational Physics**, Wiley-Interscience, New York, 1973.
- R. E. Rand, **Recirculating Electron Accelerators**, Harwood Academic, New York, 1984.
- S. Ramo, J. R. Whinnery, and T. Van Duzer, **Fields and Waves in Communications Electronics**, Wiley, New York, 1965.
- E. Regenstreif, *Focusing with Quadrupoles, Doublets and Triplets*, in A. Septier, Ed., **Focusing of Charged Particles, Vol, 1**, Academic, New York, 1967.
- J. Rosenblatt, **Particle Accelerators**, Methuen, London, 1968.
- W. Scharf, **Particle Accelerators and Their Uses**, Harwood Academic, New York. 1985.
- S. Schiller, U. Heisig, and S. Panzer, **Electron Beam Technology**, Wiley, New York, 1982.
- R.W. Southwell, **Relaxation Methods in Theoretical Physics**, Oxford University Press, Oxford, 1946.
- A. Septier (Ed.), **Applied Charged Particle Optics, Part A**, Academic, New York, 1980.
- A. Septier (Ed.), **Applied Charged Particle Optics, Part B**, Academic, New York, 1980,
- A. Septier (Ed.), **Applied Charged Particle Optics, Part C, Very-High Density Beams**, Academic, New York, 1983.
- A. Septier (Ed.). **Focusing of Charged Particles**, Academic, New York, 1967.

Bibliography

- J. C. Slater, **Microwave Electronics**, Van Nostrand, Princeton, New Jersey, 1950.
- K. G. Steffen, **High Energy Beam Optics**, Wiley-Interscience, New York, 1965.
- E. Stuhlinger, **Ion Propulsion for Space Flight**, McGraw-Mill, New York, 1964.
- P. Sturrock, **Static and Dynamic Electron Optics**, Cambridge University Press, London, 1955.
- M. Tigner and H. Padamsee, *Superconducting Microwave Cavities in Accelerators for Particle Physics*, in **Physics of High Energy Particle Accelerators** (SLAC Summer School, 1982), American Institute of Physics, New York, 1983.
- A. D. Vlasov, **Theory of Linear Accelerators**, Atomizdat, Moscow, 1965.
- C. Weber, *Numerical Solutions of Laplace's and Poisson's Equations and the Calculation of Electron Trajectories and Electron Beams*, in A. Septier, Ed., **Focusing of Charged Particles, Vol. 1**, Academic, New York, 1967.
- R. G. Wilson and G. R. Brewer, **Ion Beams with Applications to Ion Implantation**, Wiley, New York, 1973.
- H. Wollnik, *Electrostatic Prisms*, in A. Septier, Ed., **Focusing of Charged Particles, Vol. 2**, Academic, New York, 1967.
- H. Wollnik, *Mass Spectrographs and Isotope Separators*, in A. Septier, Ed., **Applied Charged Particle Optics, Part B**, Academic, New York, 1980.
- O. C. Zienkiewicz, **The Finite Element Method in Engineering Science**, McGraw-Hill, New York, 1971.
- J.F. Ziegler, **New Uses of Ion Accelerators**, Plenum, New York, 1975.
- V. K. Zworykin, G. A. Morton, E. G. Ramberg, J. Hillier, and A. W. Vance, **Electron Optics and the Electron Microscope**, Wiley, New York, 1945.

Index

- Aberrations, lens, 132
- Acceleration column, electrostatic, 161, 227
 - breakdown in vacuum, 228f
 - maximizing breakdown voltage, 231
- Acceleration gap, electrostatic focusing, 121, 125, 172
- Accelerator:
 - AGS (alternating gradient synchrotron), 503
 - Alvarez, 456f
 - AVF (azimuthally varying field) cyclotron, 501, 524f
 - betatron, 326f
 - Cockcroft-Walton, 210, 221
 - coreless linear induction, 317f
 - coupled cavity, 459f
 - cyclotron, 504f
 - drift tube linac (DTL), 456f
 - electrostatic, 196f
 - high energy, listing, 542
 - linear, RF, 437f
 - electron, 440f
 - ion, 452f
 - linear induction, 283f
 - pulsed power, 258f
 - racetrack microtron, 493f
 - radio-frequency quadrupole (RFQ), 482f
 - recirculating linear induction, 328f
 - separated function synchrotron, 503, 531f
 - separated sector; cyclotron, 501, 520f
 - side-coupled linac, 465, 469
 - spiral cyclotron, 502, 518f
 - strong-focusing synchrotron, 503
 - superconducting. cyclotron, 502
 - synchrocyclotron, 502, 523f
 - synchrotron, 502, 531f
 - uniform-field cyclotron, 501, 504f
 - Van de Graaff, 221f
 - weak focusing synchrotron, 503, 534
 - Wideroe, 453
- Acceptance:
 - of aperture, 140, 142
 - of, focusing-system, 129, 140f
 - of linear focusing system, 141f
 - longitudinal, 420f
 - of strong focusing system, 551
 - of weak focusing system, 551
- Alpha.particle, properties, 10
- Ampere, definition, 27
- Analog, electrostatic. @potential, 59f
- Angular, momentum, canonical, 126, 154
 - conservation, 126, 152f
- Apparent accelerator length, 433f
- Applications, accelerator, 6
- Archimedean spiral, 519
- ATA accelerator:
 - cavity. geometry, 289, 290
 - parameters, 288
- Atomic mass number, A, 9
- Atomic number, Z, 9
- Ballistic orbits, definition, 116
- Barium titanate, 85
- Beam, charged particle, 2
 - breakup instability, 445f
 - bunching, 423, 445
 - confinement, 109
 - cooling, 536

Index

- current measurement, 276f
- focus, 110
- generation process, 2f
- laminar, definition, 113
- matching, to focusing system, definition, 141
- position measurement, 278
- Bessel equation, 369
- Bessel functions, 369f
- Beta-lambda linac, 456
- Beta-lambda/2 linac, 456
- Beta, relativistic factor, 18, 24
- Betatron, 326f
 - acceleration cycle, 333, 352f
 - betatron, condition, 333
 - betatron oscillations, 336, 342f
 - comparison to linear induction accelerator, 328f
 - equivalent circuit, 348f
 - extraction from, 345f
 - field biasing, 354f
 - flux biasing, 354f
 - geometry, 328
 - high current:
 - advantages, 327
 - methods of achieving, 346f
 - injection into, 334f, 343f
 - instantaneous circle, 334f
 - magnetic peeler, 345
 - mapets, 348
 - main orbit, 332
 - maximum beam energy:
 - electrons, 330
 - ions, 331f
 - orbit contraction coils, 345
 - principle of operation, 327f
- Betatron oscillations, 138, 342
 - constant energy, 145f
 - radial and axial frequencies, 150
 - reversible compressions, 336f
 - orbital stability, 150
 - variable energy, 342
- Betatron wavelength, 138
 - in FD quadrupole channel, 193, 195
- Bevatron, 547
- Bifrignence, 79
- Biot and Savart, law of, 28, 68
- Blumlein line, 250f
 - analysis of operation, 251
 - circuit, 250f
 - geometry, 250
 - properties, 253
- Breakdown:
 - spark:
 - condition for, in gas, 216
 - electronegative gases, effect of, 218
 - in gases, 213f
 - in oil and water, 212
 - Paschen's law, 217
 - self-sustaining discharge, conditions, 216
 - spark parameters, gases, 218
 - vacuum, 227f
 - breakdown levels, effect of pulselength, 229f
 - breakdown voltage, methods to increase, 230f
 - conditioning of metal surfaces, effect, 229
 - effect of beam, 231
 - effect of exposed insulators, 229
 - effect of surface whiskers, 227f
 - electron multipactoring, 479f
 - exposed insulators, breakdown levels, 231
 - factors affecting, 228f
 - Kilpatrick limit, RF voltage, 482
 - with RF voltage, 478f
- Brillouin diagram, 407
- Busch theorem, 152
- Capacitance:
 - coaxial capacitor, 200
 - parallel plates, 199
 - transmission line, 249
- Capacitor, 199
 - coaxial, 200f

Index

- energy transfer between, 259f
- impedance, 361
- parallel plate, 3 If, 85
- in pulsed power circuit, 233
- stored electrostatic energy density, 97f
- stored energy, 200
- Cathode:
 - cold, 229
 - effect of plasma closure, 229
 - immersed, 156
- Central orbit, 128
- Characteristic impedance:
 - coaxial transmission line, 241, 246
- Guillemin network, 255f
 - LRC circuit, 235
 - transmission line equivalent PFN, 254
 - transmission lines, 241
- Charge density, 33, 64
- Charge layer, 65
- Chromaticity, 168
- Clock, photon, 16, 19
- Cockcroft-Walton accelerator, 210f, 221
- Coercive force, 93
- Coherence, beam, 2
- Collider, 504, 540f
 - advantages, 541f
 - available reaction energy, 541
 - lumiosity, 543
 - particle dynamics in, 540
- Complex conjugate, 359
- Complex exponential notation:
 - relation to trigonometric functions, 358
 - theory, 357f
- Confinement system, magnetic, 68
- Constancy, speed of light, 22
- Coordinates, cylindrical, 40f
- Coordinate transformations, 13f
- Corona discharge, 220
- Coulomb's law, 27
- Curl operator, 49f
- Cartesian coordinates, 50
- Current, 27
 - Current density, 33, 60
 - Current loop, magnetic fields of, 72f
 - Current measurement, see Pulsed current measurement
 - Current sheet, 68
 - Cutoff frequency, waveguide, 387, 390
 - CVR (current viewing resistor), 276f
 - configurations, 277
 - Cyclotron, 501
 - AVF:
 - advantages, 527
 - energy limits, 527
 - nature of focusing forces, 526
 - radial field variations, 524f
 - AVF focusing, 513f. See also Focusing by
 - azimuthally varying fields
 - azimuthally varying field, 501
 - beam extraction, 508
 - dees, 506
 - separated sector, 501
 - advantages, 527f
 - spiral, 502
 - superconducting, 502
 - trim coils, 525f
 - uniform-field:
 - magnetic field, 506f
 - maximum beam energy, 51 If
 - phase dynamics, 509f
 - principles, 501, 504f
 - transverse focusing, 506f
- Delta function, 33
- Demagnetization curve, 105
- Derivative:
 - first, finite difference form, 53
 - second, finite difference form, 54
- Deuteron, properties, 10
- Diamagnetism, 39
- Dielectric constant, relative, 79
 - plasma, 82
 - water, 80
- Dielectric materials, 64, 77f
 - accelerator applications, 77

Index

- properties, 78f
- saturation, 79
- Dielectric strength, 212
- Diode, 198
 - pulsed power, 258
- Dirichlet boundary condition, 56
- Dispersion, in waveguide, 387
- Dispersion relationship, 389
- Displacement current, 37, 39f
- Displacement current density, expression, 39
- Displacement vector, D , 76, 80f
 - boundary conditions, 81, 83f
- Distribution, particle, 140
 - modification by acceleration gap, 427
- Divergence equation, 46
- Divergence operator, 47
- Divergence theorem, 47
- Domains, magnetic, 90
- Drift tube, 453
- Dynamics, particle, 8f
- EAGLE, pulsed power generator, 259, 261
- Eddy current, 291
- Edge focusing, 132f
- Eigenvalues, 184f
 - of 2×2 matrix, 185
- Eigenvectors, 184f
 - of 2×2 matrix, 185
- Elastic sheet, electrostatic potential analog, 59
- Electric field, 29f, 45f
 - between parallel plates, 33
 - boundary conditions on dielectric material, 81, 83f
 - boundary conditions on metal surface, 51
 - in charged cylinder, 64f
 - energy density, 97f
 - minimization in electrostatic accelerator, 223f
 - paraxial approximation, 111f
 - properties, 52
- Electrodes, quadrupole field, 62
- Electrolytic tank, electrostatic potential analog, 60f
- Electromagnetic oscillations, 40
- Electron, properties, 10
- Electron capture, 432
- Electron multiplication, in gases, 214f, 219
- Electron volt, eV, 9f, 23
- Electrostatic energy, storage, 85
- Elliptic integrals, 73f
 - series approximations, 74
- Equipotential surface., 52
- Energy:
 - kinetic:
 - Newtonian, 12f, 23
 - relativistic, 23
 - potential, 13
 - relativistic, 22
 - rest, 23
- Envelope, beam, 110, 154
- Equipotential shields, 225f
- Eulerian difference method, 115
- Extractor, charged, particle, 121
- Faraday rotation, 291f
- Faraday's law, 37, 38f
- FD focusing channel, 118f, 192f
- Ferrite, 287, 293, 294, 299
- Ferromagnetic materials, 90f
 - accelerator applications, 77
 - applications to magnetic circuits, 102
 - boundary conditions, 95f
 - eddy currents, effects, 291f
 - ferrite, properties, 293f, 299
 - hysteresis curve, 91f
 - Metglas, properties, 293f, 299
 - properties, 90f
 - relative permeability, 90
 - saturation, 90, 91
 - saturation wave, 295
 - silicon steel, properties, 293f, 299
 - skin depth, 291
 - terminology, 93

Index

- time-dependent, properties, 291f
- FFAG accelerator, 513
- Field biasing, betatron, 354f
- Field description, advantages, 31
- Field emission, 227
 - enhancement by surface whiskers, 227f
 - Fowler-Nordheim equation, 227
- Field equations, static, 46
- Field index, 148
 - expressions for, 148
 - in isochronous cyclotron, 525
- Field lines, 46
 - approximation, 110f
 - focusing properties, 113f
 - magnetic:
 - relation to magnetic potential and vector potential, 71
 - relation to stream function, 72
- Finite difference calculations, 53
 - accuracy, 159f
 - Eulerian method, II 5, 15 9
 - particle orbits, 157f
 - particle orbits in periodic focusing channel, 179f
 - time-centered method, 159
 - two-step method, 159f
- Flutter, AVF focusing, 514
- Flux, magnetic, 38, 102
- Flux biasing, betatron, 354f
- Flux forcing, 305f, 350
- Flux function, 153
 - relation to vector potential and stream function, 154
- FNAL accelerator (Tevatron), 536f
- f-number, 117
- Focal length, 116
 - relation to transfer matrix, 173
 - systems with curved axes, 130
- Focusing, radial, in uniform magnetic field, 146
- Focusing by azimuthally varying fields, 513f
 - in AVF cyclotron, 526
 - flutter, 514
 - flutter amplitude, 514
 - flutter function, 514
 - hills and valleys, definition, 514
 - modulation function, 514
 - nu, vertical and horizontal, 517f
 - particle orbits, 514f
 - sector, definition, 514
 - separated sector magnets, 521f
 - separated sector magnets with spiral boundaries, 521
 - spiral pole boundaries, effect, 518
 - Thomas focusing, 514f
 - transfer matrices, 517f
- Focusing cell, definition, 179
- Focusing channels, periodic, 165f
 - FODO, 533
 - quadrupole, stability condition, 188, 192f
 - quadrupoles, 187f, 550f
 - stability properties, 183f
- Focusing force, average in a periodic system, 139
- Focusing lattice, 532
- Foil focusing, 124
- Force, 11, 22
 - centrifugal, 41
 - between charges, 27
 - Coriolis, 42
 - electric, 26f, 30
 - magnetic, 26f, 30f
 - virtual, 41
- Fowler-Nordheim equation, 227
- Frames of reference, 13
- Frequency domain, 198, 240
- Fringing flux, 102
- Gamma, relativistic factor, 18
- Gap, vacuum, effect in magnetic circuit, 100
- Gaussian optics, 108
- Gradient, definition, 13
- Grading, voltage, 223f
- Grading rings:

Index

- effect on vacuum insulation, 227f, 230, 231, 232
 - electrostatic focusing by, 161
 - electrostatic potential variations, 163f
- Grid focusing, 124
- Group velocity, 387, 449
 - in coupled cavities, 466
- Guillemin network, 255f
 - choice of circuit elements, 257
 - properties, 257
- Gyrocenter, 44
- Gyrofrequency, 44
- Gyroradius, 44
 - in cyclotron, 506
- Hamiltonian dynamics, 154
- Harmonic oscillator, damped, solution, 359f
- Helmholtz coils, 75
- Hysteresis, 93
- Hysteresis curve:
 - examples, 94
 - ferromagnetic materials, 91f
 - measurement, 91
 - saturation, 92f
- Image:
 - charged particle, 110
 - definition, 117
 - formation, equations, 119, 175f
 - intensifier, 110
- Image plane, 117
- Image space, 116
- Impedance, 360
 - capacitor, 361
 - combinations, 362
 - inductor, 361
 - resistor, 360
 - transformation on transmission line, 383
- Inductance:
 - coaxial inductor, 201
 - solenoid inductor, 202
 - transmission line, 249
- Induction, magnetic, 37, 39
- Inductive isolation, 283
- Inductive switching, 263f
 - advantages, 263
 - circuit analysis, 263f
 - circuit design, 264, 266
 - constraints, power compression, 264f
 - for high power transmission line, 266
 - power compression, 264f
 - pulse shaping, 267
- Inductor, 199
 - coaxial, 201
 - in energy storage circuit, 236
 - impedance, 361
 - solenoid, 202
 - stored energy, 200
- Inertial frame, 15
- Instability:
 - orbital, 150
 - in FD quadrupole channel, 188f, 192f
 - in separated sector magnets, 521f
 - in strong focusing system, 554
 - in thin lens array, 182f
 - resonance, 143f
 - in circular accelerator with FD focusing, 195
 - conditions for, 145
 - models for, 144
- Insulation, 211f
 - vacuum, 227f
 - optimization, 229
- Insulator:
 - gas, properties, 213
 - high voltage vacuum, 85f
 - properties of some solids and liquids, 212
 - pulsed behavior, 212
 - self-healing, 213
 - transformer oil, properties, fast pulse, 212
 - water, properties, fast pulse, 212
- Integrator, passive, 203f
- Invariance, coordinate transformation, 15
- Ion, properties, 9

Index

- Irises, in slow wave structures, 394
 - Iris-loaded waveguide, see slow wave structure
 - ISR (Intersecting Storage Ring), 539

 - KEK 2.5 GeV accelerator, 442f
 - Kerr effect, 281
 - Kilpatrick limit, 482
 - Klystron, 376

 - Ladder network, 210f
 - advantages, 211
 - circuit, 210
 - LAMF accelerator, 465, 468
 - Laminar beam, 113, 140, 155
 - Laplace equation, 50f
 - analog solutions, 58f
 - cylindrical coordinates, 57
 - with dielectrics, 81
 - finite difference formulation, 53f
 - cylindrical coordinates, 58
 - numerical solution with dielectrics, 81
 - numerical solutions, 53f
 - Laplacian operator, 50
 - Laser, electron-beam-controlled discharge, 21
 - Law, relativistic velocity addition, 22
 - Laws of motion:
 - Cartesian coordinates, 12
 - cylindrical coordinates, 40
 - Newton's first, 11
 - Newton's second, 11
 - LC generator, 238f
 - Leakage current, 285
 - in ferrite core induction accelerator, 294f
 - in laminated core, 298
 - measurement, 298f
 - Leakage flux, 102
 - Length, apparent, 20
 - Lens, charged particle, 108f
 - determination of properties, 119
 - einzel, 124
 - electrostatic, unipotential, 119, 124
 - electrostatic aperture:
 - focal length, 121
 - properties, 119f
 - electrostatic immersion, 58, 121f
 - electric fields, 122
 - focal length, 124
 - particle orbits, 123, 164
 - potential variation, 164
 - transfer matrix, 172f
 - electrostatic quadrupole, 136
 - facet, 60
 - inclined sector magnet boundary, 132f
 - magnetic quadrupole, 134f
 - doublet and triplet, 176f
 - focal lengths, 135
 - particle orbits, 135
 - magnetic sector, 127f
 - power, 117
 - properties, 115f
 - solenoidal magnetic, 125f
 - focal length, 127
 - particle orbits, 126f
 - thick, definition, 116
 - thin:
 - definition, 115, 116
 - transfer matrix, 168
 - toroidal field sector, 131f
- Linear accelerator:
 - induction, 283f
 - accelerating gradient:
 - comparison with and without ferromagnetic cores, 323f
 - expressions, 315f
 - factors affecting, 316f
 - ATA accelerator, 288f
 - cavity:
 - equivalent circuit, 286
 - principles of operation, 284, 286
 - comparison with betatron, 283, 328f
 - compensation circuits, 31 If
 - coreless:

Index

- limitations, 323
- principles of operation, 319f
- coreless geometries, 317
- core reset, 307f
- core saturation, problems, 304
- damping resistor, role of, 307
- electric field distribution in cavity, 313f
- ferrite core cavity, 294f
- flux forcing, 305
- injector configuration, 302
- laminated cores, 297
- leakage current, 285, 295, 298
- longitudinal beam confinement:
 - electrons, 435f
 - ions, 427f
- longitudinal core stacking, 302
- longitudinal dynamics, 426f
- radial core stacking, 302f, 306f
- recirculating, 328f
- relationship to electrostatic accelerator, 284f
- reset circuit:
 - ferrite core cavity driven by Blumlein line, 309f
 - long pulse accelerator, 308
 - properties, 307
 - series configuration, 286, 287
 - volt-second product, 287
- RF:
 - choice of waveguide, 406f
 - energy spread, 426
 - individually phased cavities, particle dynamics, 411f
 - individually phased cavity array, 398, 456
 - injection into, 423
 - Kilpatrick limit, 482
 - micropulsewidth, 425
 - multipactoring, 479
 - radio-frequency quadrupole (RFQ), 482f
 - representation of accelerating field, 416
 - resolution of electric fields into travelling waves, 414f
 - shunt impedance, definition, 452
 - vacuum breakdown in, 478f
- Linear accelerators, advantages, 437
- Linear electron accelerator, RF, 440f
 - beam breakup instability, 445f, 447
 - energy flow, 449f
 - frequency equation, 447f
 - geometry, 440f, 451f
 - injection into, 445
 - optimizing for maximum beam energy, 450f
 - properties, 440f
 - pulse shortening, 445f
 - radial defocusing by RF fields, 478
 - regenerative beam breakup instability, 446
 - transverse instability, 445f
- Linear focusing force, properties, 138
- Linear ion accelerator, 452f
 - Alvarez linac, 456f
 - beta-lambda structure, 456
 - beta-lambda/2 structure, 456
 - comparison with electron accelerator, 452
 - coupled cavity, 459f
 - disk and washer structure, 466, 473
 - drift tube linac, 456f
 - features, 459
 - gap coefficient, 475
 - post-couplers in DTL, 459
 - radial defocusing by RF fields, 476
 - resonant cavities in, 455
 - side-coupled linac, 465, 469
 - transit-time factor, 473f
 - Wideroe configuration, 453f
- Linear optics, 108
- Lorentz contraction, 18f
- Lorentz force law, 3, 31
- LRC circuit:
 - equations, 233f
 - power loss, resonant circuit, 363f
 - Q parameter, 364f
 - resonance, 362f
 - resonance width, 363, 365
 - solutions:

Index

- critically damped, 235
- overdamped, 235
- underdamped, 235
- L/R time, 204
- Luminosity, 543
- Magnetic circuits, 99f
 - permanent, 103f
- Magnetic core:
 - betatrons, 348f
 - construction, 291
 - electric field distribution, 299f
 - energy losses, 99
 - ferrite, properties, 287
 - flux forcing, 305f
 - in inductive accelerator, 287
 - in inductive switches, 263f
 - laminated core construction, 297
 - laminated cores, time-dependent properties, 297f
 - in magnetic circuit, 101
 - reset, 264, 307f
 - saturation, problems, 303f
 - saturation wave, 295
- Magnetic field, 30f, 45f, 93
 - boundary conditions, ferromagnetic materials, 95f
 - of current loop, 74f
 - electro-optic measurements, 281f
 - energy density, 97f
 - calculated from hysteresis curve, 98f
 - examples, 67f
 - with gradient, properties, 148
 - of Helmholtz coils, 75
 - near current-carrying wire, 67
 - near two current carrying wires, 71
 - paraxial approximation, 112f
 - sector, 127f
 - sector with gradient, transfer matrix, 170
 - solenoid, 68f
 - in torus, 68f
- Magnetic intensity, H, 76, 88f, 93
- Magnetic materials, 87f
 - hard, definition, 93
 - properties, 87f
 - soft, definition, 93
- Magnetic mirror, 112f, 147f
 - properties of field in, 148f
- Magnetic moment, 87f
 - classical value, 87
 - quantum mechanical value, 88
- Magnetic poles, 95f
 - determination of shape, 148
 - North-South convention, 96
 - saturation effects, 96
- Magnetization curve, virgin, 92
- Magnetomotive force, 102
- Magnets:
 - AGS (alternating gradient synchrotron), 53
 - betatron, 348f
 - cyclotron, 506, 514
 - dipole, 532f
 - quadrupole, 532f
 - sextupole, 532f
 - synchrotron, 532f
 - superconducting, 537
- Magnification, by lens, 118
- MAMI accelerator, 494, 496
- Marx generator, 237f
- Mass, 10f
 - relativistic, 22
- Mathieu equations, 484
- Matrix, transfer, 165f
 - of AVF system, 517f
 - of AVF system with spiral boundaries, 518
 - of circular accelerator with alignment error, 552f
 - combining optical elements, 173f
 - determinant, 172
 - of drift space, 169
 - eigenvectors and eigenvalues, 184f
 - of immersion lens, 172
 - inverse, 171f
 - multiplication, rules of, 174

Index

- operations, 167
- orbital stability condition, 186
- properties of, 167f, 172
- of quadrupole channel, 188, 192
- of quadrupole doublet, 177f
- of quadrupole lens, 166f
- of quadrupole triplet, 179
- raising to power, 183f
- relation to phase advance, 186
- relation to principal planes and focal lengths of lens, 173
- of sector magnet with gradient, 170f
- of thin lens, 168
- trace, 184
- Maxwell equations, 33f
 - electromagnetic form, vacuum, 368
 - listing, 34
 - static form, 46
- Mean free path, for collisions, 214
- Mechanics, Newtonian, 10f
- Mesh, finite difference, 53, 55
- Microbursts, 229
- Microtron, see Racetrack microtron
- Modulator, pulsed power, see Pulsed power generator
- Momentum:
 - Newtonian, 11
 - relativistic, 22
- Multipactoring, 479f
- Necktie diagram, 192, 194
- Negative lens effect, 121
- Neptune C, pulsed power generator, 259, 260
- Neumann boundary condition, 56, 58
- Nu, 142f
 - for AVF cyclotron, 527
 - for AVF focusing system, 517f
 - for AVF focusing system with spiral boundaries, 519
- boundaries, 519
- definition, 143
- forbidden values, 533, 554f
 - for separated sector magnets with spiral boundaries, 521
- Numerical solutions:
 - first order differential equation, 158f
 - Laplace equation, 53f
 - particle orbits, 157f
 - particle orbits in acceleration column, 161
 - particle orbits in immersion lens, 164
 - second order differential equation, 157f
- Object plane, 117
- Object space, 116
- Oil, transformer:
 - in coaxial transmission line, 250
 - insulation properties, 212
- Orange spectrometer, 131
- Orbit, particle:
 - in AVF focusing system, 514f
 - constant magnetic field, 43f, 146
 - numerical solutions, 157f
 - in quadrupole channel, 189f
 - reversible compression, 337f
 - in RF quadrupole field, 484f
 - in separated sector cyclotron, 529
 - in thin lens array, 181f
- Orthogonality, of eigenvectors, 184
- Paramagnetic materials, 88, 90
- Paraxial approximation, basis, 110
- Paraxial ray equation, 151, 154f
 - complete relativistic form, 156
 - non-relativistic forms, 157
 - validity conditions, 155
- Particle, properties, 9f
- Paschen law, 217f
- Peaking capacitor circuit, 259f
- Periodic focusing, 165f
 - choice of phase advance, 191
 - orbit solutions, 179f
 - stability condition, 186
 - stability properties, 183f
- Permanence, magnetic, 102

Index

- Permanent magnets, 103f
 - energy product, 106
 - examples of calculations, 107
 - load line, 107
 - material properties, 104
 - operating point, 105f
 - permanence coefficient, 107
- Permeability, relative, 88f
 - small signal value, 91
- Phase, particle, definition, 410f, 414
- Phase advance:
 - choice of optimum, 191
 - definition, 181
 - relation to transfer matrix, 186
- Phase dynamics, 408f
 - asymptotic-phase, electron accelerator, 445
 - compression of phase oscillations, 424
 - effective longitudinal force, 419
 - electron capture, 432, 445
 - limits of phase oscillations, 419
 - linear, accelerator, electrons, 430f
 - linear induction accelerator:
 - electrons, 435f
 - ions, 426f
 - longitudinal acceptance, 420f
 - longitudinal potential diagram, 420f
 - in racetrack microtron, 498f
 - relation between kinetic energy error and phase, 424
 - relativistic particles, 430f
 - in synchrotron, 544f
 - trapping particles in RF buckets, 422
 - in uniform-field cyclotron, 509
- Phase equations, 414f
 - applications, 408
 - approximation:
 - slowly varying vs, 418, 419
 - small amplitude, 418
 - small amplitude, 424f
 - general form, 417
 - relativistic limit, 430, 432
 - for synchrotron, 549
 - for uniform-field cyclotron, 511
- Phase oscillation frequency, 418
- Phase space, 140
 - conservation of phase area, 339, 341
 - orbits, reversible compression, 339
 - relativistic particles, 343
- Phase stability, 410f
 - condition:
 - linear accelerator, 413
 - synchrotron, 550
- PIGMI accelerator, 467
- Pion, 18
- Planck constant, 88
- Plasma, dielectric constant, 82
- Plasma closure, cold cathode, 229
- Plasma source, inductively coupled, 38, 39
- Pockels effect, 281
- Poisson equation, 65f
 - numerical solution, 66f
- Polar molecules, 77f
- Potential:
 - absolute, 36, 155
 - electrostatic, 34f, 50
 - in charge cylinder, 66
 - definition, 36
 - expressions, 36, 37
 - magnetic, 53, 70f
 - analogy with electrostatics for ferromagnetic poles, 95
 - relation to field lines, 71
 - vector, 34f, 70f
 - analogy with field lines, 70
 - of current loop, 72f
 - definition, 37
 - expressions, 37
 - relation to flux function, 154
 - of two current-carrying wires, 71
- Power compression, 259f
 - role of peaking capacitor circuit, 260f
- Power supplies, high voltage, 204f
 - circuit, half-wave rectifier, 209
 - ladder network, 210f

Index

- ripple, 209
- Precession, orbit, 150
- Primary, transformer, 204
 - inductance, 205
- Principal plane, 116
 - relation to transfer matrix, 173
 - in system with curved axes, 130
- Proton, properties, 10
- Pulsed current measurement:
 - current viewing resistor (CVR), 276f
 - electro-optical, 281f
 - magnetic pickup loops, 278f
 - Rogowski loop, 279f
- Pulsed power generator, 231f
 - accelerator applications, 232
 - Blumlein line, 250f
 - characteristic impedance, 235
 - critically damped LRC circuit, properties, 235
 - diagnostics on, 267f
 - impulse generators, 236f
 - inductive energy storage, 236
- LC generator:
 - circuit, 238f
 - properties, 239f
- Marx generator:
 - circuit, 237
 - properties, 238
- matching condition to load, 235
- peaking capacitor circuit, 260
- power compression cycle, 258f
- properties, 231
- pulse-forming-network, 254f
- pulse shaping by saturable core inductors, 267
- risetime of current and power, 204
- role of saturable core inductor switches, 263
- series transmission line circuits, 250f
- simple model, 202
- switching by saturable core inductors, 266
- transmission line:
 - circuit, 248
 - properties, 241f
- Pulsed voltage measurement, 270f
 - balanced divider, 273
 - capacitive divider, 273
 - compensated, 276
 - capacitive pickup, 275f
 - compensated divider with water resistor, 273f
 - inductive correction with magnetic pickup loop, 278f
 - inductive divider, 273
 - limitations, 267f
 - resistive divider:
 - compensation, 272f
 - sources of error, 271f
- Pulse-forming-network, 254f
 - characteristic impedance, 254
 - Guillemin network, 255f
 - transmission line equivalent circuit, 254
- Q parameter:
 - combinations, 379
 - cylindrical cavity, 373
 - definition, 364
 - resonant circuit, 365
- Quadrupole field:
 - electrostatic, 61f
 - electrostatic potential, 62
 - magnetic, 96
- Quadrupole focusing channel, 187
 - betatron wavelength, 193, 195
 - choice of phase advance, 191
 - resonance instabilities in circular accelerator, 194f
 - stability condition, 188, 192f
- Quadrupole lens:
 - doublet, 176f
 - transfer matrix, 177
 - approximate form, 178
 - magnetic, 134
 - radio-frequency (RF), 483f

Index

- transfer matrix, 166
 - approximate form, 178
- triplet, 178
 - transfer matrix, 179
- Racetrack microtron, 493f
 - advantages 493
 - double-sided microtron (DSM), 498f
 - injection into, 494f
 - geometry, 493f
 - problems of focusing and beam breakup
- instability, 497f
 - spatial separation between orbits, 497
 - synchronous particle condition, 495f
- Radio-frequency quadrupole accelerator (RFQ), 482f
 - dipole mode, 493
 - electric fields in, 487
 - electrode design, 490f
 - electromagnetic modes in, 492f
 - electrostatic approximation, 483
 - electrostatic potential, expression for, 490
 - geometry, 486, 491, 492
 - ion injection application, 482f
 - limit on accelerating gradient, 490
 - manifold, 493
 - motion of synchronous particle, 487f
 - transverse focusing in, 483f, 489f
- RC time, 203
- Rectifier, half-wave, 209
- Relativity, special, 15f
 - postulates of, 15f
- Remanence flux, 93
 - magnetic, 102
- Residuals, method of successive overrelaxation, 55
- Resistivity, volume, 60
- Resistor, 198f
 - impedance, 360
 - power dissipation, 199
- Resonance, 363
- Resonant accelerators, properties, 356
- Resonant cavity, 362
 - analogy with quarter wave line, 384
 - arrays for particle acceleration, 455f
 - comparison with induction linear
- accelerator cavity, 367
 - coupled array, 459f
 - cylindrical, 367f, 371f
 - disk and washer structure, 466, 473
 - electric and magnetic coupling between
- cavities, 460
 - high order modes, effect, 373f
 - inductive isolation in, 362f
 - lumped circuit analogy, 362f
 - matching power input, 380, 385
 - for particle acceleration, 455
 - power exchange, 376, 385
 - power losses, 363f, 373
 - Q parameter, 373
 - re-entrant, 365f
 - resonance width, 365, 373
 - resonant modes, 367f, 371f
 - role in RF accelerators, 454
 - side coupled cavities, 469
 - stored energy, 373
 - transformer properties, 377
- Resonant circuits, 362f
- Resonant modes, 367f
 - of array of coupled cavities, 462f
 - degeneracy, 376
 - nomenclature, 371
 - pi mode, coupled cavities, 464
 - pi/2 mode, coupled cavities, 466f
 - of seven coupled cavities, 464
 - TE vs. TM, 391
 - TE₁₁, 393
 - TE₁₁₁, 374f
 - TEM, 387f, 399f
 - TE₂₁₀, in RFQ, 493
 - TM₁₀, 388, 390f
 - TM_{n0}, dispersion relationship, 400
 - TM₀₁₀, cylindrical cavity, 370f, 372, 373
 - TM₀₁₀, in beta-lambda and beta-lambda/2

Index

- structures, 456
 - TM020, cylindrical cavity, 370, 372
 - TM0n0, cylindrical cavity, 370, 371
 - TM110, 445f
 - of two coupled cavities, 460f
- Rest energy, 9
- Rest frame, 13
- Rest mass, 11
- Reversible compression, particle orbits:
 - of phase oscillations, 424f
 - properties, 338f
 - relativistic, 343
- RF bucket, 422
- Rogowski loop, 279f
 - geometry, 280
 - properties, 281
 - sensitivity, 280, 281
 - theory, 279f
- Rogowski profile, 219f
- Saturation induction, 93
- Saturation wave, in magnetic core, 295f
- Secondary, transformer, 204
- Secondary emission coefficient, 215, 479
- Sector magnet, 127f
 - focal properties, 45 degrees, 498f
 - horizontal direction, definition, 128
 - with inclined boundaries, focusing, 520f
 - vertical direction definition, 128
- Septum, for beam extraction, 508
- Shunt impedance, 452
- Side coupled linac, 465, 469f
- SIN cyclotron, 528f
- Skin depth, 291, 293, 373
- Slow wave, non-existence in uniform waveguides, 393
- Slow wave properties:
 - non-existence in uniform waveguide, 393
 - radial defocusing of captured particles, 476f
 - rest-frame description:
 - non-relativistic, 475f
 - relativistic, 477
- Slow wave structures, 393f
 - capacitively loaded transmission line, 394f, 401 f
 - dispersion relationship, iris-loaded waveguide, 403f
 - energy flow in, 449
 - individually phased cavity array, 398
 - iris-loaded waveguide, 395f
 - dispersion relationship, 403f
 - frequency equation, 447f
- Solenoid, 68
- Solenoidal magnetic lens, 125f
- Space charge, 64
- Sparks, 216
- Spectrograph, 180 degree for charged particles, 128
- Spectrometer:
 - dual-focusing magnetic, 133f
 - orange, 131
- Speed of light, c , 15
- Squares, method of, 53
- SSC (Superconducting Super Collider), 543
- Stability bands, 189
- Stanford Linear Accelerator (SLAC), 442
- Stationary frame, 13
- Stoke's theorem, 48f
- Storage ring, 503f, 539
- Stream function, 72
- Strong focusing, 550f
 - acceptance, 551
 - comparison with weak focusing, 550f
 - effect of alignment errors
- Successive overrelaxation, method of, 55f
 - with space charge, 67
- SUPERFISH code, 455
- Superposition, electric and magnetic fields, 64, 89
- Surface charge, dielectric materials, 79
- Surface current, paramagnetic and ferromagnetic materials, 88
- Switch, 198
 - closing, 198, 231

Index

- opening, 198, 236
- saturable core inductor, 263f
- spark gap, high power, 259
- Synchrocyclotron, 502, 523f
 - beam extraction from, 523f
 - comparison with cyclotron, 523
- Synchronous particle, 410f
 - condition for:
 - individually phased cavities, 411f
 - racetrack microtron, 495f
 - Wideroe accelerator, 454
- Synchronous phase, 411
- Synchrotron, 502, 531f
 - energy limits, 535
 - focusing cell, definition, 533
 - geometry, 531f
 - longitudinal dynamics, 544f
 - magnets, separated function, 532
 - principles of operation, 531f
 - strong focusing in, 550f
 - superperiod, 533
 - synchronization condition, 546f
 - synchrotron radiation in electron accelerator, 535f
 - transition energy, 544, 549f
 - types of, 502f
 - weak focusing, 534
- Synchrotron oscillations, 544, 549
- Synchrotron radiation, 535
 - beam cooling by, 536
 - energy limits, electron synchrotron, 535f
 - expression for, 535
- Tandem Van de Graaf accelerator, 222, 224
- Telegraphist's equation, 245
- Termination, of transmission line, 246f, 381f
- Thick lens equation, 119
- Thin lens array:
 - orbital stability, 182, 187
 - particle orbits in, 179f, 187
- Thin lens equation, 119
- Time dilation, 16f
- Time domain, 198, 240
- Topics, organization, 4f
- Toroidal field sector lens, 131
- Torus, 68f
- Townsend coefficient, first, 214, 216
- Townsend discharge, 220
- Transformation:
 - Galilean, 13f
 - Lorentz, 20f
 - Newtonian:
 - kinetic energy, 14
 - velocity, 14
 - relativistic, velocity, 21
- Transformer, 204f
 - air-core, 204f
 - droop, 207f
 - energy losses, 208
 - equations, 206
 - equivalent circuit models, 206f
 - impedance transformation, 207
 - pulse, 207
 - role of ferromagnetic material, 207f
 - volt-second product, 209
- Transform function, of a diagnostic, 272
- Transit-time factor, 473f
- Transmission line, 240f
 - capacitance of, 249
 - capacitively loaded, 343f
 - dispersion relationship, 401f
 - coaxial, properties, 240f
 - conditions for TEM wave, 243
 - current diagnostics in high power line, 277
 - equations, time domain, 243f
 - frequency domain analysis, 380f
 - at high frequency, 388
 - inductance of, 247
 - lumped element circuit model, basis, 242f
 - matched termination, 247
 - parallel plate, properties, 241
 - as pulsed power modulator, 246f
 - pulse-forming-network equivalent, 254f
 - pulselength, as pulsed power modulator,

Index

- 249
 - quarter-wave line, 384
 - radial, properties, 317f
 - reflection coefficient, 382
 - relation to pulse forming networks, 240
 - solutions of wave equation, properties, 245f
- stripline, properties, 241
- termination, 246
- transformer properties, 382f
- transmission coefficient, 382
- two-wire, properties, 241
- velocity of wave propagation, 246
- voltage diagnostics in high power line, 275f
- wave equation, 245
- wave reflection at termination, 246f, 381f
- Trimming coils, in cyclotron, 526
- Triton, properties, 10
- Two-terminal elements, 197f
- UNILAC accelerator, 471
- Van de Graaff accelerator, 221
 - equipotential shields in, 225f
 - minimizing electric field stress, 223f
 - parameters, 221f
 - principle of operation, 221f
 - tandem, 222, 224
 - voltage grading, 223f
 - voltage measurements, 269f
- Vector, particle orbit, 166, 183f
- Velocity, 11
- Voltage, measurement, 267f
 - generating voltmeter, 269f
 - resistive divider, 269
 - resistive shunt, 268f
 - see also Pulsed voltage measurement
- Water:
 - in coaxial transmission line, 250
 - dielectric properties, 80
 - microwave absorption, 80
 - electrostatic energy storage, 85, 212
 - insulation properties, fast pulse, 212
 - in radial transmission line, 319
 - resistors, 271
- Waveguides, 386f
 - applications, 387
 - comparison to transmission line, 387
 - cutoff frequency, 387, 392
 - dispersion in, 387
 - lumped-circuit-element analogy, 387f
 - phase velocity in, 393
 - properties, 387f
 - slow waves, see Slow wave structures
 - solutions for TM₁₀ mode, 391f
- Weak focusing, 150
- Whiskers, 227f
 - effect on vacuum insulation, 229f
 - enhancement of field emission on metal surface, 227
 - removal by conditioning, 229
 - vaporization, 227f
- Wideroe accelerator, 453f
 - limitations, 454
 - synchronous particle in, 454
- Work, definition, 12
- ZGS (Zero-gradient Synchrotron), 133, 534